The Cascadia subduction zone: Kinky or not?

An implementation of a 2D background velocity model in teleseismic scattered-wave inversion

Maren Kjos Veim

May 31st, 2017

Department of Earth Science

A thesis for the degree Master of Science

UNIVERSITY OF BERGEN
Faculty of Mathematics and Natural Sciences

Abstract

This thesis, within the field of seismology, investigates the process and effect of implementing a complex reference model in a teleseismic migration technique based on the Inverse Generalized Radon Transform. This migration technique utilizes concepts from the field of integral geometry, in order to accurately generate high resolution images of the subsurface. This technique is particularly powerful in the case of subduction zones, as indicated by previous applications, such as that of Rondenay et al. (2001).

A subduction zone is a geological setting in which one tectonic plate plunges underneath another. As the plate plunges downwards, it releases water due to an increase in pressure and temperature. This water enters the mantle of the overriding plate and changes the petrology of this area, the forearc mantle, through hydrothermal reactions.

Understanding this process is important, as it might lead to an increased understanding of mantle dynamics in general, and the dynamics of subduction zones in particular. A key step to an increased understanding is to accurately map the spatial extent and material properties of the plunging plate and the forearc mantle.
To better image these features, this thesis describes the implementation of an improved imaging method that addresses a limitation in the original teleseismic migration approach of Rondenay et al. (2001). The original technique utilizes a 1D background velocity model as a basis for key calculations. Assuming that the seismic properties of a subduction zone is restricted to a 1D geometry is a major simplification. In this thesis I address this simplification by modifying the method to account for a 2D background velocity model.

By addressing this limitation I am able to generate images of higher robustness and resolution. I demonstrate the effect of this implementation by applying the new modified method to both synthetic data and real data obtained from the Cascadia subduction zone. Through this application I observe that the imaging of the dip of the subducting plate is better resolved by the implementation of a 2D background model, and that the features of the subduction zone are, in general, better constrained using the new improved method.

I therefore conclude that, while more research and development can and should be done in this area, the implementation of a 2D background velocity model described in this thesis is a promising step towards a better resolved subduction zone system.

Preface

This thesis was written in the spring of 2017, for the Department of Earth Science at the University of Bergen, as part of the NFR-funded project "Subduction zone Water and Metamorphism: a Modelling and Imaging Study (SwaMMIS)".

I would like to thank my supervisor Stéphane Rondenay, and cosupervisor Henk Keers, for guidance and feedback along the way. I would like to thank Felix Halpaap for creating the synthetic dataset and for help throughout the project. Most of all, however, I would like to thank Simen Skaret Karlsen for continuous support and encouragement throughout the project, as well as the tremendous effort that went in to the final proofreading of this thesis.

Contents

List of Figures

Chapter 1

Introduction

1.1 Background

Subduction zones are defined as areas where one tectonic plate moves underneath another (Fowler, 2005). This creates a complex system of forces interacting with each other, resulting in strain and stress on the system. As the plate is pushed down into the mantle, it is subjected to an increase in temperature and pressure, fluids escape from the subducting plate and we observe a change in the material composition of the overriding mantle.

Subduction zones are of great interest in the Earth sciences. Understanding subduction zones is important for hazard studies and for mantle dynamics, as it might lead to a better understanding of the generation of new mantle material, large scale mantle flow and the dynamics of the subduction zone. The material properties of the forearc mantle wedge, which is a key geological feature of a subduction zone, might provide an insight to the mantle dynamics in specific, and subduction zone system in general (Bostock et al., 2002). Subduction zones may be studied using methods such as seismic tomography, refraction and wide angle reflection surveys, magnetotelluric surveys and migration methods (Unsworth and Rondenay, 2013).

The development of more powerful tools and accumulation of more accurate data allow us to improve upon these methods over time. The data quality is ever increasing, both in terms of number of stations recording seismic events, increase in the quality of the stations, and the overall number of seismic events recorded as time progresses. More powerful tools allow us to revisit previously developed techniques with fewer constraints. Among the methods, teleseismic migration is particularly interesting as it provides high resolution images by utilizing multiple scattering phases, adding an additional level of constraint to the produced image(Rondenay, 2009). However, the

technique so far has assumed a (flat earth) 1D background velocity model, severely simplifying the spatial properties of a subduction zone. Further, its computational power is limited as it only observes perturbations in a 2D plane. This serves as a severe limitation to the method, as the results of primary calculations in the technique relies on an accurate seismic model, leading to significant deviations when the reference model is overly simplified (Bostock and Rondenay, 1999). In this thesis, the results of a Master's project that addresses this limitation is presented. As part of the project, I have implemented a more complex background velocity model, utilizing improvements in computational tools and power to cater to the more or less two dimensional structure of a subduction zone.

We revisit the technique of the 2D generalized Radon transform inversion (inverse GRT), proposed by Beylkin (1984), Miller et al. (1987) and, Beylkin and Burridge (1990). A technique further developed by Bostock, Shragge and Rondenay in 2001 (Bostock et al., 2001), (Shragge et al., 2001),(Rondenay et al., 2001). The basic concept of the inverse GRT is to take advantage of an analogy between the Radon transform and the back projection of acoustic scattering potential. The Radon transform maps the points along an integral surface (a surface described by an integral) in a data space onto a single point in a model space. The acoustic scattering potential describes the propagation of seismic energy from a source. The back projection of the acoustic scattering potential projects the scattered data back to its source, i.e. a transformation from a surface (scattering potential) to a point(source). This analogy allows us to reconstruct the seismic properties of a point in space, by generating a weighted diffraction stack of the related seismic data along the isochronal surface corresponding to this point.

The previous implementations of the technique utilize a 1D background velocity model to calculate the various parameters needed for the GRT inversion. A 1D velocity model not only limits the amount of calculations for each image point, but also the variance in input parameters, allowing one set of input parameters to be used for several image points. Calculating these parameters in advance and storing the generated values in a table provides a major increase in efficiency. A 1D velocity model is, however, a major simplification of the actual subsurface, leading to a subpar stacking of data, in turn resulting in less clear images where finer structures might be overlooked or missing. This simplification has been a necessity in order to limit the computational demand of the method, but leads to a lower signal-to-noise ratio, influencing the quality of the generated image. Modifying the method to allow for a more complex background velocity model should alleviate much of this concern and generate a better resolved model in terms of reliability and resolution.

In particular, there are two noteworthy elements from the study by Rondenay et al. (2001) whose imaging could benefit from a more precise model:

- The dip of the subducting slab, and the assumed kink in this slab.
- The petrological properties and extension of the forearc mantle.

The project is written in Matlab. Matlab is a programming language developed for solving scientific and engineering problems. This project is a further development of a set of already existing Matlab-scripts generated by Rondenay as part of his PhD-project, published in 2001. The evaluation of the project was based on synthetic and real datasets. The synthetic datasets were generated by Felix Halpaap using the software Specfem, a software for simulating the propagation of seismic waves. The real dataset is part of the dataset CASC93, the same dataset used in 2001 by Stéphane Rondenay.

1.2 Outline of project

1.2.1 Research questions

The primary task of this project was to develop the tools and methods needed to implement a 2D background velocity model in the technique presented by Bostock, Shragge and Rondenay in 2001, as well as implementing the actual model. As part of this project it is relevant to evaluate the following research questions:

1. Will incorporating a 2D background velocity model provide a significant improvement to the models generated by the original method?
   (a) Will incorporating a 2D background velocity model allow us to ultimately identify the proposed kink in the dipping slab imaged by the old technique as a feature or as an artefact generated by the old method?
   (b) Is the mantle wedge more discernible by utilizing a 2D background velocity model?
2. Will incorporating a 2D background velocity model provide an improvement significant enough to justify the additional processing time?

1.2.2 Project description

In this thesis I am expanding from the 1D background velocity model to a 2D background velocity model, varying perpendicular to the strike of the subduction zone. A 2D velocity model provides a more accurate depiction of the subsurface, as a subduction zone has a high degree of variation perpendicular to the direction of strike. This expansion will provide an improvement to the accuracy of the travel time, as well as other inversion parameters, thus improving the stacking of the data. This should lead to a more constructive summation of scattered signals and thus a better signal-to-noise ratio and a better resolved model.

The evaluation of whether or not the improvement constitutes a *"significant improvement"* will be evaluated in a qualitative fashion. Of particular interest will be observations that confirm or conflict with the inferred subsurface structure from the previous study by Rondenay et al. (2001). Observations regarding the subducting slab dip and supposed mantle wedge will be of special concern, adhering to the focus of the research questions.

Given a correction in dip we may evaluate if this correction supports or contradicts the increase in slab dip at 40 km generating a kink in the slab as proposed by Rondenay et al. (2001). The mantle wedge may be identified through the properties of the crust-mantle transition. Rondenay and Bostock identified the mantle wedge of the Cascadia subduction zone as heavily serpentinized(Rondenay et al., 2001), (Bostock et al., 2002) ,(Bostock, 2012). The serpentinization of a mantle wedge will reduce its seismic velocities, softening the crust-mantle discontinuity. Given enough serpentinization, the discontinuity may disappear completely or even reappear as an inverted discontinuity, with a transition from fast to slow seismic velocities, in contrast to the slow to fast transition normally associated with the crust-mantle discontinuity. By observing the crust-mantle transition above the forearc mantle we may be able to evaluate the degree of serpentinization and the horizontal extent of the mantle wedge.

The evaluation of additional processing time will also be done in a qualitative manner. The evaluation of this research question is not critical for a proof of concept, but it is relevant for potential further improvement. A *"long processing time"* is of course a relative measure, as is *"significant improvement"*. A partial goal of the project is to minimize the increase in processing time to facilitate further work. This question will be evaluated relative to the primary research question, comparing increase in total processing time against the relative success of the project.

Chapter 2

Subduction zones

2.1 Plate tectonics

The Earth's lithosphere is a dynamic system consisting of a number of tectonic plates moving and interacting with each other. This creates tension and compression, ultimately leading to the creation of new lithosphere and destruction of old. There exist about 15 major tectonic plates, divided into continental and oceanic plates. They largely behave as rigid entities, so that most deformation occurs along their boundaries (Stein and Wysession, 2009). The interaction between two plates may be categorized as one of three types: Divergent, transform and convergent, depending on their relative direction of movement. A divergent interaction occurs when two plates move away from each other, creating new lithosphere in the resulting gap. A transform interaction is when two plates move parallel to each other, so that little to no lithosphere is destroyed or created. A convergent interaction arises when two plates move towards each other, eventually overlapping. Such an interaction forces the underlying plate to plunge into the mantle due to the weight of the overlaying plate. The converging scenario where one tectonic plate is forced underneath another is also known as a subduction, as one of the two plates is subducted. The region where subduction occurs may be referred to as a subduction zone. In this thesis the main focus is on oceanic-continental subduction zones and in particular the Cascadia subduction zone.

2.2 Geometry of a subduction zone

As already determined, a subduction zone consists of two tectonic plates, one heavier, usually oceanic, subducting plate, and one, overriding, lighter, usually continental plate, see figure 2.1. The line of intersection, where the overriding plate meets

the subducting plate, evolves to become an oceanic trench. A wedge of sediment builds up along the intersection as the overriding plate scrapes the upper sediments off of the subducting plate. The subducting slab causes a change in the mantle composition, temperature and flow, creating a mantle wedge. This causes an upwelling of mantle, resulting in volcanic activity in the nearby upper continental crust, creating a volcanic arc. The area between the volcanic arc and line of intersection is called the forearc, while the area of the continental overriding plate landward of the volcanic arc is called the backarc. The still intact subducting oceanic plate is simply called the oceanic plate, while the subducted part of the oceanic plate is referred to as the slab.

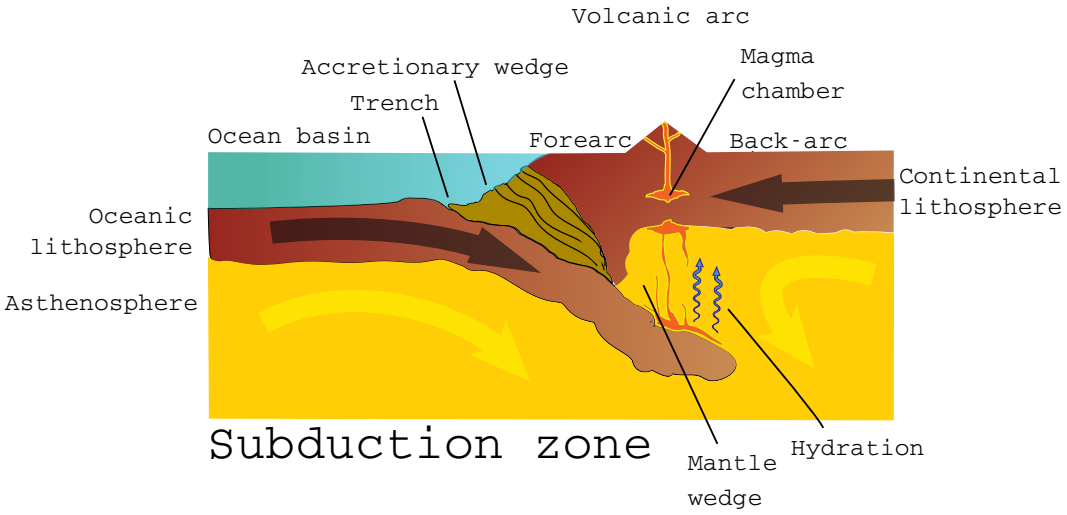

Figure 2.1: Illustration of a subduction zone. Modified from wikimedia (Wikimedia Commons, 2016)

2.3 Mantle wedge

The mantle wedge is located in the mantle beneath the forearc. It is part of the mantle, but has a different rheology than the nearby asthenosphere. This is due to its lower temperature and the presence of fluids originating from the colder subducted lithospheric slab. This affects the properties of the forearc mantle, for instance by a decrease in seismic velocities, reducing density and increasing Poisson's ratio (Hyndman and Peacock, 2003).

The subducting oceanic crust contains free water in pore spaces and water bound in hydrous minerals. The oceanic plate acts a vessel for the transportation of fluids

into the mantle, facilitating the hydration of the forearc mantle (see figure 2.2). Water is released due to metamorphic reactions in the slab, caused by an increase in pressure and temperature at lower depth. The release of water diminishes with depth, meaning that most of the water is released beneath the forearc while some is released later, facilitating magma generation connected to the volcanic arc.

Free water is released early in the subduction process due to the compaction of pore spaces. Water bound in minerals is released through metamorphic reactions. The main metamorphic dehydration of the subducting slab occurs through a process known as eclogitization. Eclogitization is associated with an increase in density and decrease in seismic contrast (Bostock et al., 2002). Different metamorphic reactions occur based on pressure and temperature conditions. Once released from the slab, water fluxes into the mantle wedge above and reacts with rocks there.

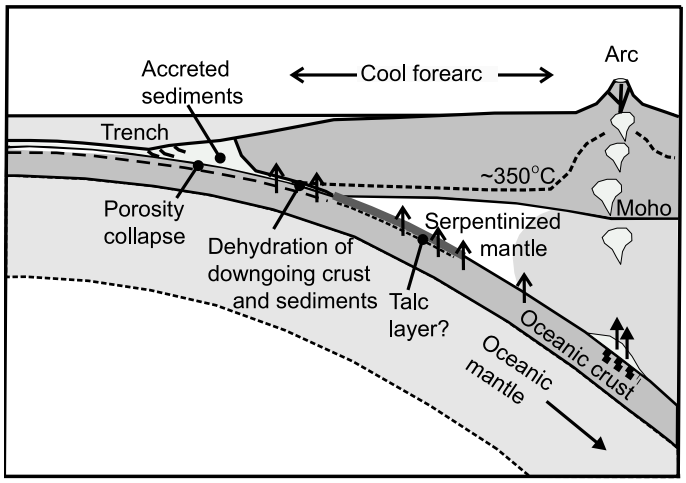

Figure 2.2: Illustration of a the dehydration process in a subduction zone, Hyndman and Peacock (2003).

2.4 Hydration

The presence of water in a subduction setting has a significant affect on the expression of the seismic properties in the region (Bostock, 2012). A dry mantle forearc is thought to consist of depleted ultramafic rocks, mainly consisting of olivine and orthopyroxene (Hyndman and Peacock, 2003). The addition of water creates hydrous minerals such as serpentine, talc and brucite, depending on the temperature and pressure conditions (see overview by Hyndman and Peacock (2003) as shown in figure 2.2). The amount of water supplied is dependent on the convergence rate (speed of the subduction), the age and thickness of the incoming oceanic plate and the dip of the subducting slab. The hydration of the mantle wedge affects the rheol-

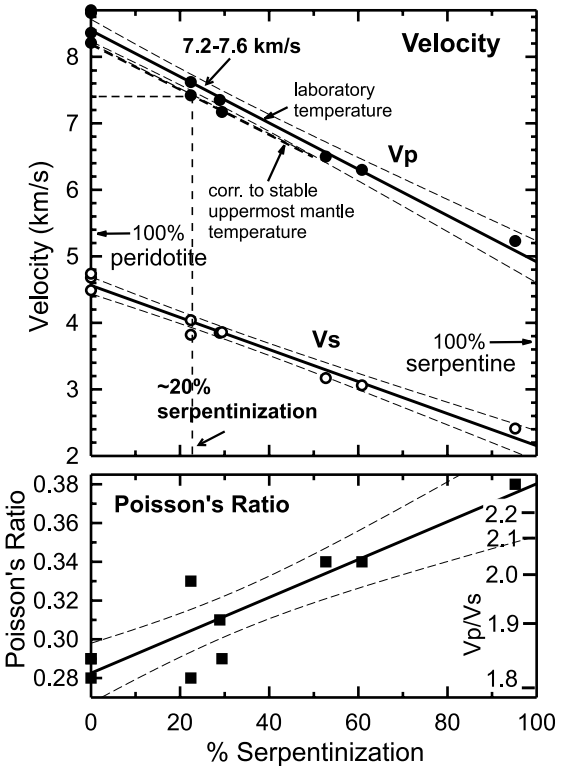

Figure 2.3: Laboratory conditions, mantle peridotite. V_P/V_S-ratio and Poisson's Ratio as a function of serpentinization. Figure by Hyndman and Peacock (2003), Data originally obtained by Christensen (1966).

ogy, as hydrated materials generally have lower seismic velocities than the original material. The decrease in seismic velocities and increase in Poisson's ratio in relation to the degree of serpentinization is evident through figure 2.3 by Hyndman and Peacock (2003). In their article they conclude that a serpentinization degree of 20% is common and that serpentinization locally may reach as high as 50%.

The presence of hydrated minerals in the forearc mantle is supported by observations of serpentine mud volcanoes located on the Mariana and Izu-Bonin forearcs, and outcrops of hydrated ultramafic rocks, suspected to originate from paleo-subduction zones. Seismic properties resolved through wide-angle refraction studies also support a hydrated forearc mantle (Hyndman and Peacock, 2003).

Chapter 3

Geophysical imaging of subduction zones

The goal of this thesis is to better image the subsurface using the generalized Radon transform (GRT), by incorporating a new, more detailed background velocity model. Before going into how this will image the subsurface with increased accuracy, it is imperative to first understand how the subsurface is imaged in general and by the GRT specifically. It is helpful to have a clear understanding of where the background velocity model is utilized, and why modifying it might lead to improvement of the produced model. It is also beneficial to have an understanding of the techniques used to incorporate the new 2D background velocity model.

Common techniques for imaging subduction zones are:

- **Seismic tomography**: An inverse technique that uses artificial or natural sources to create 3D images of the earth by computing the travel time of ray paths through the a medium, and comparing them to observed travel times, to infer volumetric anomalies in the material properties.
- **Teleseismic imaging**: Maps the subsurface by observing the effect of perturbations in the medium on the scattered wavefield, using natural sources.
- **Refraction and wide-angle reflection surveys**: Maps an area using artificial sources and evaluating the perturbations in velocity using travel times and scattered waves to image discontinuities.
- **Magnetotelluric surveys**: Determines the Earths structure by investigating the electrical resistivity and thus inferring information on the fluid content.

In this project, teleseismic imaging has been used due to the need for a high resolution image in the 0-200 km depth range, a result not obtained by the other three methods (Unsworth and Rondenay, 2013).

Mapping the subsurface using teleseismic data utilizes the same premise as echolocation. By observing recorded seismic energy generated by a known source, known as a trace, we may make an educated guess about the properties of the medium which the energy travelled through, and by extension the materials present in this medium. The trace is recorded as a time series, usually in three perpendicular directions: One in the vertical and two in the horizontal plane. We record the energy in this fashion in order to detect seismic energy arriving from all directions, as well as determining its direction of origin, through backpropagation. Recording multiple sources of energy, at multiple locations, moving through the same medium, allow us to map the medium with a higher precision and reliability.

3.1 Wave equation

In seismic imaging, as well as seismic tomography, the results are found using methods based on the wave equation. Methods utilizing the wave-equation to image mediums are equivalent to finding a numerical solution to a partial differential equation. The wave equation describes the propagation of a wave in the proposed medium. Where possible, the medium is usually reduced to the simplest feasible case.

The simplest possible case is an acoustic medium. In an acoustic medium the energy moves through the medium only as a compressional (or dilatational) wave, and the response of the medium is the same, regardless of the direction in which the energy is moving. Water and air are primary examples of acoustic media. Describing the wave propagation in a more complex, elastic isotropic case, provides a more accurate depiction of real life geological scenarios. This allows for the propagation of shear waves while the response of the medium is still unaltered by the direction of movement. As shear waves are necessary to support the different scattering modes used for GRT, an elastic isotropic medium is required for this method.

Equation 3.1 is the wave equation for an elastic isotropic medium, which describes how a medium experiences a (small) displacement in response to an external force. In this equation u_i is the displacement of the medium caused by the external force, ρ is the density, c_{ijkl} is the elastic tensor and f is the external force. Equation 3.2 is the Ray equation. It describes the response of the pressure field at position $\mathbf{x}$ to a point-source. In this equation $\omega = 2\pi f$, angular frequency, $T(\mathbf{x})$ is the traveltime, and $A(\mathbf{x})$ the amplitude, both at position $\mathbf{x}$ (Auld, 1973).

$$\rho \frac{\partial^2 u_i}{\partial t^2} = \partial_j \left(c_{ijkl} \partial_k u_l \right) + f_i \tag{3.1}$$

$$u = A\left(\mathbf{x}\right) e^{i\omega T(\mathbf{x})} \tag{3.2}$$

3.2 Wave propagation and Ray theory

The propagation of a wave may be described using a wave front or a ray. The wave front describes the total propagation of the energy in a volume generated by the source. In an acoustic 3D medium this would be described by a perfect sphere. The wave front at any point in space is always perpendicular to the direction of propagation in that point. The ray describes the direction of the propagation of the wave, radiating outwards from the source. The wave front is useful for tracking the entire wave-field, while the ray is used for tracking the energy propagating in a particular direction between two distinct points in space. As the wave front propagates outwards, the curvature of the front becomes smaller and smaller as the sphere becomes bigger. The wavefront of energy originating from teleseismic distances has such a small curvature that we may assume a planar wavefront for mathematical simplicity, while still retaining a good approximation of the wave front. Figure 3.1 illustrates the relationship between a ray, wave front and the implication of the assumption of a planar wave front.

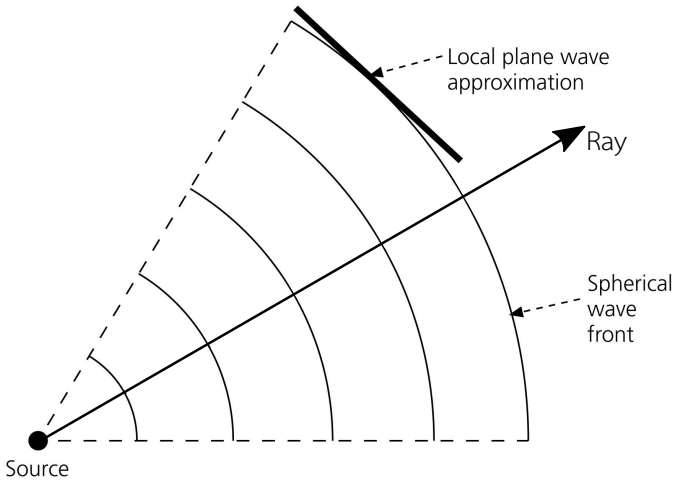

Figure 3.1: Illustration of a ray and wave front, modified from Stein and Wysession (2009).

The propagation of a wave through space can be described by Huygens' principle, stating that each point in space agitated by a wave can be considered a new source of

energy. The energy radiating outwards along the wavefront interferes destructively along the wave front, while the energy propagating onwards interferes constructively, in sum generating the spherical wavefront observed, see figure 3.2. The scattering/diffraction of the energy in this fashion is what allows the energy of the wave to move around obstacles.

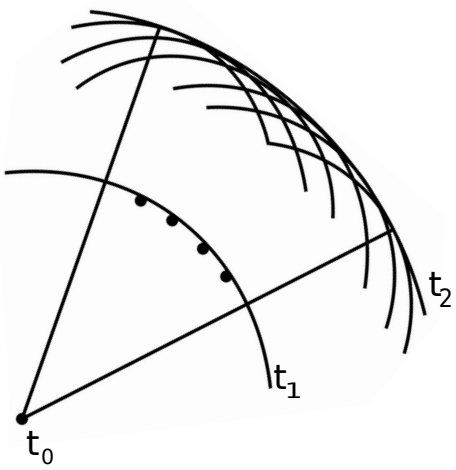

Figure 3.2: Illustration of Huygens principle, modified from Stein and Wysession (2009).

We classify seismic waves based on the direction of particle motion caused by the seismic energy. The volume waves are in general divided into P-waves and S-waves. Surface waves are commonly divided into Love waves and Rayleigh waves, but will be ignored for the remainder of this thesis. P-waves are waves caused by a particle movement parallel to the direction of propagation, causing a compressional or dilatational wave, depending on whether the particle moves in the direction of propagation, or against the direction of propagation. S-waves cause particle motion perpendicular to the direction of propagation, subdivided into SH-waves and SV-waves, moving in the horizontal direction and vertical direction respectively.

3.3 Scattering

At a point scatterer, the seismic energy is not only propagated onwards in the same phase, but rather diffracting into multiple phases. A compressional P-wave may transmit or reflect seismic energy both as a compressional P-wave and as a shear S-wave. Any interface may be considered a series of scatterers, just as a line in geometry may be considered as a series of points. As Huygens' principle applies the energy propagating from each scatterer will interfere constructively and the energy

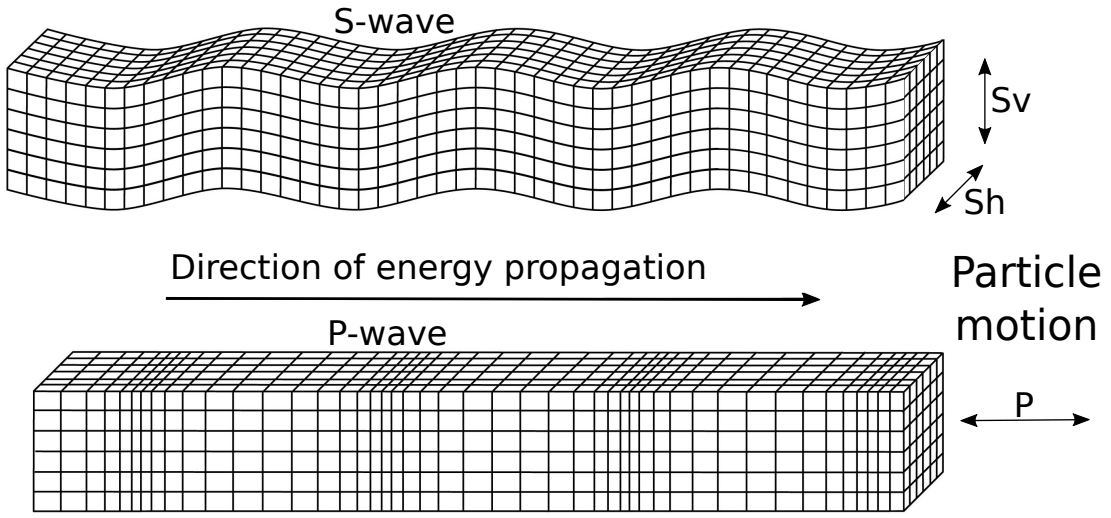

Figure 3.3: Illustration of the particle motion of P-wave and S-wave propagation, modified from Stein and Wysession (2009).

transmitted or reflected will be observed as a wave front.

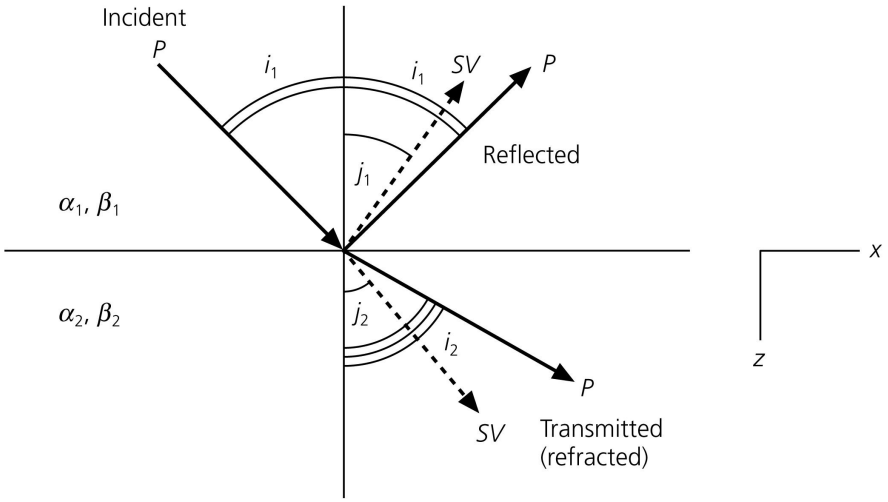

Figure 3.4: Illustration of reflection and transmission of seismic energy into multiple phases, modified from Stein and Wysession (2009).

A discontinuity in the medium, a sudden change in a material property, will cause the energy to be reflected or transmitted, changing the direction of propagation. The change in direction depends on the changes in properties across the discontinuity, in accordance with Snell's law (equation 3.3). Here, θ_1 is the incidence angle and θ_2 is the scattering angle, v_1 and v_2 are the seismic velocities of the the media on either side of the discontinuity.

$$\frac{v_1}{sin\theta_1} = \frac{v_2}{sin\theta_2} \tag{3.3}$$

Snell's law allows us to estimate the fastest ray path between two points in space, and thus the travel path of the first arriving wave. The spatial geometry of the two points and the medium, dictates the fastest path. This is the path that spends the most time in the fastest layer and the least time in the slowest. The direction of the ray path, measured by its angle against the vertical, may be described by the ray parameter. The ray parameter is the reciprocal of the horizontal apparent velocity c_x, which is the velocity of the seismic energy measured only in the horizontal direction.

$$p = \frac{1}{c_x} = \frac{sin\theta_i}{v} \tag{3.4}$$

The ray parameter, equation 3.4, remains constant along the entire ray path, making it useful for mathematical calculations. The ray parameter may also be referred to as the horizontal component of the slowness of the wave. The slowness of the wave, the inverse of the velocity, may be divided into its horizontal and vertical components, using vector decomposition, see figure 3.5. The horizontal component of the slowness vector is thus independent of the vertical movement, while the vertical component is independent of the horizontal movement.

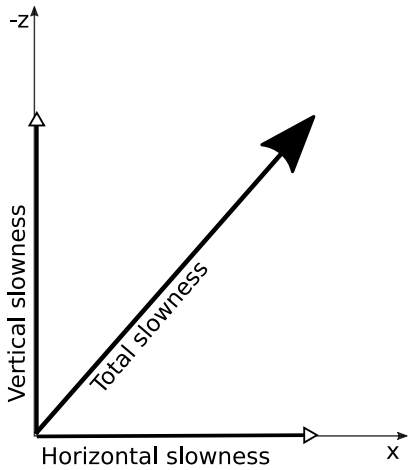

Figure 3.5: Illustration of vector decomposition.

Energy transmitted at a discontinuity may be described as a forward scattering, or more precisely as a forward scattered P-to-P, if the energy had a compressional or

dilatational particle motion, P-phase, before and after the interaction a discontinuity. Reflected energy, may be described as a backscattered P-to-P, again assuming both phases are compressional/dilational particle-motion.

Each of these scatterers are inhomogeneities in the medium, caused by a perturbation in the Lamé parameters, resulting in a change in seismic velocity or density, diffracting the seismic energy. The Lamé parameters λ and μ describe the elastic properties of the medium, which in turn affect the seismic velocity of the medium. μ describes the rigidity of the medium and the bulk modulus is described by κ (Stein and Wysession, 2009).

$$\text{P-velocity: } \alpha = \sqrt{\frac{\lambda + 2\mu}{\rho}} = \sqrt{\frac{\kappa + \frac{4\mu}{3}}{\rho}} \tag{3.5}$$

$$\text{S-velocity: } \beta = \sqrt{\frac{\mu}{\rho}} \tag{3.6}$$

$$\text{Bulk modulus: } \kappa = \lambda + \frac{2}{3}\mu \tag{3.7}$$

The rigidity is the medium's resistance to shearing, or a non-volumetric change of shape. The bulk modulus is the incompressibility of the medium, or the resistance to change in volume. An inhomogeneity in the medium is in other words a change in the medium's ability to compress or distort, correlating to a petrological change, i.e. a change the chemical structure and/or the composition of the medium.

3.4 Seismic imaging

Seismic imaging is generally divided into inverse and forward modelling, classified based on the approach used to image the medium, illustrated in figure 3.6. In inverse modelling, we start with the observed traces, and from this we infer the likely properties of the medium, applying the theory of wave propagation and utilizing various mathematical techniques, such as the Fourier transform. Forward modelling is an iterative process in which we use the theory of wave-propagation to propose a medium that might generate the observed traces. The traces produced by the proposed model is then compared to the original traces and adjustments are made. The process is then repeated until the misfit between the original traces and the generated traces fall within a predetermined margin of error.

Inverse modeling: Estimating a model m based on the observed arrival times d, utilizing the generalized inverse G^{-g} to account for a potential overdetermined system of equations:

$$\Delta m = G^{-g}\Delta d = (G^T G)^{-1} G^T \Delta d \tag{3.8}$$

Forward modeling: Predicting the model m that produces arrival times d:

$$\Delta d = G(\Delta m) \tag{3.9}$$

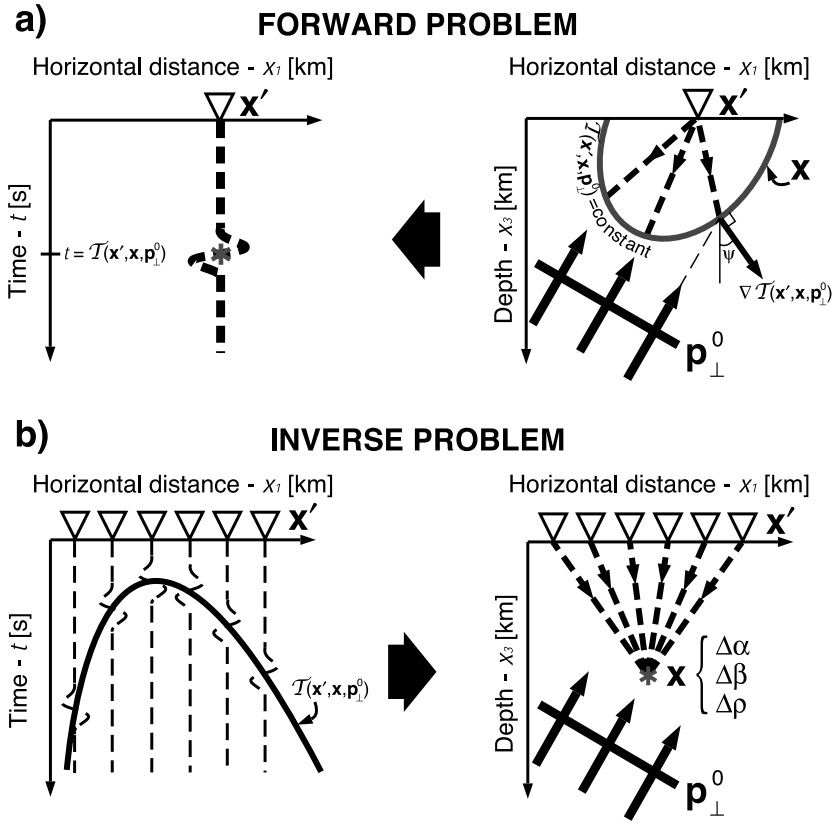

Figure 3.6: Illustration of inverse vs. forward modeling (Rondenay et al., 2005).

In seismic imaging, we solve for the unknown medium through a process called migration. Migration of seismic data may, in short, be described as a summation of recorded traces corrected for traveltime offset. A trace is the signal recorded at the station. In the case of teleseismic imaging, imaging using passively recorded earthquakes, the trace may, once corrected for the source and instrument response, be referred to as a receiver-function, and represents the response of the earth to the seismic event. The trace does, however, still contain a lot of unwanted information, also known as noise.

When summing traces constructively, they need to be aligned so that the wanted signal, the incident energy, interferes constructively while the remaining signal, the noise, interferes destructively, meaning that the alignment serves to reduce the noise in the stacked data. When summing traces, a correction for travel time offset therefore needs to be made, as seismic energy must travel a longer time period to reach a station further away from the source; the incident energy will arrive at different times at different stations. The time shift is estimated based on a background velocity model. A more accurate time-shift will lead to a better signal-to-noise ratio and in turn a better resolved model.

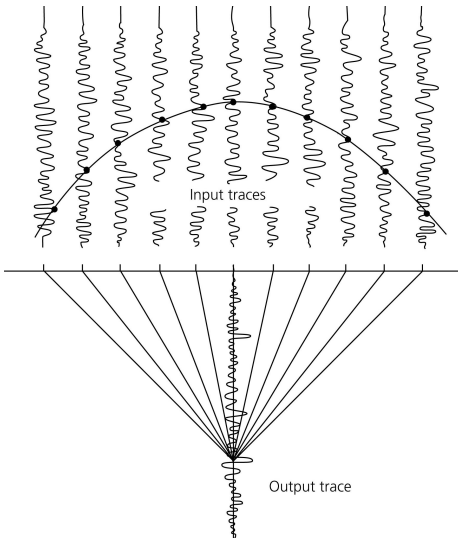

Figure 3.7: Illustration of summing of traces (Stein and Wysession, 2009).

Different migration techniques differ in how they estimate the time shift required to get the best output trace; The stacked trace with the highest signal-to-noise ratio.

In the early days of migration, summation was based on a purely geometrical understanding of the source and receiver configurations. Today this is referred to as classical migration or diffraction stack migration, as the traces are corrected for travel time offsets by summing along a diffraction hyperbola. The diffraction hyperbola is calculated based on the geometry and d=v/t (Gazdag and Sguazzero, 1984)(Miller et al., 1987). This was later exchanged for an approach relying more on the mathematical understanding of wave-propagation using the wave-equation. The recorded energy was then backpropagated in time and the image was estimated based on the wave field (Miller et al., 1987).

The migration technique used in this project was developed in the 1980s by among others Miller et al. (1987) and Beylkin (1984). It was developed to address both the

problem of the underdetermined wave equation method, and the geometry dependence and over-simplification associated with the classical migration. The technique decouples the forward and inverse methods in a way that allows for inversion of multi-receiver, multi-source experiments afforded by classical migration, while still keeping the level of accuracy afforded by the wave equation and the mathematical analysis of the forward problem.

3.5 Generalized Radon Transform

Conceptually, the Generalized Radon Transform is a combination of both wave-equation based migration and classical migration, as we use methods developed from the wave-equation to determine the diffraction hyperbola associated with classical migration. First in this section, a geometrical understanding of the Generalized Radon Transform will be explained, as it relates to an isotropic medium. The equation and computations, that later follows, are explained as they relate to an elastic isotropic medium, as this is more relevant in terms of the implementation itself.

The basic concept is to take advantage of an analogy between the Radon transform and the back-projection of the scattering-potential. The Radon transform is a concept from the mathematical field of integral geometry. From the integrals over a general geometric object we are able to reconstruct the function associated with the object, using the inverse of the generalized Radon transform. The scattering potential is the seismic energy that radiates outward from a source, described as a projection integral. Back-projecting the seismic energy recorded at the receivers is the basic concept of a diffraction stack, or classical migration. This back-projection allows us to reconstruct the scattering potential, from which we may derive the material parameters. The analogy between the Radon transform and the back-projection allows us to reconstruct the scattering potential. This is done using the integral surfaces generated by the scattering potential, using the mathematical tools afforded to us through the field of integral geometry (Miller et al., 1987).

The premise of migration is that the material parameters of any point in the subsurface may be imaged by detecting the field of seismic energy scattered from this point. In classical migration, the seismic data is stacked along a diffraction curve determined by the source-scatterer-receiver traveltime, known as the 'reflection-time-surface', see figure 3.8 left. Here the curves R_A and R_B are the reflection-time-surfaces associated with the source, receivers (located along the left side of the plot) and the scatter-points A and B respectively, displayed in 3.8 right. The surfaces are

generated based on the traveltime of each source-scatterer-receiver-combination and the depth of the associated receivers.

Inverse GRT imaging is based on the same premise, but rather than setting a fixed scatter point and finding the reflection time surface, we set a fixed traveltime, and find a surface of scatter-points of equal traveltime, known as an isochronal surface. This means that the seismic energy recorded at the station for a given traveltime, originating from a given source, must have been scattered at one of the points on the isochronal surface. In figure 3.8 you may see an isochronal surface illustrated by the surface that is denoted I_d. This is an isochronal surface that satisfies both scatter point A and scatter point B. The energy travelling from the source to any scatter point on this surface, and then on to the receiver, will have travelled for the same amount of time. We know from common-tangent-stacking that stacking along an isochronal surface will afford the same results as the diffraction stack, as the numbers are just added in a different order (Miller et al., 1987). In figure 3.8 you may also observe how the surface in the model space on the right may be displayed as a point in the data space on the left.

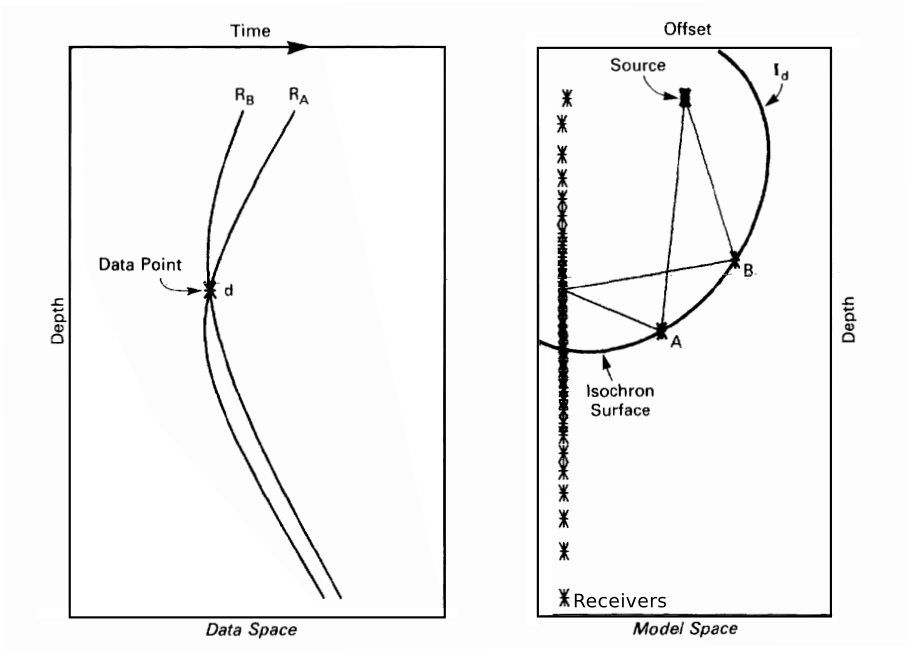

Figure 3.8: Illustration of isohchron surface(Miller et al., 1987).

All in all, inverse GRT is a summation over isochronal surfaces. We sum over the isochronal surfaces for a range of stations and a specific event, as the point of intersection for all of these isochronal surfaces should be the common point at which the energy is scattered. We sum the traces based on the traveltime defined by equations 3.10, 3.11 and 3.12, which vary depending on the scattering mode of the seismic energy.

Scattering index q	**Description**
1	forward scattered P-to-P
2	forward scattered P-to-S
3	backscattered P-to-P
4	backscattered P-to-S
5	backscattered S-to-P
6	backscattered S-to-S (polarization in-plane)
7	backscattered S-to-S (polarization out-of-plane)

Figure 3.9: Table with description of the scattering index

$$\mathcal{T}^{q=1,2}(\mathbf{x},\mathbf{x}',\mathbf{p}_\perp^0) = \int_0^{x3} \frac{dy3}{\upsilon^q(y_3)\sqrt{1-[\upsilon^q(y_3)]^2(p_1^q)^2}} - p_1^0(x_1'-x_1) - \int_0^{x3} \frac{dy_3}{\alpha(y_3)}\sqrt{1-\alpha^2(y_3)|\mathbf{p}_\perp^0|^2} \tag{3.10}$$

$$\mathcal{T}^{q=3,4}(\mathbf{x},\mathbf{x}',\mathbf{p}_\perp^0) = \int_0^{x3} \frac{dy3}{\upsilon^q(y_3)\sqrt{1-[\upsilon^q(y_3)]^2(p_1^q)^2}} - p_1^0(x_1'-x_1) + \int_0^{x3} \frac{dy_3}{\alpha(y_3)}\sqrt{1-\alpha^2(y_3)|\mathbf{p}_\perp^0|^2} \tag{3.11}$$

$$\mathcal{T}^{q=5,6,7}(\mathbf{x},\mathbf{x}',\mathbf{p}_\perp^0) = \int_0^{x3} \frac{dy3}{\upsilon^q(y_3)\sqrt{1-[\upsilon^q(y_3)]^2(p_1^q)^2}} - p_1^0(x_1'-x_1) + \int_0^{x3} \frac{dy_3}{\beta(y_3)}\sqrt{1-\beta^2(y_3)|\mathbf{p}_\perp^0|^2} \tag{3.12}$$

Different scattering modes gets diffracted with different angles and as we only model perturbations in a 2D plane, the velocity of the scattered energy will also vary depending on the scattering mode. These equations, 3.10, 3.11 and 3.12, describes the travel time curves corresponding a unique scatterer-station-event combination, corresponding to the scattering mode q indicating the ray path/particle motion. The diffraction modes are numbered 1-7 and corresponds to 'Forward scattered P-to-P', 'Forward scattered P-to-S', 'Backscattered P-to-P','Backscattered S-to-P', 'Backscattered S-to-S in-plane(vertical)' and 'Backscattered S-to-S out-of-plane(horizontal)', see table, figure 3.9, and illustration of ray paths in figure 3.11.

The traveltime curve $\mathcal{T}(\mathbf{x},\mathbf{x}',\mathbf{p}_\perp^0)$ is the traveltime that corresponds to a line-perturbation in material parameters, perpendicular to our plane at position $\mathbf{x}$, given a receiver at position $\mathbf{x}'$ and a horizontal slowness corresponding to an incoming plane wave with a horizontal slowness $\mathbf{p}_\perp^\mathbf{0}$. See figure 3.10.

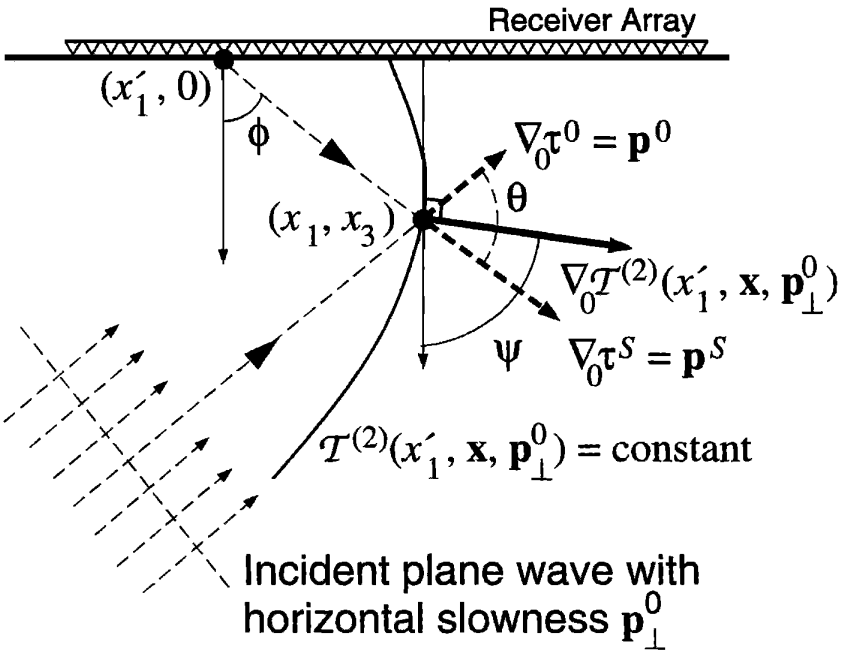

Figure 3.10: Illustration of parameters referenced in equations related to the scattering potential (Bostock et al., 2001).

As we are working in an assumed 2D world, the effects of the third dimension, obliquity, must be normalized. The obliquity corrected velocity is given by equations 3.13, which corrects the velocity of the seismic energy based on the direction of the incident plane wave given by the ray parameter:

$$v^q(y_3) = \left[\frac{1}{\alpha^2(y_3)} - (p_2)^2\right]^{-\frac{1}{2}}, \quad q = 1, 3, 5$$
$$v^q(y_3) = \left[\frac{1}{\beta^2(y_3)} - (p_2)^2\right]^{-\frac{1}{2}}, \quad q = 2, 4, 6, 7 \tag{3.13}$$

The amplitude is expressed by equation 3.14 and associated geometrical spreading J^P by equation 3.15. The partial differential term in equation 3.17, is called Jacobian (displayed separately in equation 3.16). It is used for transforming the operation from an integration over angles to an integration over spatial parameters.

$$A(x_3; x'; p_2) = \frac{1}{4\alpha(x'_3)} \sqrt{\frac{2}{\pi\rho(x_3)\alpha(x_3)\rho x'_3)[J^P(x_3; x'_3)]^2\sqrt{1-p_2^2\alpha^2(x'_3)}}} \tag{3.14}$$

$$J^P(x_3; x'_3) = \sqrt{\frac{\cos\phi(x_3)\cos\phi(x'_3)}{v^q(x_3)\left(\frac{\partial x'_1}{\partial p_1^P}\right)}} \tag{3.15}$$

$$\left|\frac{\partial(\psi,\theta)}{\partial(x'_1,\gamma)}\right| \tag{3.16}$$

This traveltime is used in combination with the radiation pattern, amplitude and a series of weights to define the scattering potential g_r:

$$\begin{aligned} g_r(\mathbf{x}_0) =& \frac{1}{4\pi}\int d|\mathbf{p}^{\mathbf{0}}_{\perp}| \int d\gamma \int dx'_1 \left|\frac{\partial(\psi,\theta)}{\partial(x'_1,\gamma)}\right| \sum_q W_r^u(\theta)\frac{|\nabla_0\mathcal{T}^q|^2}{|\mathcal{A}^q|^2} \\ & \cdot \sum_n A_n^q(\mathbf{x}_0,\mathbf{x}')\nu_n^q[\mathbf{x}', \mathbf{p}^0_{\perp}, t = \mathcal{T}^q(\mathbf{x_0},\mathbf{x}')] \end{aligned} \tag{3.17}$$

The backazimuth γ, in these equations, denotes the horizontal direction of the incoming plane wave, θ is the scattering angle measured against the vertical of the scattered ray and ψ denotes the dip of the sensitivity of the isochronal surface, see figure 3.10. The scattering-matrix W describes the radiation pattern of the scattered energy, dependent on theta, scattering mode and material parameter perturbation. A, the amplitude of the incident and scattered wave, varies dependent on the geometrical spreading.

Equation 3.17 describes a weighted diffraction stack of data ν along the isochronal surface, $\mathcal{T}$. Defining the scatter potential is what allows us to deduce the elastic properties at the scatter point. Evaluating the scatter potential is thus required at each scatter point. The isochronal surface is effectively a moveout curve, varying for different scattering modes.

In our method, we utilize scatterers to deduce how the medium varies as a function of the seismic velocities, and, by extension, the elastic properties. We assume a matrix of scatterers, each corresponding to one pixel in our generated image. We record the incident P-wave at each receiver, in addition to the forward scattered P-to-P and P-to-S, and the backscattered P-to-P, P-to-S, S-to-P and S-to-S, both in-plane and out-of-plane, as the method assumes a 2D medium. The incident wave is assumed to be planar due to the teleseismic distance (epicentral distance $> 30°$) between the stations and epicenter. The scatterers are in close proximity to the stations, relative to the epicenter.

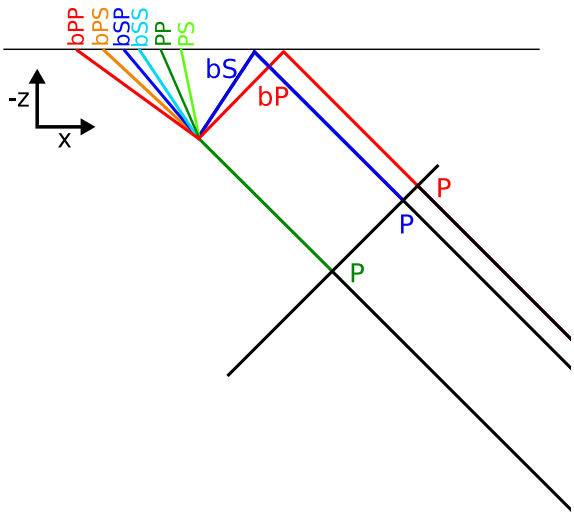

Figure 3.11: Illustration of ray path of scattering modes.

The additional phases provide added constraints, as not all scattering modes propagate equally well in all mediums. A weaker amplitude or complete absence of a scattering mode provides general information on the elastic properties of the medium, in addition to information obtained from the travel path and traveltime.

As the goal of this thesis is to implement a 2D background velocity model, it is worth highlighting the effect of this action. The original method models 2D scatterers in a 1D reference medium. This is a major simplification in terms of traveltime. Seeing as the calculation of the traveltime is so central to the method, this is bound to cause a cascading error corrupting the final models. A new velocity model will primarily affect the traveltime and ray path, and, by extension of the ray path, the slowness and geometrical spreading. The travel time for each ray will be affected as the number of layers increase and layers of both higher and lower velocities are added. The ray path, and thus the slowness of most rays, will be affected, as the ray path will always be the fastest path between two points in the medium, adhering to Fermat's principle, upon which Snell's law is built. Introducing dipping structures in the model also affects the ideal ray path. This will, however, be a source of discrepancy in the new method, as the original method assumes horizontal layers and this is a requirement not easily bypassed. The Geometrical spreading, attenuating the energy of a wave with a factor of $1/r^2$, is also affected, as a change in ray path is also a change in distance travelled, r. This will in turn affect the isochronal surfaces and the weighted diffraction stack.

Chapter 4

The Cascadia subduction zone

4.1 Overview

The Cascadia subduction zone is located along the west coast of North America. It extends 1000 km from Northern Vancouver Island in British Columbia to Cape Mendocino in the northern part of California (Pacific Network, 2017). The subduction zone is an interaction between the oceanic Juan de Fuca plate and the continental North American plate, see figure 4.1. The Juan de Fuca plate subducts at a rate of approximately 42 mm/year, in a North-Eastern direction of 69 degrees. The Juan de Fuca plate is one of the smaller oceanic plates and subducts while still relatively warm and young, at an age of approximately 4-10 Myr (Hyndman and Wang, 1993).

The subduction zone is an area of lower than expected seismicity, with very few earthquakes unambiguously occurring at the interface between the two plates. Megathrust earthquakes are estimated to occur with a return interval of 400-600 years. The last known megathrust earthquake occurred in the northwest, in January of 1700 (Pacific Network, 2017). Some aseismic slip is thought to occur at depth.

4.2 Previous studies

One of the first direct seismic images of the Cascadia subduction zone was produced using receiver functions, specifically teleseismic P-wave conversions, by Langston (1981). He identified the crust-mantle-boundary, the Moho, of the Juan de Fuca plate at 40-50 km depth beneath Corvallis, Oregon, dipping eastward at 20 degrees (Rondenay et al., 2001). Weaver and Michaelson (1985) found abnormally low crustal seismicity in the forearc of the southern part of the subduction zone, compared to the northern part. They attribute this to a segmentation of the dipping plate, where the southern part is believed to be less coupled. A Magnetotelluric

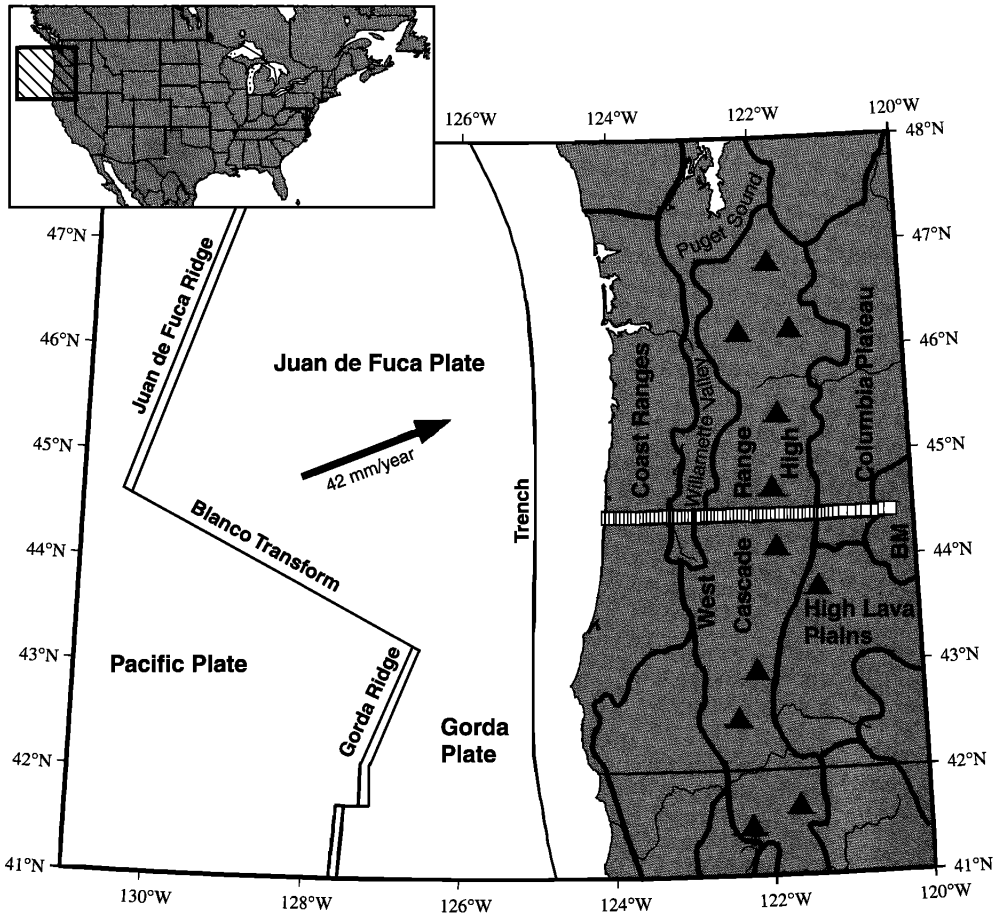

Figure 4.1: Tectonic map of the Cascadia subduction zone (Rondenay et al., 2001).

survey was conducted by Wannamaker (1989). He set out to identify the major features of the subduction zone system as determined by the resistivity. In this survey he identified highly conductive areas in the forearc mantle, which he attributed to the presence of fluids within subducting crust (Rondenay et al., 2001).

A range of controlled source seismic studies have later been conducted, among others by Tréhu et al. (1994), on the crustal architecture on the forearc. They identified a low velocity layer dipping beneath the Coast Ranges located on the coast outside Oregon. The layer was interpreted to be 5 to 8 km thick with a landward dip of 13-16 degrees. Another survey of importance was performed by Flueh et al. (1998). They imaged the subduction zone using wide angle reflection and refraction seismic data, and multichannel seismic reflection data, and suggested the presence of extensive dehydration of the oceanic crust at depth. In 1999 Flemming and Tréhu concluded that demagnetization of the subducting oceanic plate below the continental shelf, inferred by magnetotelluric surveys, could be explained by a hydrothermal alteration, a mineralogical change occurring from interaction with hot water-based fluids (Fleming and Tréhu, 1999).

In 2002 Bostock et al. confirmed very low shear velocities in the cold forearc mantle-Bostock et al. (2002). They concluded this based on the inverted continental Moho discontinuity, a transition from fast to slow as opposed to the expected slow to fast transition associated with the mantle discontinuity Bostock et al. (2002). Audet et al. (2010) demonstrated that the Poisson's ratio in the low velocity zone was unusually high, $\rho = 0.4$. Elastic properties on this scale can not be attributed to lithology, or physical characteristics, alone. A Poisson's ratio of this scale must involve fluids and a high pore-pressure, in addition to very low S-velocities Bostock (2012). A progressive weakening of the velocity contrast starting at 45 km depth, disappearing completely at 100 km depth, was identified by Rondenay et al. (2008). Bostock attributes the change in velocity to eclogitization, a release of fluids hydrating the mantle forearc (Bostock, 2012). He proposes that the absence of a sharp velocity contrast in the mantle forearc is due to such an extensive eclogitization that the rheology of the forearc mantle is comparable to the rheology of the lower continental crust, in some cases reducing the seismic velocities to such an extent that it justifies an inversion of the continental Moho discontinuity above the mantle forearc. In 2014 Wannamaker et al. (2014) repeated the study of 1989 (Wannamaker, 1989), a magnetotelluric study that concluded on 'low resistivity fluidized zones' in the slab at a depth of 35-40 km, approximately 100 km west of the arc which they interpreted as 'prograde metamorphic fluid release from the subducting slab'.

4.3 Application to the Cascadia subduction zone

The objective of the three-part series, written by Bostock, Shragge and Rondenay in 2001 (Bostock et al., 2001),(Shragge et al., 2001),(Rondenay et al., 2001) (on which this project is based), was to develop a method for formal inversion of the P-wave coda to identify 2D variations in elastic properties. The objective of the third paper in particular, is to apply the method to a dataset (CASC93) provided by the Incorporated Research Institute for Seismology - Program for Array Seismic Studies for the Continental Lithosphere, IRIS-PASSCAL.

The dataset was recorded across central Oregon in 1993 and aims to map the Cascadia subduction zone. The white squares in figure 4.1 indicate receiver positions. The study utilized 44 broadband seismometers, relocated multiple times in the span of a 1 year period, leading to a total of 69 sites and a station spacing of $\sim$5 km. Events were selected based on signal-to-noise ratio for the P-waves and converted P- and S-phases, in a qualitative fashion. As the method estimates perturbations in a 2D plane, we must choose the orientation of the plane of interest in relation to

our dataset. The orientation was chosen based on the available surface features of the subduction zone. The deformation front runs approximately North-South, the orientation of the plane is therefore set to approximately East-West.

The background velocity model should be general enough to be broadly applicable, but specific enough to be an approximately accurate representation of reality. The background velocity model for S-waves chosen by Rondenay et al. (2001) for the application to Cascadia, was an adaptation of the results of a study by Li (1996). This produced a 1D velocity model informed by the World Wide Standardized Seismograph Network station COR (Corvallis, Oregon) and the 2D velocity model associated with the CASC93 dataset. The P-wave velocity model was obtained from the S-velocity model by employing a Poisson ratio of 0.33.

Different scattering modes travel along different ray-paths and with a different particle motion. The information recorded by different scattering modes will therefore differ in how well the information on the medium's material properties is recovered. By weighting mode contribution we are able to remove poorly resolved signals and produce a clearer model. The weights applied to each scattering mode were chosen in an ad hoc fashion.

The method resolves perturbations in seismic velocities in the medium. The model displays the perturbations with a resolution of 2 by 2 km, for a 120 km vertical by 300 km horizontal grid. The perturbations are visualized with a red-to blue colour scale. Red represents a negative perturbation(i.e. slower velocity), while blue represents a positive perturbation(i.e. faster velocity). The method produces a model for each scattering mode, in addition to a compilation model for the perturbations in P- and S-velocity for all events, and a compilation model for all the reverberations.

In the generated models, figure 4.2, Rondenay identified a dipping low-velocity feature located on the left side of the model. He assumed this to be the subducting Juan de Fuca oceanic crust, dipping from $\sim$20 km at the coast to 40 km beneath the volcanic arc with an inferred dip of $\sim$12 degrees and average thickness of about 10 km. At about 40 km the oceanic crust dissipates, while the oceanic mantle appears to continue with a change in dip, now $\sim$27 degrees. This is the, supposed, kink in the slab discussed earlier. A clear slow-to-fast horizontal feature is located on the right in the model at 35-40 km depth. This discontinuity is assumed to be the continental Moho. The features in the central part of the image displaying the beta perturbations appear more ambiguous.

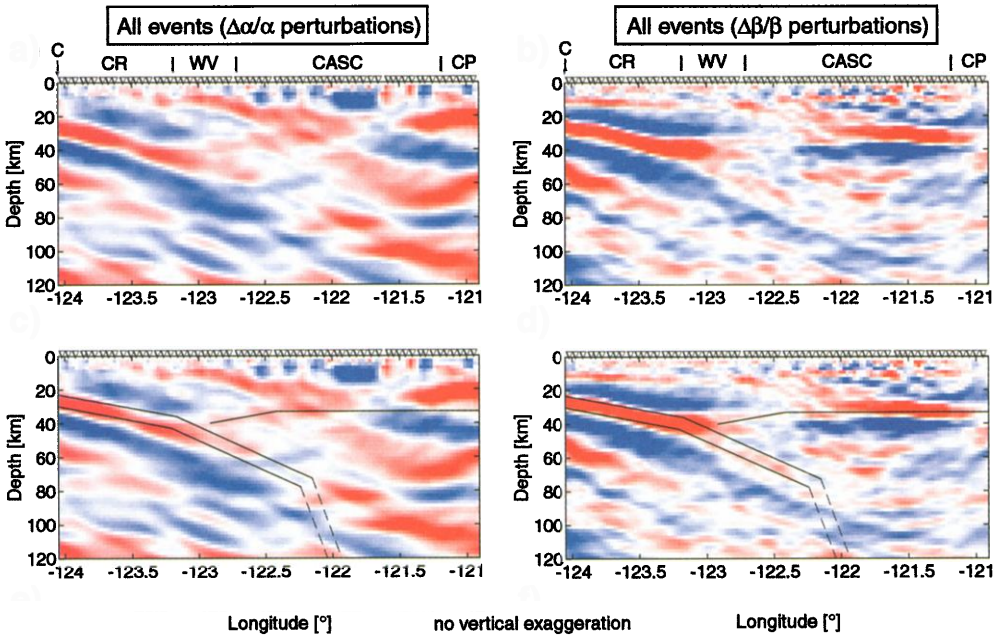

Figure 4.2: Images produced in study by Rondenay et al. (2001), modified.

The dissipation of the oceanic crust at 40 km is associated with a larger change: the oceanic mantle appears to increase in dip and thickness. While Rondenay acknowledges that it might be an erroneous feature, perhaps due to an additional unaccounted for planar structure, he still concludes that the apparent bend of the subducting slab is a real feature. The source of the dissipating oceanic crust and increase in dip angle is in general attributed to one of two scenarios: delamination or dehydration into the overriding mantle, illustrated in figure 4.3.

Delamination refers to the decoupling of the subducting oceanic crust and lower lithosphere. This occurs when the lower oceanic lithosphere is denser than the continental asthenosphere. When the continental asthenosphere comes in contact with the subducting slab, the oceanic crust, being more buoyant than the continental asthenosphere, separates from the remaining oceanic lithosphere and floats along the bottom of the continental lithosphere, while the oceanic lithosphere sinks into the mantle. The consequence of delamination is an increase in slab dip, as the lighter oceanic crust no longer acts as a flotation vessel. Reflective bands discovered in previous studies are found to coincide with a detached oceanic crust redirected towards the surface (Tsumura et al., 1999) or into low-viscosity zones (Rondenay et al., 2001). Given this scenario, the lower velocities would be expected to disappear completely below 40 km, this was not the case in the images generated by Rondenay. This, coupled with the absence of exhumed oceanic crust, were the reasons he dismissed delamination as a viable explanation.

Hydration of the mantle wedge refers to the dehydration of the subducting slab, causing fluids trapped in pores and minerals to enter the continental mantle. The introduction of water in the mantle causes a petrological change as hydrothermal reactions occur (as described in the geological background section 2.4). The serpentinization that occurs on account of the dehydration of the oceanic crust decreases the seismic velocities and increases the resistivity, both in line with the results observed in fig. 4.2. Rondenay proposes that the increase in slab dip might be attributed to an increase in density following the eclogitization.

Rondenay therefore conclude that the thickening and increase of dip of the subducting Juan de Fuca plate is caused by dehydration of the oceanic crust and the associated metamorphic reactions in the oceanic crust increasing the density of the slab.

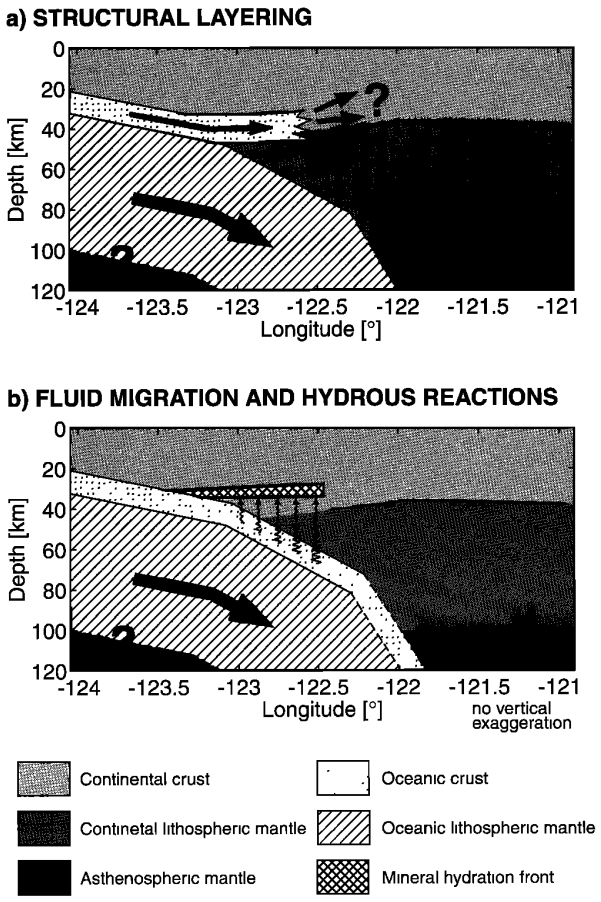

Figure 4.3: Illustration of delamination vs. hydration (Rondenay et al., 2001).

Chapter 5

Methods

5.1 Motivation

Underlying this project are some assumptions about the feasibility of the project and the relationship between the technological development in the project, and the scientific merit of this thesis:

- The implementation of a 2D background velocity model should be possible with the present tools and techniques available. The evaluation of success is therefore reliant upon the degree of improvement rather than the feasibility of the project itself.

- The process of implementation is in itself not central to the scientific aspect of the written thesis. The process is, however, important for comprehension and replicability of the project and will therefore be covered in brief in chapter 5.4, and in detail in appendix A.2.

The original method employed in this project utilized a 1D velocity model as the basis of the proposed model. A 1D velocity model however, is a major simplification of a subduction zone. A poorly fitting velocity model leads to a sub-par stacking of data, as the diffraction hyperbola along which stacking is performed, is estimated based on the background velocity model. An ill fitting diffraction hyperbola results in a model with a high degree of noise, where finer structures might be overlooked. This simplification was a necessity in order to limit the computational demand, but as computational power becomes cheaper and more accessible, this is less of a concern.

The velocity model used by the original method was a 1D model, consisting of a 40 km thick multilayered crust, and mantle below, where the total depth of the velocity model was 300 km. This model provides no horizontal variation in material

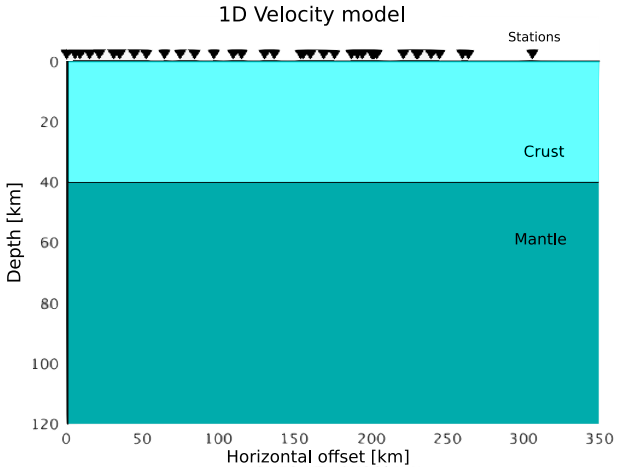

	$\mathbf{P}_{vel}$	$\mathbf{S}_{vel}$	**Density** ρ
	km/s	km/s	g/cm^3
Crust	6.46	3.80	2.80
Mantle	8.05	4.50	3.20

Figure 5.1: Illustration of 1D velocity model, with table of parameters, as used by Rondenay et al. (2001)

parameters and, as such may be seen as an oversimplification. A subduction zone can not be simplified to a strict 1D medium without significant problems.

A 2D velocity model would take into account a dipping oceanic crust and permit an optional low-velocity mantle wedge. In this thesis, I account for both, by creating two similar, but distinct, 2D velocity models. A 2D model should allow us to better approximate the correct travel times and allow us to do a more reliable evaluation of the inferred property perturbations, but will unfortunately necessitate an increase in computational demand.

A 3D model would of course facilitate all the same solutions as a 2D model, with relatively little gain (due to the approximately 2D geometry of a subduction zone in the upper mantle), but with an additional computational increase. The mathematical solution is more complicated, as an additional angle of movement must be taken into account. This leads to an additional increase in the amount of computations and less transitive sections from the original 1D case.

This thesis mainly describes a proof of concept, and as such the complication afforded by the 3D case is unnecessary to achieve the goals of the project. Further, in keeping with the tenets of the scientific approach, it is natural to first make a solution for the simplest possible case, and then make incremental adjustments and improvements to incorporate a higher level of accuracy. Developing the method to account for a 2D background velocity model is therefore a natural next step. The tools created as part of this project are therefore not designed to handle a 3D model, but they have been designed with a possible future implementation of a 3D medium in mind.

5.2 Research method

In an effort to keep as much of the original computations as possible, it was determined that the best approach to implementing the 2D velocity model was to implement a series of unique 1D velocity models, each corresponding to the travel path of each ray.

This was considered the most reasonable approach, as it required few structural changes to the migration algorithm, while maintaining the accuracy provided by a 2D velocity model. A vital assumption in this approach is that the algorithm expects the material parameters to vary as a function of depth. Adhering to this constraint was determined a more productive, less invasive, approach to implementing the 2D velocity model, than requiring the method to accept a new type of input which would most likely require extensive changes to both the method and the implementation. This was not considered feasible within the scope of a Master thesis.

The unique 1D velocity models were created by ray-tracing through the 2D velocity model, and storing the depth information at each interface along with the properties of each layer, see figure 5.2. The process of ray tracing will be explained in detail later in section 5.4.3.

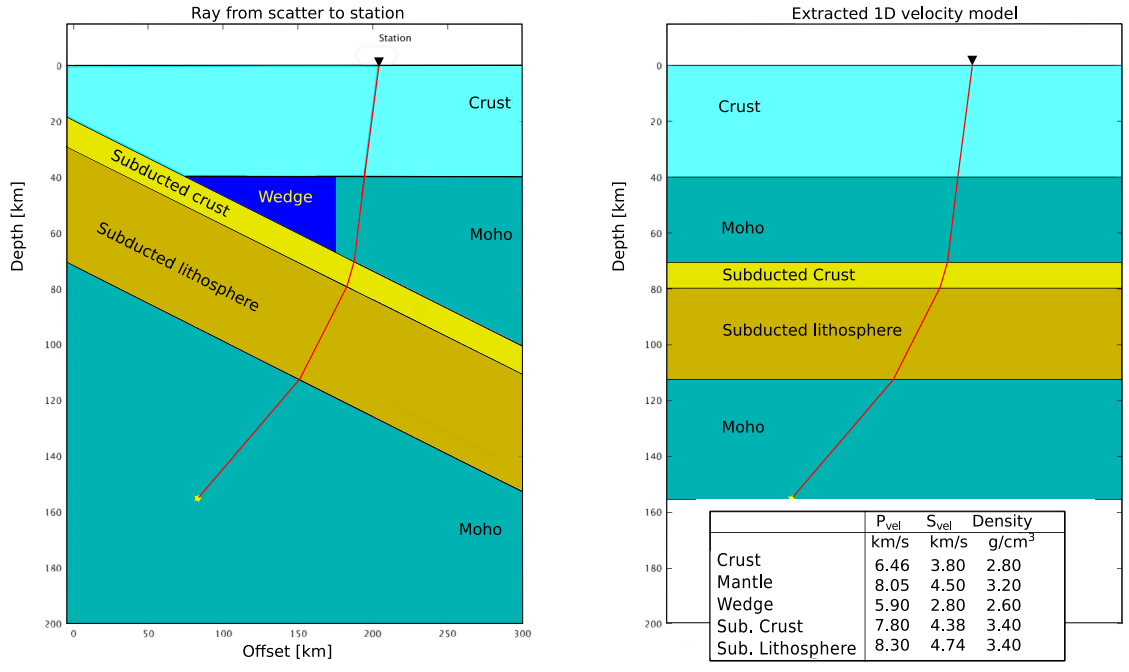

Figure 5.2: Illustration of conversion from ray path through 2D velocity model to a 1D velocity model.

Keeping as much of the original code as possible, allow us to attribute the changes in the produced images to the change of background velocity model rather than the structural or mathematical changes in the method, as well as minimizing the potential errors and bugs that would occur throughout this project.

5.2.1 Evaluation

The object of this thesis is to solve a scientific question, by utilizing and expanding upon present tools, as well as developing new tools as part of the project. The tools developed are inherently an important part of the project, but not of the thesis, as the focus in the thesis is on the scientific method and the scientific results. The images produced by the tools will be evaluated using a qualitative approach, comparing the original images and the images generated by the new method, as well as the computational demand of the new method.

5.3 Objectives

Below, I will detail the specific objectives of this study, and the method that will be employed to obtain these.

The first objective is to recreate the original images for a set of test data, using the new method. Ray tracing through the original 1D velocity model should generate the same 1D velocity model for each ray path, identical to the original 1D velocity model, and thus produce images identical to those of the original method. Recreating the original images using a 1D model should ensure that all changes to the images produced using the 2D model, can be attributed to the actual 2D velocity model.

The second objective is to apply the new method to synthetic data, still comparing the original method and the new method, both incorporating the original 1D velocity model, to identify any discrepancies. We apply the method to a synthetic data set to correctly evaluate the accuracy of the method and what to expect and evaluate, when applying the method to real data sets. The synthetic data is generated for two separate cases, incorporating a slow mantle wedge and a fast mantle wedge. The dataset is generated by Felix Halpaap using the software specfem. Specfem is a tool utilizing a spectral element method to simulate the propagation of elastic waves through a realistic medium (Komatitsch and Vilotte, 1998). It incorporates

free-surface topography and it is an efficient and flexible tool for studying diffracted waves in a 2D or 3D medium. Halpaap modeled the response of 10 ray parameters ([0.04, 0.05, 0.06, 0.07, 0.08, -0.04, -0.05, -0.06, -0.07, -0.08]), corresponding to ten individual seismic events,arriving from both directions, within the 2D plane. It utilizes 61 seismometers with a 5 km spacing between 100 and 400 km. The geometry of the velocity model used for generating the synthetic data was restricted to a geometry easily available through specfem, but the properties of the medium were set to resemble the 2D velocity model appropriated from Bostock et al. (2002). See figure 5.3 for an illustration of the velocity model used for the synthetic dataset.

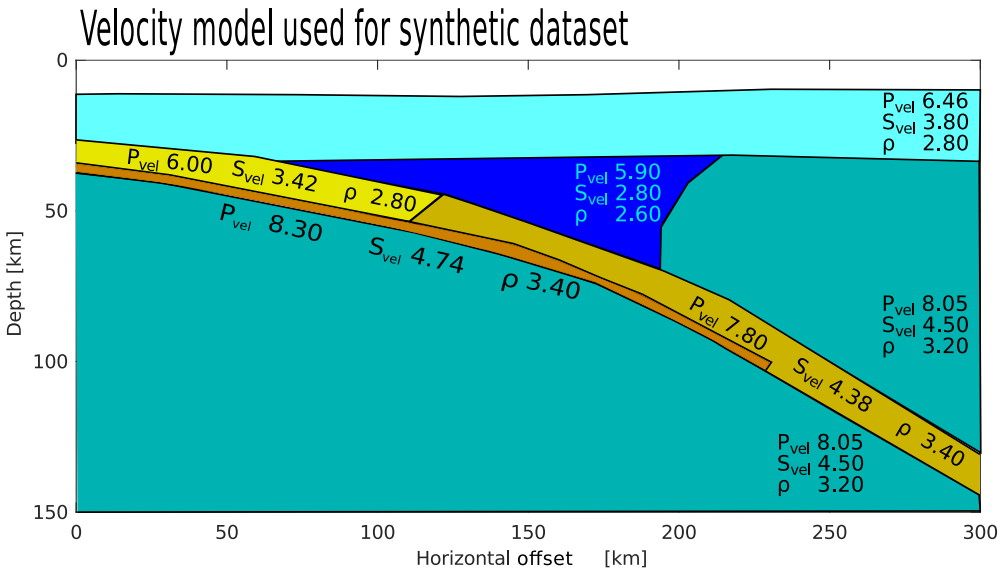

Figure 5.3: Illustration of 2D velocity model used for generating synthetic dataset.

The data is then tested for the 2D background velocity model, using two sets of data, both with and without a serpentinized/slower mantle wedge. The success of the synthetic tests are evaluated based on how the images generated adhere to the velocity model used for generating the synthetic datasets. The focus of the evaluation is on the accuracy of the dip of the subduction zone and the constrainment of the mantle wedge.

The final objective is to apply the new method to a real dataset from the Cascadia subduction zone, comparing the images generated by the original method and the new method for a series of background velocity models. The focus of the real test is to observe and evaluate whether the changes identified in the synthetic tests can be identified in the real models as well.

5.4 Implementation

5.4.1 Overview

Incorporating a range of bespoke 1D velocity models is comparable to incorporating a single 2D velocity model, as the only parameters that are relevant on any given occasion, are the parameters along the ray path. Unfortunately, the 1D velocity model contains no information about the dip at each interface, neither is the method developed to take dipping layers into account, so it is still an approximation. The take-off angle and incidence angles along the ray paths will therefore be lost in the conversion. The take-off angle must be recalculated for each new, unique 1D velocity model with horizontal layers. This is because the take-off angle is affected by dipping layers, and the method requires the specific take-off angle from the scatter-point to a specific station, given horizontal layers.

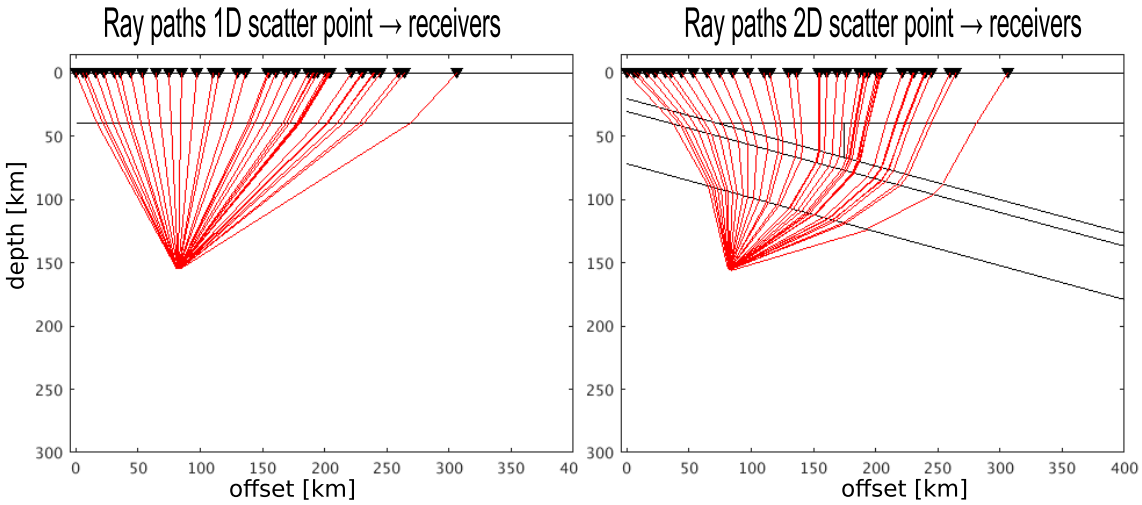

Figure 5.4: Illustration of the effect of a 2D velocity model on the ray paths.

Each ray path is determined based on the geometry of a unique combination of event, scattering-point and receiver. This creates a multitude of ray paths which are incorporated into the algorithm by iterating the corresponding sections for each event, scattering-point and receiver.

The GRT-inversion uses both the incident and scattered waves in the migration. The event-receiver ray path may vary greatly from the event scatterer-receiver ray

path. Based on this, we utilize two unique velocity model for each event-scatterer-receiver combination, one for the incident wave, and one for the scattered wave. As we are only interested in scattered energy after it has been scattered, we only trace the ray from the scatter-point to the receiver.

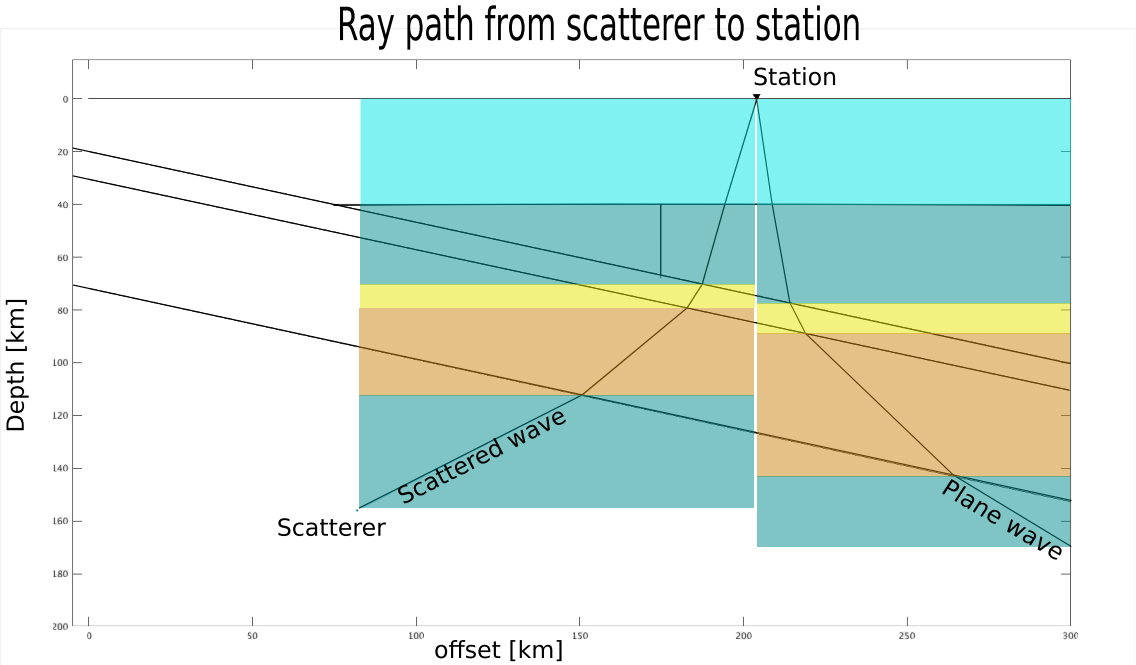

Figure 5.5: Illustration of ray path, and overlay of resulting 1D velocity model, associated with the plane wave and the scattered wave.

The ray paths of the scattered energy are independent of the direction of the incoming energy, allowing for reuse of the same scatterer-receiver ray paths for all incoming events, which reduces the computational demand. Based on this, we are interested in the ray path to all stations from each scatterer and storing these in a table for easy access. The event-receiver ray path associated with the plane incident wave is still unique and must be retraced for each iteration. The ray path is determined based on the receiver position and the horizontal slowness associated with the event.

The implementation requires a 2D velocity model, a ray tracer to obtain the bespoke 1D velocity models for each ray paths, and a change of loop structure in the original code. Most parameters are calculated directly, as needed, in contrast to the original calculations, where many parameters were obtained by interpolating across values obtained by referencing a table. This increases the computational demand as there is a vast increase in the number of calculations, but the elimination of many interpolation-operations should lead to more accurate values, even using the original 1D model. The reduction of interpolation will also provide a reduction in computational demand in certain sections, but not enough to combat the increase caused by the number of new calculations.

5.4.2 2D velocity model

The 2D velocity model I am using for this thesis was adapted from an image generated by Bostock et al. (2002), figure 5.6. The image is the result of a survey of the Cascadia subduction zone conducted in 1993-1994. The top image displays the perturbations in S-velocity with respect to a smoothly varying one dimensional reference model, this is the same image as described in section 4.3. The middle image displays a thermal model constructed based on the top image. The bottom image displays the interpretation of the top image. The velocity model I am using is a simplification of the interpreted results obtained in the Bostock study.

The 2D model is a improvement from the simple 1D velocity model, as it takes into account a dipping interface and a mantle wedge, in addition to the original crustal lithosphere and underlying mantle. The model still makes simplifying assumptions though, such as linear, sharp interfaces, a homogeneous medium within the set boundaries, and a generally isotropic model. The new dipping slab is 50 km thick, consisting of 10 km oceanic crust and 40 km asthenosphere. The kink, as interpreted by Rondenay et al. (2001), has been ignored for this new proposed velocity model, as the kink adds an additional complicating element to the project, and its assumed existence might turn out to be caused by the assumption of a 1D structure. The slab is dipping at 15 degrees, measured against the horizontal, in the inland direction. Bostock et al. (2002) references a 10 degree dip above 45 km and a 30 degree dip below 45 km. The mantle wedge is assumed to start below the crust with a total width of 100 km.

The material parameters P-velocity(α), S-velocity(β) and density(ρ) are assigned to each structure based on commonly used values and suggestions from Rondenay. The velocity model has been generated for an area that is 350 km wide and 350 km deep. The interfaces are stored as lines using two points of intersection, for easy ray-tracing. The greatest effect on the results of a 2D implementation, is suspected to be the introduction of a mantle wedge, the area of the greatest variance in seismic properties, from the original 1D model. Two velocity models are therefore generated, one with a fast mantle wedge and one with a slow mantle wedge. In the case of the fast mantle wedge the seismic properties of the mantle wedge is set to that of the surrounding mantle, indicating 0% serpentinization. In the case of the slow mantle wedge the seismic properties are set to extremely low values, to accentuate the variance from the 1D model, equivalent to a serpentinization degree of $\sim 80\%$, in line with figure 2.3.

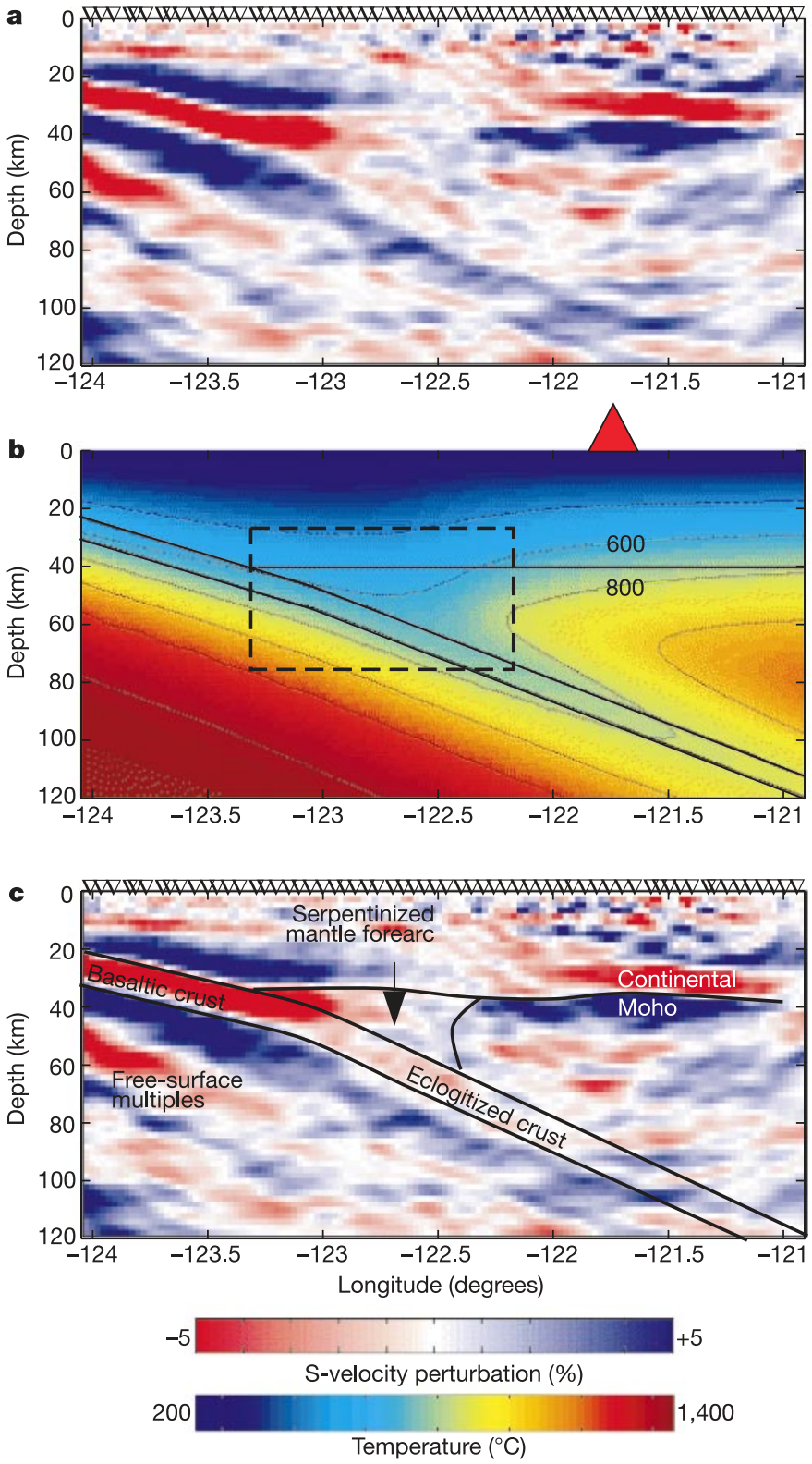

Figure 5.6: Image and thermal model of the Cascadia subduction zone (Bostock et al., 2002).

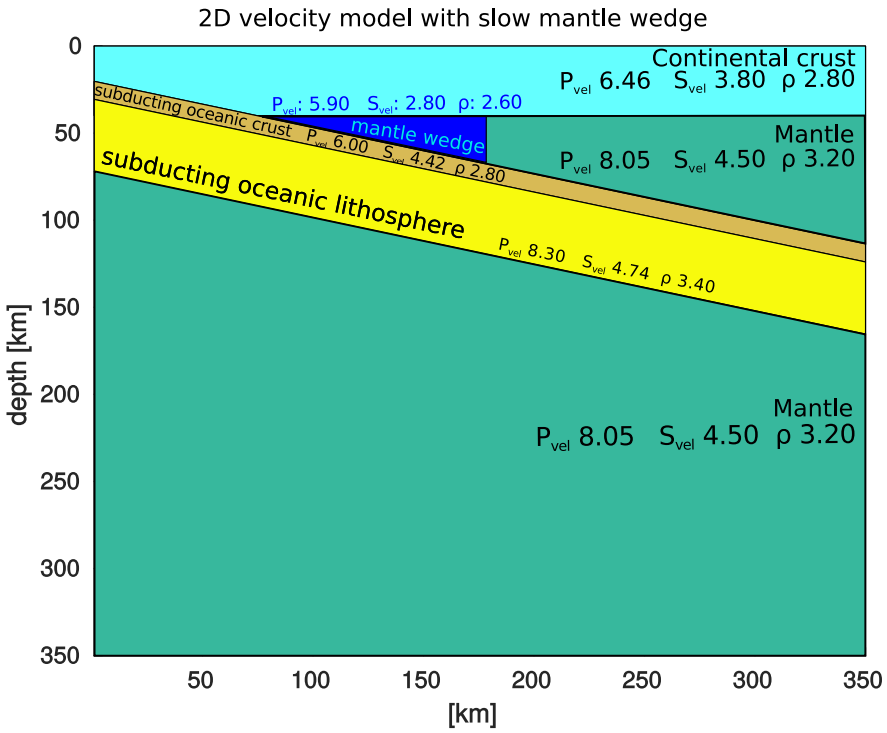

Figure 5.7: Illustration of 2D velocity model with a slow mantle wedge.

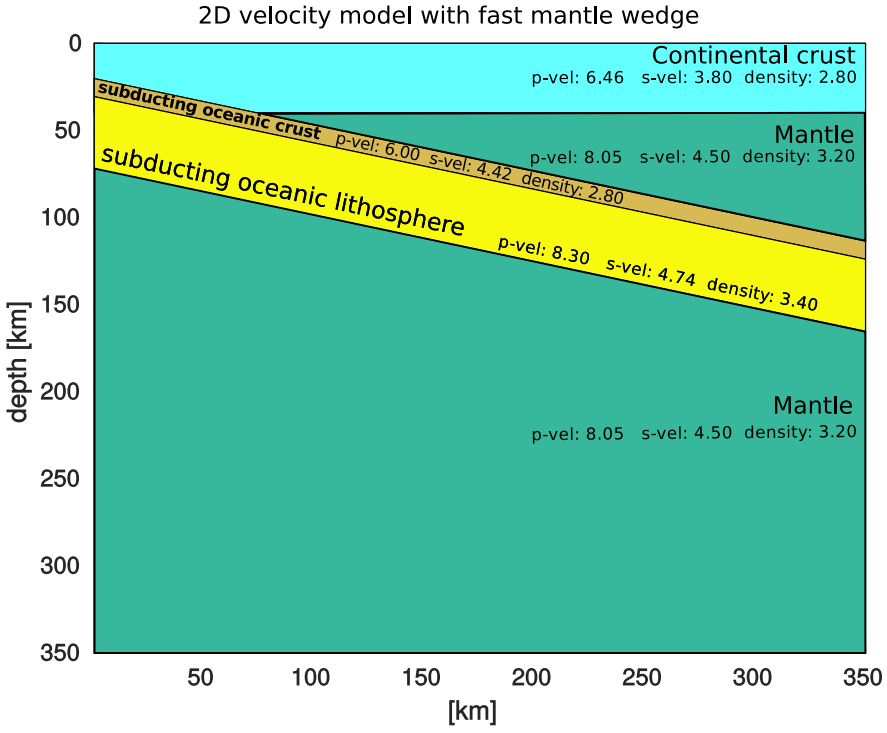

Figure 5.8: Illustration of 2D velocity model with no mantle wedge.

	p-vel	s-vel	density
	km/s	km/s	g/cm^3
Crust	6.46	3.80	2.80
Mantle	8.05	4.50	3.20
Wedge	5.90	2.80	2.60
Sub. Crust	7.80	4.38	3.40
Sub. Lithosphere	8.30	4.74	3.40

Figure 5.9: Table of parameters used in the new 2D velocity model. (The wedge is omitted in figure 5.8).

Application to the synthetic dataset

As the velocity model used to generate the synthetic dataset did not consider a continental asthenosphere, this was removed for the application of the method to the synthetic dataset. Mantle properties were instead assumed. The synthetic dataset assumed a transition in seismic properties at 50 km depth, to higher values, here set to the values I presumed for the oceanic asthenosphere. As I assume a continuous oceanic crust I set the values of the slab equal to the upper subducting slab, as this is the area of greatest interest. The subducting oceanic crust were set to the upper crustal velocities. These changes were set in place to utilize a velocity model that approximates the velocity model used to generate the synthetic dataset as close as possible, while still adhering to the constraints set in place for the ray tracer.

Application to the real Cascadia dataset

The original method, when applied to the Cascadia dataset, utilized a more complex 1D velocity model than the simple, two layered model associated with the test data for which the 2D velocity model was developed. The more complex 1D velocity model contained a total of seven unique layers, all within the crust, see table in figure 5.10. Tests proved that this provided a significant improvement to the produced models. The velocity model used for the application to the Cascadia dataset is therefore a combination of the two models. The continental crust in the generated 2D model is divided into seven layers adhering to the depths and properties of the original multi layered 1D velocity model used. The properties of the mantle in the multilayered model was also adopted.

As the seismic velocities assigned to the slow mantle wedge might be unrealistically low, an additional 2D velocity model with seismic velocities representing a more realistic serpentinization degree is included. The serpentinization in this 2D velocity model is set to $\sim$ 50 % serpentinization. Again using the diagram gen-

	depth km	**p-vel** km/s	**s-vel** km/s	**density** g/cm^3
Crust 1	0-5	5.50	2.77	2.60
Crust 2	5-8	6.35	3.20	2.60
Crust 3	8-11	6.47	3.26	2.90
Crust 4	11-16	6.67	3.36	3.10
Crust 5	16-21	6.75	3.40	3.10
Crust 6	21-25	6.93	3.49	3.10
Crust 7	25-40	7.16	3.61	3.10
Mantle	40-300	8.10	4.33	3.50

Figure 5.10: Table containing the values of the complex 1D velocity model.

erated by Hyndman and Peacock (2003), using values found in laboratory conditions found by Christensen (1966). Reasonable seismic velocities were found to be $P_{vel} = 6.20km/s$, $S_{vel} = 3.20km/s$ and density was kept at $\rho = 2.60g/cm^2$. This velocity model was added in order to compare the images generated from the new method with results of previous studies, using images generated based on more realistic values.

5.4.3 Ray Tracer

The objective of the 2D ray tracer is to find the 1D velocity models bespoke to the ray path between a source-point and the receivers in a 2D velocity model. To determine the ray paths, I created a simple ray-tracer.

Given a source position and a take-off angle, the ray tracer is able to trace the ray path from the source position to the surface, bending in accordance with Snell's law. The tracer runs through an iterative process in which it calculates the intersection between the line defined by the source-position and given take-off angle, and the line that describes the model interface. The new intersection is the point at which the ray hits this interface. This is set as a new 'source'-point and a new take-off angle is determined by first estimating the incidence angle with regards to the dipping surface and then applying Snell's law. This process is repeated until the ray hits the surface, is critically reflected or excessively out of bounds of our velocity model. Some deviation from the defined horizontal extent of the model is tolerable, and even encouraged, as there is a receiver at 0 km offset, and rays hitting at negative offset are therefore required for the interpolation to work properly. As the model consists of lines, the lines extend indefinitely. As long as the intersection between the ray and the interfaces are within a reasonable horizontal offset, here set at [-250,600], the ray path is accepted as reasonable. The ray tracer does not tolerate downward propagating rays.

The ray tracer is utilized to find the 1D velocity models needed to calculate the travel time of the incident plane wave and the scattered waves. This ray tracer works well for the incident plane wave when modified to trace from the receiver and backwards toward the event. For the scattered rays, we do not know the correct scattering angle necessary to reach the exact position of the receiver prior to ray tracing. To circumvent this, we trace a series of ray paths from the scatter-point and outwards, with a take off angles set to 201 values in the range of $[-\pi/2 : \pi/2]$. From this, we get a series of points where the ray hits the surface. From these surface positions we interpolate for the station positions, obtaining the ray path required to reach the station, see illustration figure 5.11. This ray path is then converted into a 1D velocity model, illustration figure 5.12.

The scattering angle, the take-off-angle at the scatter-point against the vertical, is required for some of the calculations. The scattering-angle depends on the dip of the layers in the velocity model. As we have now obtained a 1D velocity model with no dip, the ray path needs to be recalculated through our new 1D velocity model. An illustration of the retraced ray path is illustrated in pink in figure 5.12, this illustration is, however, an exageration in terms of change in scattering angle θ. The actual retraced ray deviates less from the original ray path, an exaggeration was done for illustrative purposes. Retracing the ray will insure a correct scattering angle, θ, for later calculations.

This process is iterated for the ray paths corresponding to both the P-wave and the S-wave for the scattered waves. The incident wave is by design a teleseismic P-wave and only the P-ray path is therefore obtained.

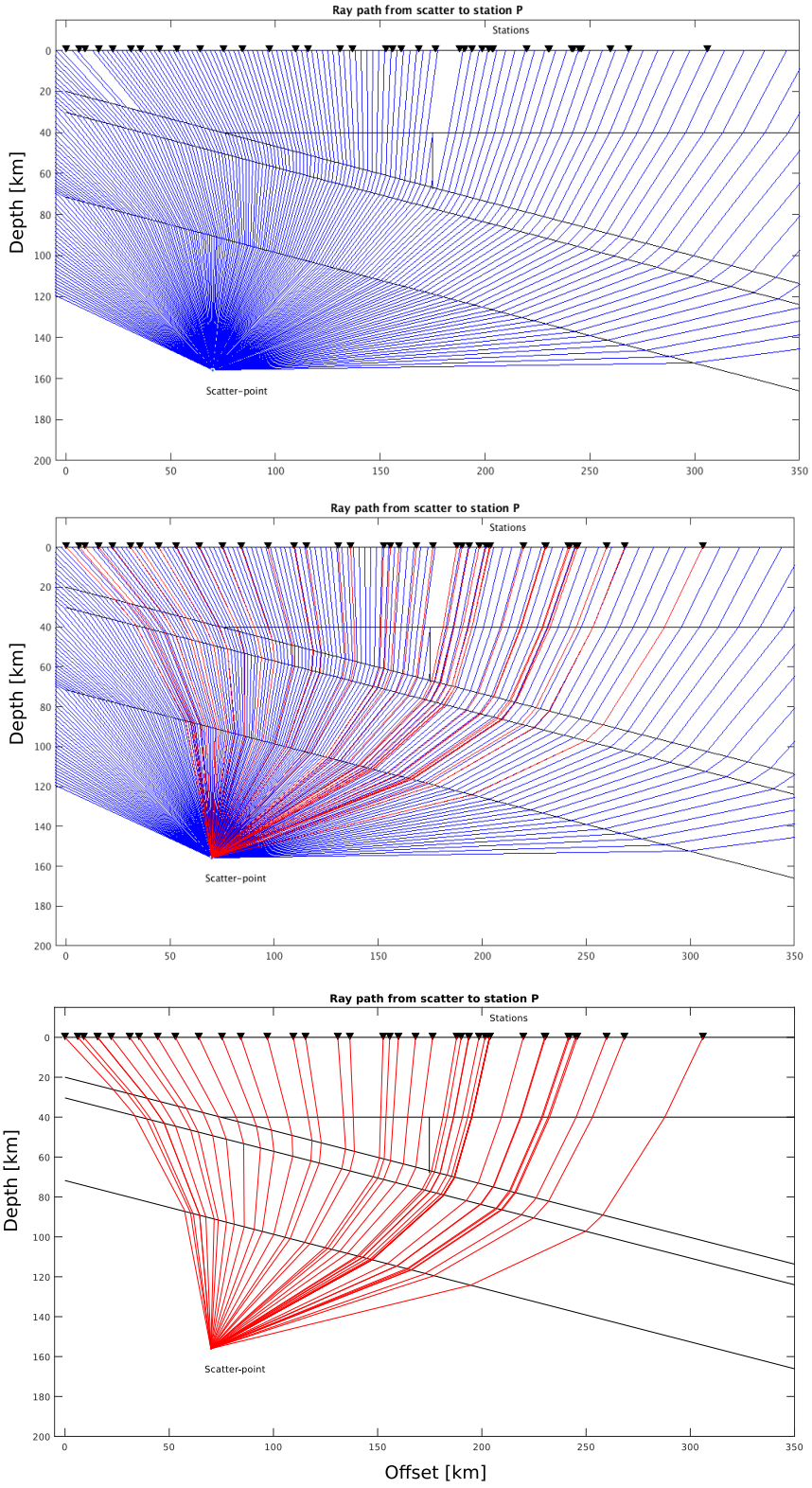

Figure 5.11: Illustration of interpolation.

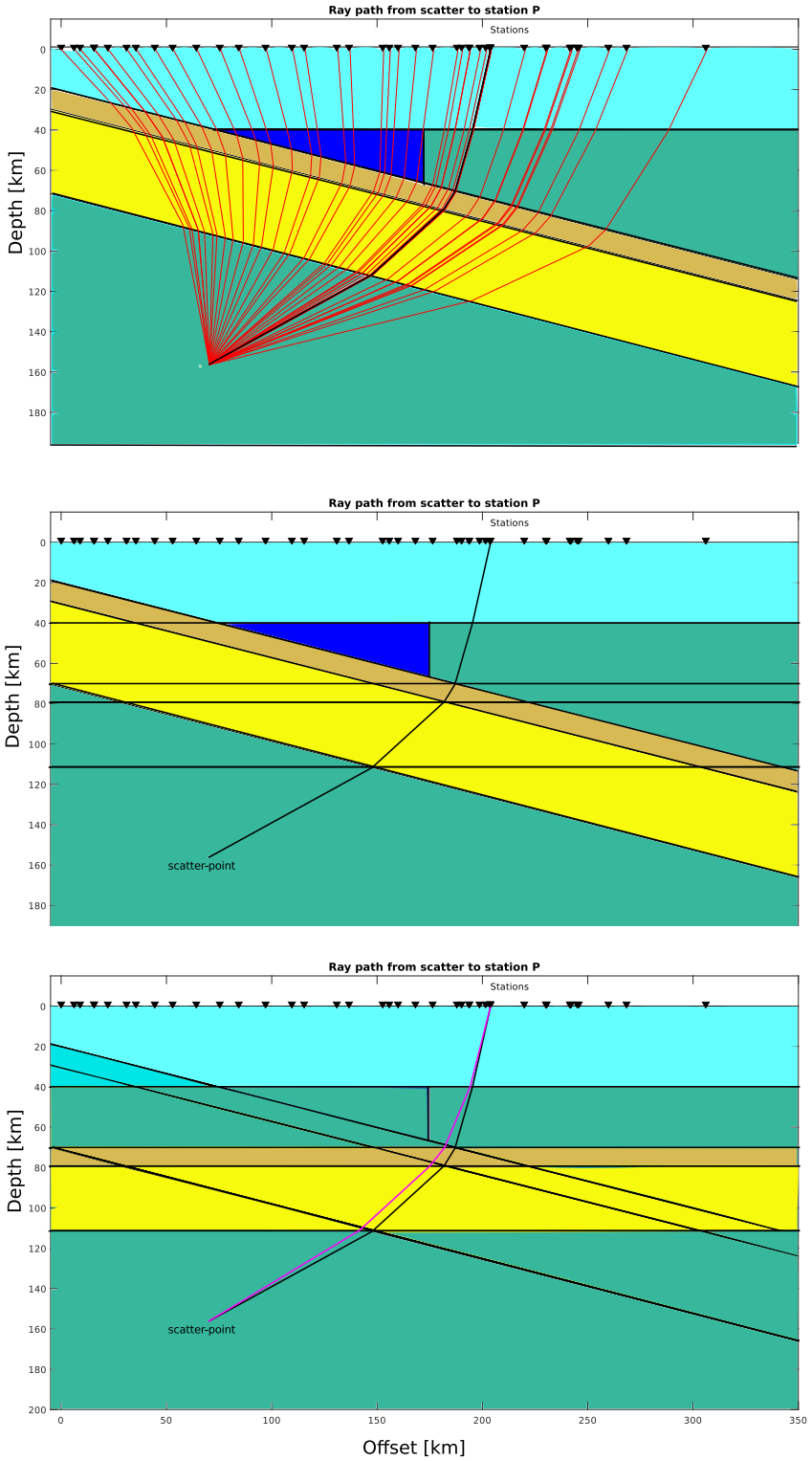

Figure 5.12: Illustration of conversion from ray path to 1D velocity model.

Technical implementation

The technical implementation of the ray tracer function may be divided into five steps:

1. Ray tracing through the model from the scattering point using the scattering angle range to obtain the points where the ray intersects with the layers of the 2D model and generate a 1D velocity model.

2. Expand the obtained 1D velocity model to prepare for subsequent interpolation.

3. Interpolate across the surface positions obtained to obtain the values associated with the station positions.

4. Contract the values associated with the station positions to obtain 1D velocity models corresponding to the scatter point station combination, to make it usable for the migration.

5. Finally retrace through the final 1D velocity model to obtain the correct scattering angles.

Next is a detailed explanation on each step.

Step 1: Ray tracing through the 2D velocity model

The objective of the first step is to find a velocity model corresponding to a range of take of angles, θ. To do this, we set the source position to slightly off the scatter point to avoid potential issues that may arise when doing the interpolation.

From the source position and take off angle, we determine the linear equation describing the ray, and from the velocity model, we get the linear equation describing the interface.

$$\text{Ray:} \qquad a_r t + b_r = k \tag{5.1}$$

$$\text{Interface:} \qquad a_l t + b_l = k \tag{5.2}$$

$$a_r = [cos(\theta), sin(\theta)] \qquad b_r = [z_s, x_s] \tag{5.3}$$

$$a_l = [L_{i,3} - L_{i,1}, L_{i,4} - L_{i,2}] \qquad b_l = [L_{i,3}, L_{i,4}] \tag{5.4}$$

In these equations, t and k are unknowns, L is a matrix associated with the velocity model containing the coordinates of the end points defining the interfaces. i is the index for looping over the layers in the model. We find the intersection point between the two lines by setting the equation describing the ray equal to the equation describing the interfaces and solving for t. The intersection point is where the ray originating from the source point would hit the interface, given the take-off angle. We substitute t by the obtained value, to find z and x coordinates of the intersection.

$$\begin{pmatrix} a_{r,1} \\ a_{r,2} \end{pmatrix} t + \begin{pmatrix} b_{r,1} \\ b_{r,2} \end{pmatrix} = \begin{pmatrix} a_{l,1} \\ a_{l,2} \end{pmatrix} k + \begin{pmatrix} b_{l,1} \\ b_{l,2} \end{pmatrix} \tag{5.5}$$

$$t = \frac{b_{l,1} - b_{r,1} + \frac{a_{l,1}}{a_{l,2}}(b_{r,2} - b_{l,2})}{a_{r,1} - \frac{a_{l,1}}{a_{l,2}} a_{r,2}} \tag{5.6}$$

$$z_{new} = a_{r,1} t + b_{r,1} \qquad x_{new} = a_{r,2} t + b_{r,2} \tag{5.7}$$

The intersection point is saved to the ray path matrix and set as the new source point. The incidence angle when hitting a dipping layer is corrected using equation 5.8

$$\theta_i = \sin^{-1}\left(\frac{a_l \cdot a_r}{|a_l||a_r|}\right) \tag{5.8}$$

We find which layer the ray will be moving through next based on the current spatial position, and use the properties of this layer and the previous layer to determine the new take off angle using Snell's law.

All substeps of step 1 are repeated for each layer/interface until the surface is reached.

Step 2: Expanding the velocity model to prepare for interpolation

The next step is to prepare the obtained velocity models for interpolation. As different rays may go through a different number of layers, interpolating to find the correct velocity model is a bit less straightforward. All velocity models corresponding to scatter points are transformed to similar multilayered models. The thickness of each layer of these velocity models is set to $\sim$1 km. As all originate from the same depth, this results in the same number of layers, suitable for interpolation.

Based on the upper and lower extent of each layer we create an array corresponding to depth $[zmin : 1 : zmax]$ and an array corresponding to the horizontal position for each depth increment (1 x for each z on the interval $[xmin : xmax]$), and we create arrays of the P-velocity, S-velocity, density(ρ) and layer number with equal values for all indices of the array corresponding to a length of z. We combine the transform of these arrays to create the expanded velocity model, by concatenating the set of arrays into a matrix. This is repeated for each layer, and generates a velocity model where each row of the matrix corresponds to a 1 km thick slice of the 1D medium, unique to the traced ray.

Step 3: Interpolate expanded velocity model to find ray path to station

In this step we do the actual interpolation. As one row in the velocity model matrix corresponds to 1 km horizontal slice of the model, we interpolate the values associated with the positions on the surface for receiver positions, for each layer in the velocity model.

The spatial parameters are interpolated using linear interpolation, and the material parameters are interpolated using nearest-neighbour interpolation. This was done to keep the distinct material parameter values, but get the most accurate spatial points. If the receiver position is located outside of the range of the traced surface positions, the ray path is set to be the nearest, most extreme feasible ray path. This is to avoid any unnatural ray paths.

Step 4: Contract interpolated expanded velocity model to as few layers as possible

To obtain a usable velocity model, consisting of the original layers, the model must be contracted. As some of the calculations in the method require a summation over layers, for instance the calculation of traveltime and other parameters, a contraction is necessary to limit the computational demand of the method.

The model was contracted by identifying the unique numbers in the layer number array and the indices of the their first occurrences. The spatial position of the layer corresponding to the index of the first and last occurrence of each unique number, corresponding to the entire layer, were extracted to create the spatial points of the velocity model. The material parameters were extracted from the line corresponding to the median of the layer, by averaging the index corresponding to first and last occurrence of the layer.

Step 5: Retrace through the 1D velocity model to obtain the correct scattering angle

As the dip of the layers affect the path of the ray, and thus the scattering angle, the ray must be retraced through the new 1D model to find the correct scattering angle required by the method. This is found using the same algorithm as explained in step 1, bypassing the step of correcting for dip, and the check of spatial position for the parameters of the next layer, for an increase in computational speed.

Exception

A major exception in the ray tracer is the top crustal layer. As ray tracing outwards from 2 km depth would make it difficult to get a range vast enough to reach the majority of the stations, and as the first layer contains no diffraction, the first layer is treated as a homogeneous half-space model. The scattering angle is calculated directly using Pythagoras theorem. The spatial positions are set to the receiver and scatterer position, while the material parameters are set to the material parameters of the first layer.

5.4.4 Modifications to existing structure

With the tools required to implement the new 2D velocity model, all that is left to do is to make the necessary modifications to the structure of the original method. The original structure, algorithms and flow of the code provided for project was reverse engineered to identify the key parts and natural progression of the computations. A detailed overview of these results may be found in appendix A.2. From this it was determined that the sections that needed to be modified were the scripts *prep_table.m*, *plane_wave_alt.m* and *migration.m*, as these are the scripts that reference the velocity model parameters directly, see figure 5.13. *Prep_table.m* and *plane_wave_alt.m* needed to be modified to take into account the new velocity models, while migration needed to be modified as some parameters now are varying with each iteration.

In the script *prep_table.m*, the travel time, slowness and Jacobian associated with the scattered waves are calculated. The specific calculations are kept, but the input is changed as it now needs to reference a new velocity model for each iteration. The ray tracing script determining the unique 1D velocity models is implemented to find the velocity model associated with the P-wave ray path and S-wave ray path. As this script is designed to be run separately from the main process, information on the events are not available to the script. The parameters are therefore calculated for a series of ray-parameters (51 values in the range [0:0.008]) and stored in a table.

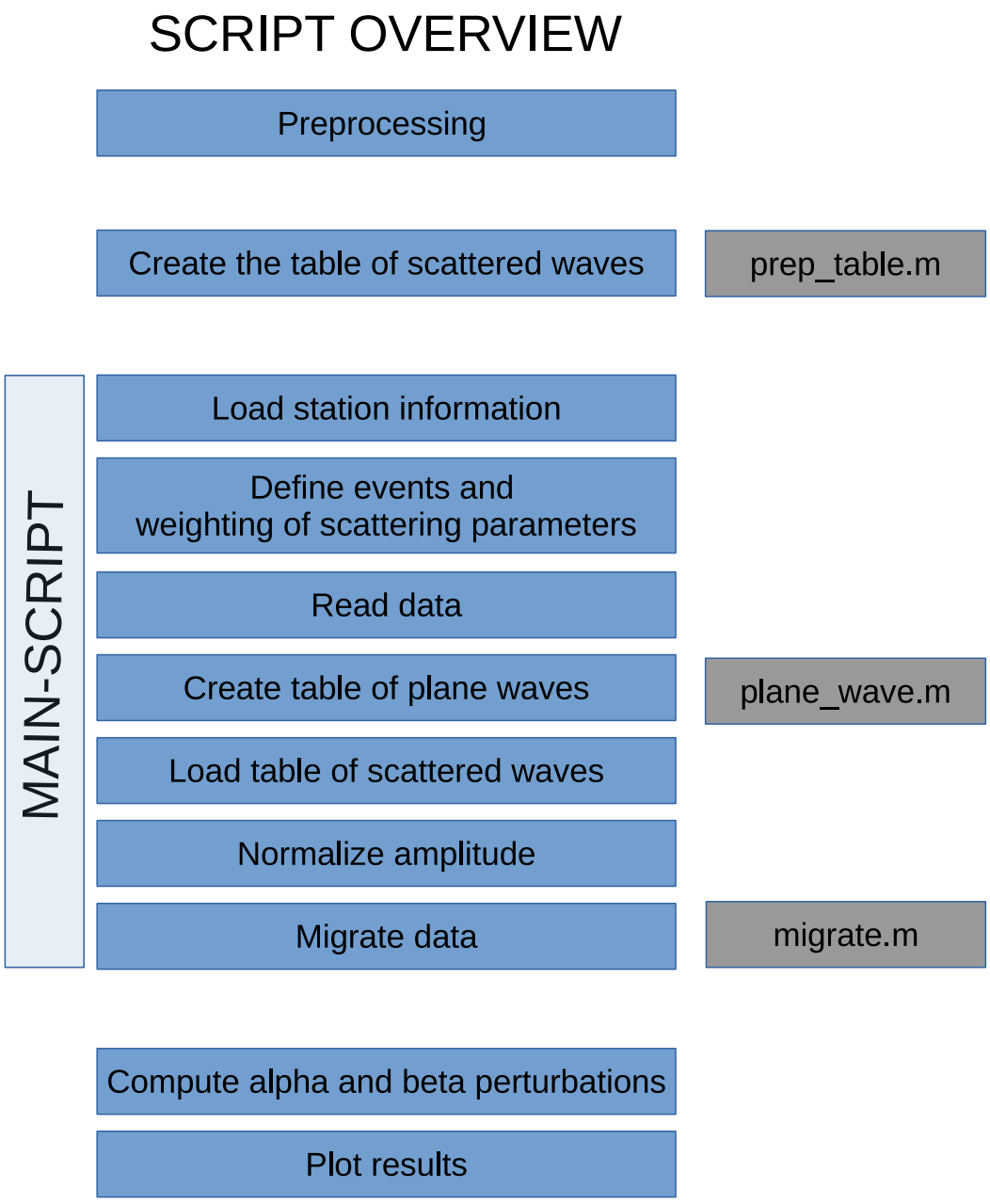

Figure 5.13: Flowchart overview of the structure. The locations of the three scripts highlighted is indicated on the right.

The correct parameters may then be found through interpolation when needed. This is still a reduction of interpolations, as the former method required an interpolation for station, event, scattering-angle and scatter-point.

In the script *plane_wave_alt.m*, the traveltimes to the scatter point of the incident plane wave, as well as the incident plane wave reverberated at the free surface, both as a P-wave and as a S-wave, are calculated. Most computations are kept, but the script is converted to a function, calculating the travel times of the incident wave with the variables provided, as needed. Backwards ray tracing is incorporated and performed for each iteration based on the ray parameter of the specific event and the receiver position. All interpolations formerly associated with the incident plane wave are removed.

To the script *migration.m*, minor changes were made to the computations. The interpolations associated with the plane wave were removed, and the interpolations associated with the scattered wave were substituted for a single interpolation with respect to the ray-parameter of the event. Major structural changes were however put in place in order to recalculate all the required calculations for each iteration.

With all tools developed and all structural changes incorporated, the development part of the project is now described. In the next chapter, I present the images generated by this new method, and a short summary on how the images generated using a 2D velocity model differ from the images generated using a 1D velocity model.

Chapter 6

Results

In this section I will detail all of the outcomes of the new method. This includes preliminary test data used in development, as well as all results of the method applied to synthetic and real data from the Cascadia subduction zone, using various background velocity models.

6.1 Test case

This project was developed based on a set of test data. As outlined in section 5.3, the first objective of the project was to recreate the original images, using the original 1D background velocity model. This objective was set in place to derive a baseline for evaluating the accuracy of the new method. Figure 6.1 is a side by side comparison of the test data using the original method; left, and the new method; right. The image was generated using the information obtained from a single event. This was therefore a natural first step, as the development and calculation times were short, and conclusive results could be obtained quickly. The simplicity of the data set also made for easier debugging.

The image, using proper scaling, displays a significant decrease in amplitude across the diagonal from the lower left part of the image. Modifying the amplitude scale was therefore a necessary step to evaluate the accuracy of the entire model. The scaling of the figures are set to facilitate a comparison of shapes and positions, as these are the key elements to evaluate how well the original results are reproduced by the new method. The placements and shapes of all features in the two images are virtually identical, except for some discrepancies near the transitions between positive (blue) and negative (red) perturbations. As the transitions from red to blue are the areas of smallest amplitude, minor discrepancies near edges are not of great concern. The demonstration of the validity of the tools and techniques developed

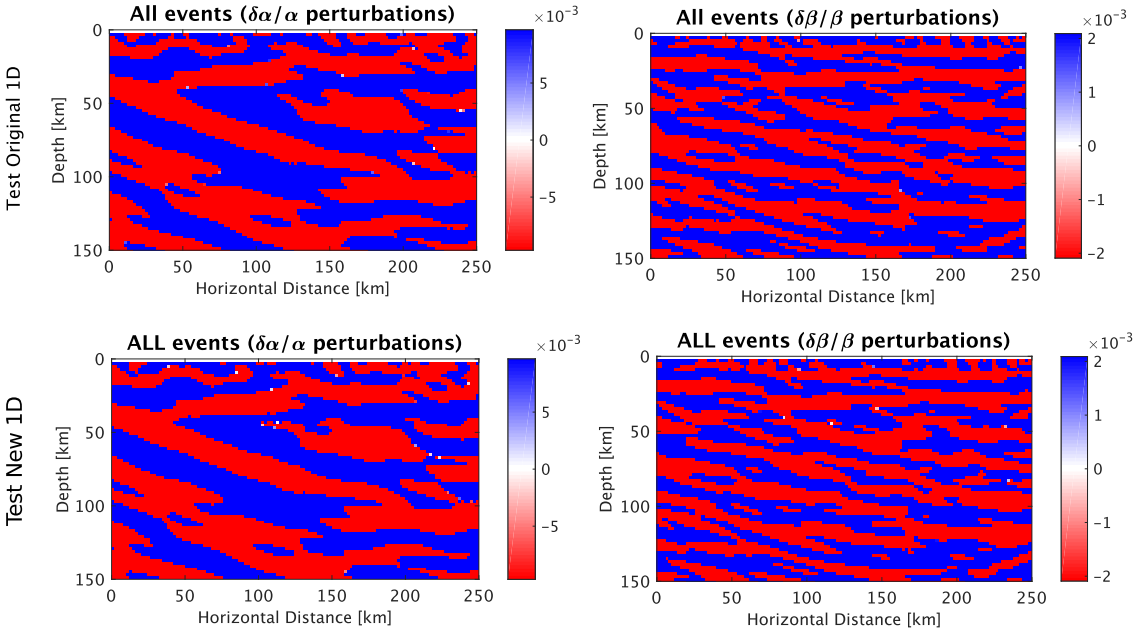

Figure 6.1: Models generated by test-data. Left: original method. Right: new method.

as part of the project can thus be considered a success, and the rest of this chapter will be focused on the results of the concrete application of the new method.

6.2 Overview

Our results may be divided according to the overview detailed in figure 6.2. The two main categories are results from the application to synthetic data, and the application to real data from the Cascadia subduction zone. In the case of the synthetic data we have two datasets; one with a fast and one with a slow mantle wedge. The dataset used for the Cascadia subduction zone is the dataset CASC93, obtained by Nabelek et al. (1993), previously described in section 4.3, hereafter referred to as the real dataset, and subsequent real results.

In the case of the synthetic datasets we apply the velocity model best fitting to each of the datasets. We apply the new method with a fast mantle wedge, in the case of the fast mantle wedge and vice versa. In the case of the real data we may divide the results in two main categories, one with a homogeneous crust and one with a multilayered crust, as prefaced in section 5.4.2, application to the real Cascadia dataset. For each of these categories we will apply new method using the three different different 2D velocity models, labelled fast, slow and moderate, in reference to the fast, slow and moderate seismic velocities of the mantle wedge, relatively.

The velocity models will be implemented in this sequence, in the order of least to most interesting. The original and new method is applied to all cases using the best fitting 1D velocity model.

The synthetic results will be presented first. The images of the synthetic case will be presented with an overlay of the outline of the velocity model used for generating the synthetic dataset, as a frame of reference. The outline will provide the correct placement of features and is a good measure of the absolute accuracy of the method. The fast case will be presented first as it portrays the least change from the 1D velocity model.

The real results with a homogeneous crust will be presented next, with no overlay, but the features will be named in correlation with previous studies, in particular the study by Bostock et al. (2002). This leaves case of the real data with a multi layered crust for last.

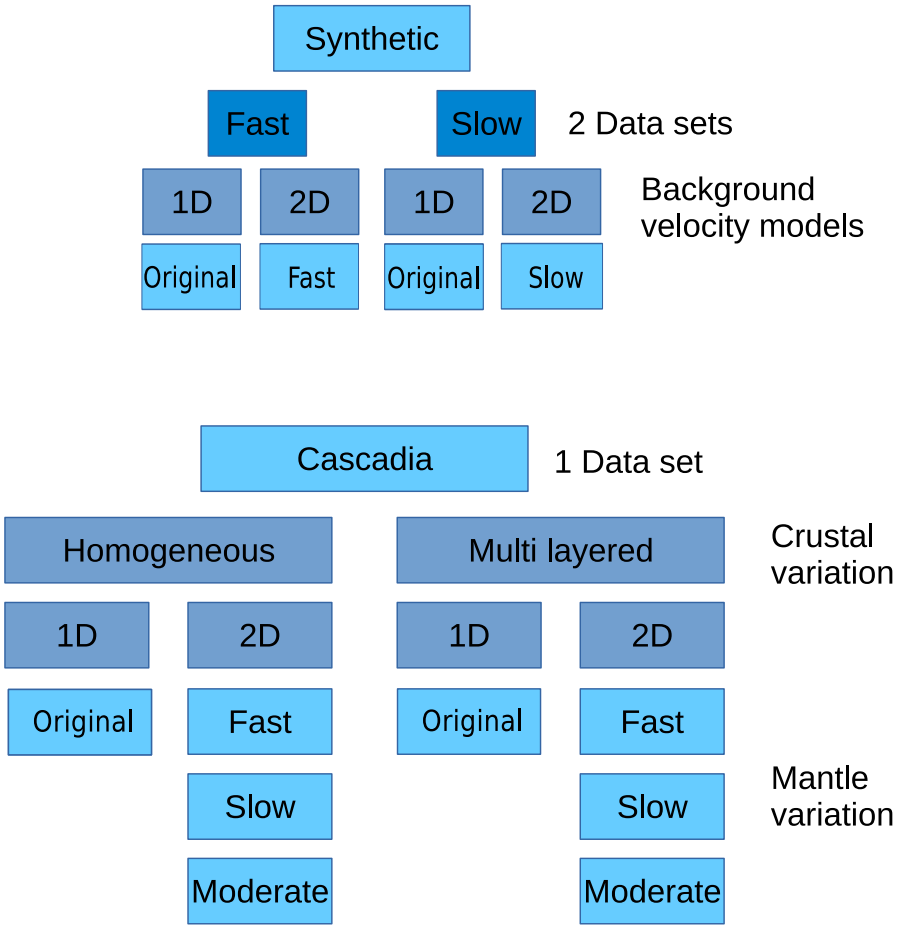

Figure 6.2: Overview of results

This leaves a total of 16 subcategories to investigate, 12 applications of the new method (8 with a 2D geometry and 4 with a 1D geometry), compared to 4 applica-

tions of the original method with a 1D geometry,(see figure 6.2). For each of these subcategories, seven images are generated by the methods:

- One image displaying both the alpha-perturbations and beta-perturbations, based on all of the events
- One image displaying both the alpha-perturbations and beta-perturbations based on just the reverberations of all of the events
- Five images displaying the results from the individual scattering modes: PP, PS, direct S, SSv and SSh.

Of these, only the first image will be presented and discussed in this thesis, since these images are compilations of all the different perturbations, giving the best overview.

The results for all these subcategories will be presented in two stages:

1. The models generated by the original method will be compared to the new method, using the same 1D background velocity model. This will demonstrate the validity of the new method, as applied to the specific dataset.
2. The models generated using the new method and a 1D velocity model will then be compared to the models generated using the new method and the 2D velocity models. This insures that any minute changes between the models, generated by the changes between the original and the new method, do not contribute to the comparison across different velocity models and evaluation of success.

When evaluating the images, I will look for the same trends as observed in the original image, and (in the synthetic cases) in relation to the overlay image. In all image presentations, the left image, displaying the alpha-perturbations, will be denoted as image A, and the right image, displaying the beta-perturbations, will be denoted as image B. The main focus will be on the dipping slab, the continental Moho discontinuity, and the mantle wedge, as these are the areas most relevant to my research questions. All images, including mode contributions, will be included in appendix; A.1.

6.3 Synthetic data - Fast mantle wedge

6.3.1 Validity - Comparison between original and new method (1D background velocity model)

The first step is to demonstrate that the new method models the subsurface correctly, as compared to the original method. As evident by figure 6.3, all the major features are correctly located and have the right dimensions. There are no discernible differences between the two images, neither in terms of alpha- or beta-perturbations.

6.3.2 Features - 1D background velocity model

There are two main features in these images. There is the diagonal red structure dipping with 7 degrees from 25 km depth on the left. In image A, we can see the feature ending abruptly at an offset of 120 km at a depth of 50 km, with an increased thickness and an obvious underlying blue structure. The structure is at all times adhering to the lines of the overlay, extending ever so slightly in the direction of subduction. In image B, the structure appears to be spanning across the entire model, with a substantial decrease in thickness in the right half of the image, and an overall more convex shape. The structure is adhering to the lower boundary of the outline in the left section of the image and the second lowest line in the right section of the image.

The other prominent feature is the horizontal red-to-blue structure at 30 km depth, spanning from about 60 km offset, where it meets the upper boundary of the diagonal structure, near the right end of the image. This feature is more prominent in the image A, but has a softer transition than in image B. This might be a result of the difference in perturbation % scale between the two images.

6.3.3 Features - 2D background velocity model

The change between the images generated using a 1D velocity model and a 2D velocity model, with no serpentinization, is minute at best. The same main features that were identified in the 1D case are observed in the 2D case. Both features are positioned in the same locations and with the same extensions. A slight increase in the dip of the dipping feature could be argued, as it appears to follow the lower boundary a little closer in the 2D case, slightly extending beyond the boundary near 50 km depth. In image A, the right end of the dipping feature appears to have a more diffuse edge and a more horizontal cut-off. The blue section underlying the dipping feature appears more consistent in thickness, and follows a more convex

shape, in contrast to the slight lense shape in the 1D image. The reverberations beneath the dipping feature also appear more planar in the 2D case, in contrast to the almost concave expression in the 1D case. All features above the dipping section, including the horizontal red-to-blue transition, appear identical in the 1D and 2D case.

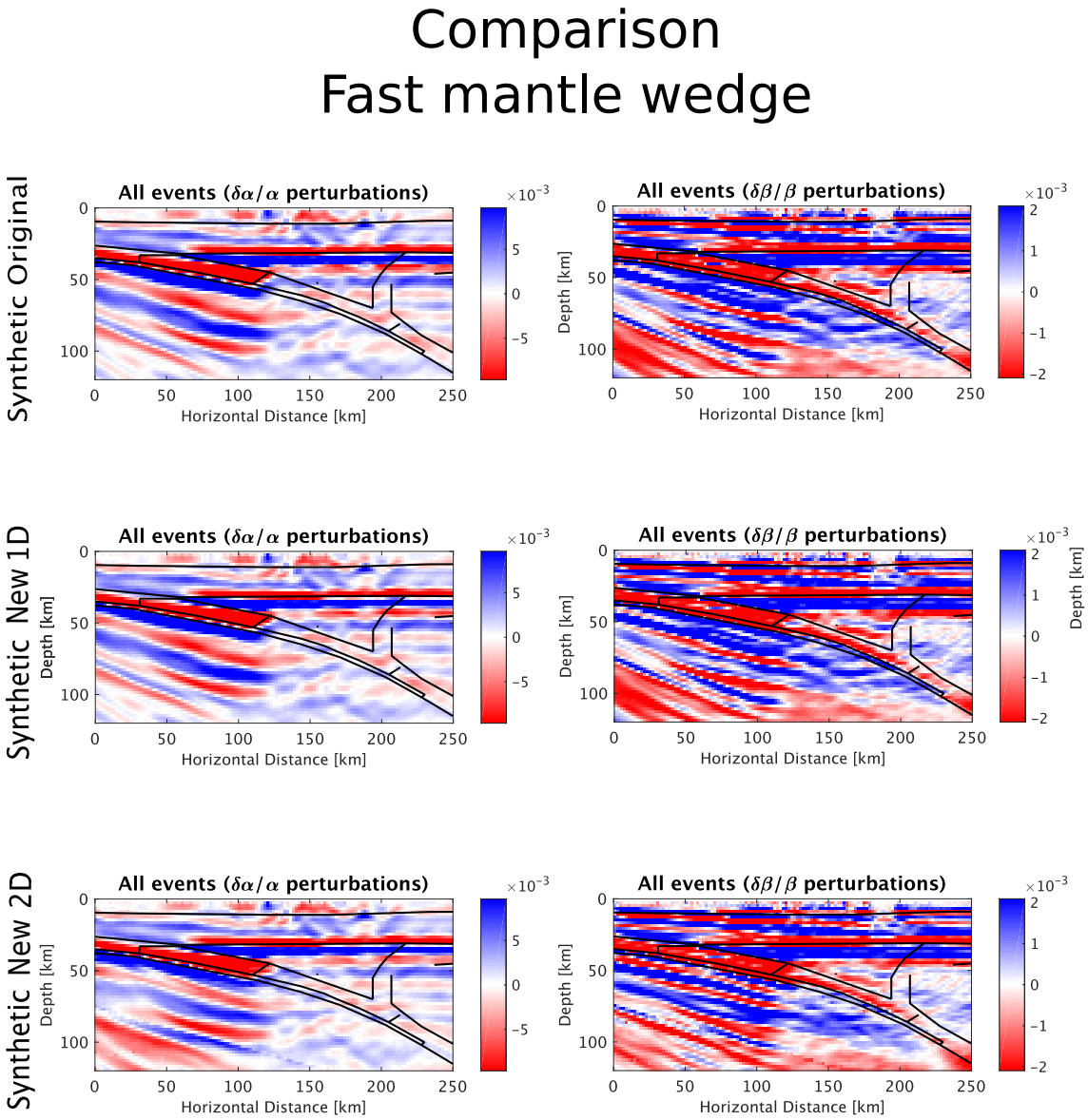

Figure 6.3: Images generated using synthetic data. In this figure from top down is the images generated using the Original method, New method 1D, New method 2D with a fast mantle wedge, respectively.

6.4 Synthetic data - Slow mantle wedge

6.4.1 Validity - Comparison between original and new method (1D background velocity model)

The images generated using synthetic data that included a slow mantle wedge is displayed in figure 6.4. The images generated by both the original method, top, and new method, middle, are identical everywhere in terms of the shape and positioning of the features.

6.4.2 Features - 1D background velocity model

In the left part of the images, we still see the dipping structure as we did in the case with the fast mantle wedge. It appears to have a slightly steeper dip, and, in image A, an abrupt transition at 55 km depth and 110 km offset. This takes the form of a jump; 5 km vertically upward and 10 km eastward, to a continuation of the red structure that disperses out to a thicker structure, eventually splitting before ending at 200 km offset. The dipping feature extends beyond the boundaries set by the overlay in both images. A red elongated feature, observed in image A, at 60-80 km depth and 120-160 km offset, located beneath the lower boundary, could be identified as a continuation of the original dipping feature. The horizontal feature observed in the previous synthetic case is only identified in the rightmost end of the images, beyond 220 km offset, to the right of the 'vertical' line indicating the end of the wedge. Above the section indicated to be the mantle wedge by the overlay, there is no clear discontinuity in image A. In image B, a horizontal structure is identified, but with a blue-to-red transition, rather than the previously identified red-to-blue transition.

6.4.3 Features - 2D background velocity model

In the 2D case, the dipping feature follows the lower line of the overlay perfectly. The feature is thinner than in the 1D case and the jump observed in the 1D case is now a more gentle transition towards a planar feature. The section of the dipping feature, that previously protruded below the outline, has been shifted upwards and is exactly above the outline in the 2D case. The same shift occurred to the elongated feature that was believed to be a continuation of the dipping feature. This feature is now confined to a narrow segment along the dipping structure, as dictated by the overlay. The lower section of the red structure, that in the 1D case appeared as a continuation of the dipping feature into the area associated with the forearc mantle, is shifted upwards as well, and is now constrained by the boundaries set

by the overlay. The upper section of the same feature is still located at the same position as in the 1D case, but with perhaps a more horizontal transition towards the surface, resulting in an ultimately more constrained red feature. In image B, the two segments of the dipping feature that protruded below the lower boundary of the outline are shifted upwards, in the same fashion as in the image A. A red, elongated, narrow structure is observed along the lower boundary, in the same location as in image A. All in all we observe a diagonal shift upwards and to the right that has affected the entire lower left diagonal of the image, in both images. The upper 40 km of the image, including the horizontal feature, remain identical in both the 1D and 2D case.

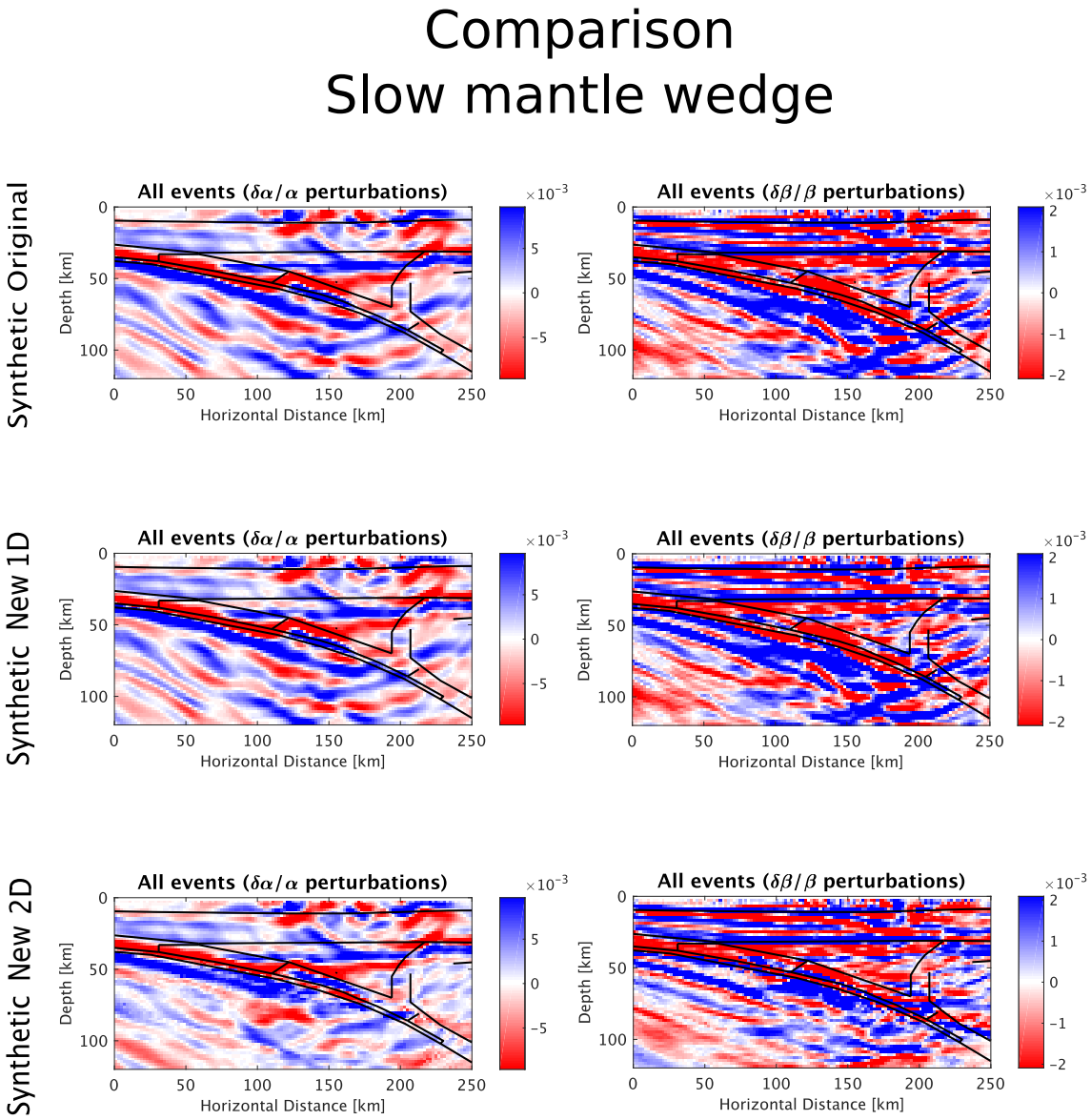

Figure 6.4: Images generated using synthetic data with a no mantle wedge. In this figure from top down is the images generated using the Original method, New method 1D, New method 2D with a slow mantle wedge, respectively.

6.5 Cascadia data - Homogeneous crust

In this section, and in section 6.6, the images generated using the Cascadia dataset will be presented. As this dataset is well studied, there is a general consensus on the identification of the features displayed in the images (Rondenay et al., 2001), (Rondenay et al., 2008), (Bostock et al., 2002), (Tréhu et al., 1994). For simplicity and readability, I will, therefore, utilize the names of the interpreted features, as proposed by these authors. The main source of inspiration will be the images generated by Bostock et al. (2002), observed in this thesis in figure 5.6. The features will be defined in subsections 6.5.2 and 6.6.2.

6.5.1 Validity - Comparison between original and new method (1D background velocity model)

In figure 6.5, we see the models generated by the original method and the new method using the simplest 1D velocity model with the homogeneous crust. The models are close to identical; the shapes and positions are similar. There appear to be some artefacts in centre of image A from the original method, at 40 km depth and 140-180 km offset, that does not appear in the model generated by the new method. The intensity of some of the features in image B, particularly around 70 km depth and 110 km offset, are not perfectly resolved, but as the general shapes and positions are correct I evaluate both images as successful, in terms of the replicability.

6.5.2 Features - 1D background velocity model

In the 1D model, we observe the dipping feature, located at 25 km depth, dipping at $\sim$10 degrees landward, towards the right, corresponding to the basaltic crust of the oceanic plate, Juan the Fuca. We see a thickening of the feature at 40 km depth and a dissipation shortly after. It dissipates in two stages, where the lower half of the subducting slab dissipates at 85 km offset while the upper half dissipates at 110 km offset, both at 55 km depth. In image A there is a large red feature in the lower right section of the model, that appears to be a continuation of the dipping feature, starting at an offset of 150 km and depth of 70 km, identified as eclogitized oceanic crust. A similar, less constrained, less homogeneous feature is observed in the same location in image B. The horizontal feature, identified in the synthetic dataset, is easily identified in image B, with a reversal of polarity at 130 km offset. It appears as a distinct, horizontal feature, and we observe the inversion of colours, as well as a thickening as it connects to the dipping feature. This feature corresponds, in placement and expression, to the continental Moho. It is difficult to observe in image A.

6.5.3 Features - 2D with a fast mantle wedge

In the images generated using a 2D velocity model with a fast, unserpentinized mantle wedge and a homogeneous crust, we observe a large section of the image shifted slightly diagonally upwards. Similar to the one observed in the synthetic case with a slow mantle wedge. We do observe some artefacts, in the form of some odd coloured pixels occurring along two diagonal parallel lines, spanning across the model, coinciding with the crust-asthenosphere and asthenosphere-mantle boundaries of the background velocity model. The upwards diagonal shift observed, affects the dipping oceanic crust, causing it to appear as a more linear feature, with a consistent dip of 7-8 degrees. The eclogitized crust, at the lower right section of the images, have also been shifted upwards and are now weakly connected to the upper, basaltic crust. It has, however, not shifted so far as to align with the underside of the basaltic crust. The eclogitized crust might appear more constrained and with a more consistent dip. The features above the oceanic crust, but beneath the continental Moho appear more horizontal, but have not been subjected to any major changes worth mentioning. The Moho, itself, at 40 km depth, is about identical to that of the 1D case, as is the medium above 40 km.

6.5.4 Features - 2D with a slow mantle wedge

The images generated using a 2D velocity model with a slow mantle wedge, representing a high amount of serpentinization, and a homogeneous crust, portrays many of the same changes as observed in the case of the fast mantle wedge. The same trends of off-coloured pixels are unfortunately observed, and a bright blue upper right corner might be observed at 150 km offset and 40 km depth. This coincides with the position of the mantle wedge in the background velocity model.

The basaltic crust observed in the 1D case is shifted diagonally upwards, appearing as a more continuous feature than in the 2D fast mantle wedge case, and is shifted slightly farther. The upper boundary of the dipping crust remains in the same location in all previous cases. An additional upwards shift thus serves to further constrain the extension of the crust, now appearing with a consistent thickness along the structure. The step or jump observed in the synthetic case is also observed here, in the upper, dipping, basaltic crust. The lower dipping, eclogitized crust, that is believed to be a continuation, is shifted slightly upwards as well. It appears more constrained, and is more clearly resolved, than in the slow 2D case. It appears to be

aligned with the post jump section of the upper dipping structure. The link between the upper and lower structure, observed in the 2D fast case is now broken, although the positioning of the features still indicate that the lower dipping structure is a continuation.

A red, upward extension of the lower dipping, eclogitized crust is observed in image A, in the area of the mantle wedge, at 140 km offset and 55 km depth. This was not observed in the case of the fast mantle wedge. This feature is also not clearly identifiable in the image B. Above the lower end of the upper dipping structure there appears to be a small, red, banana shaped structure, nearly separated from the dipping basaltic crust itself. This feature is only observed in image A, as image B instead displays a solid red transition from the dipping feature into the horizontal feature. In the 1D case, this feature was not possible to separate from the dipping crust. While the feature is more discernible in the 2D fast case, it is still not as clearly resolved or of the same size as in this 2D slow case. The crustal section of the model is identical to the 1D and 2D fast case, and there are no noteworthy changes to the continental Moho, compared to the fast case.

6.5.5 Features - 2D with a moderate mantle wedge

The images generated using a 2D velocity model with a more moderate degree of serpentinization of the mantle wedge, still with a homogeneous crust, is displayed in the bottom row of figure 6.5. The features observed in these images are in general fairly similar to the case of the slow mantle wedge. Some discrepancies, assumed to be due to the difference in background velocity, are still observed. Slight variations from the slow case is observed in the two dipping structures, corresponding to the basaltic and eclogitized crust, mostly due to a less extensive uplift of the lower left diagonal, compared to the slow case. The basaltic crust appears more linear, as the jump is dampened, while the thickness is still continuous. The banana shaped feature above the lower part of the upper dipping basaltic crust, is shifted vertically downwards, and overlaps with the basaltic crust. The lower dipping eclogitized crust is almost identical to the slow case, but appears, perhaps due to the shift of the upper crust, as a more natural continuation to the upper basaltic crust. The strange upwards protruding red structure is still present but at a slightly smaller scale. There are no apparent changes to the continental Moho or the upper 40 km.

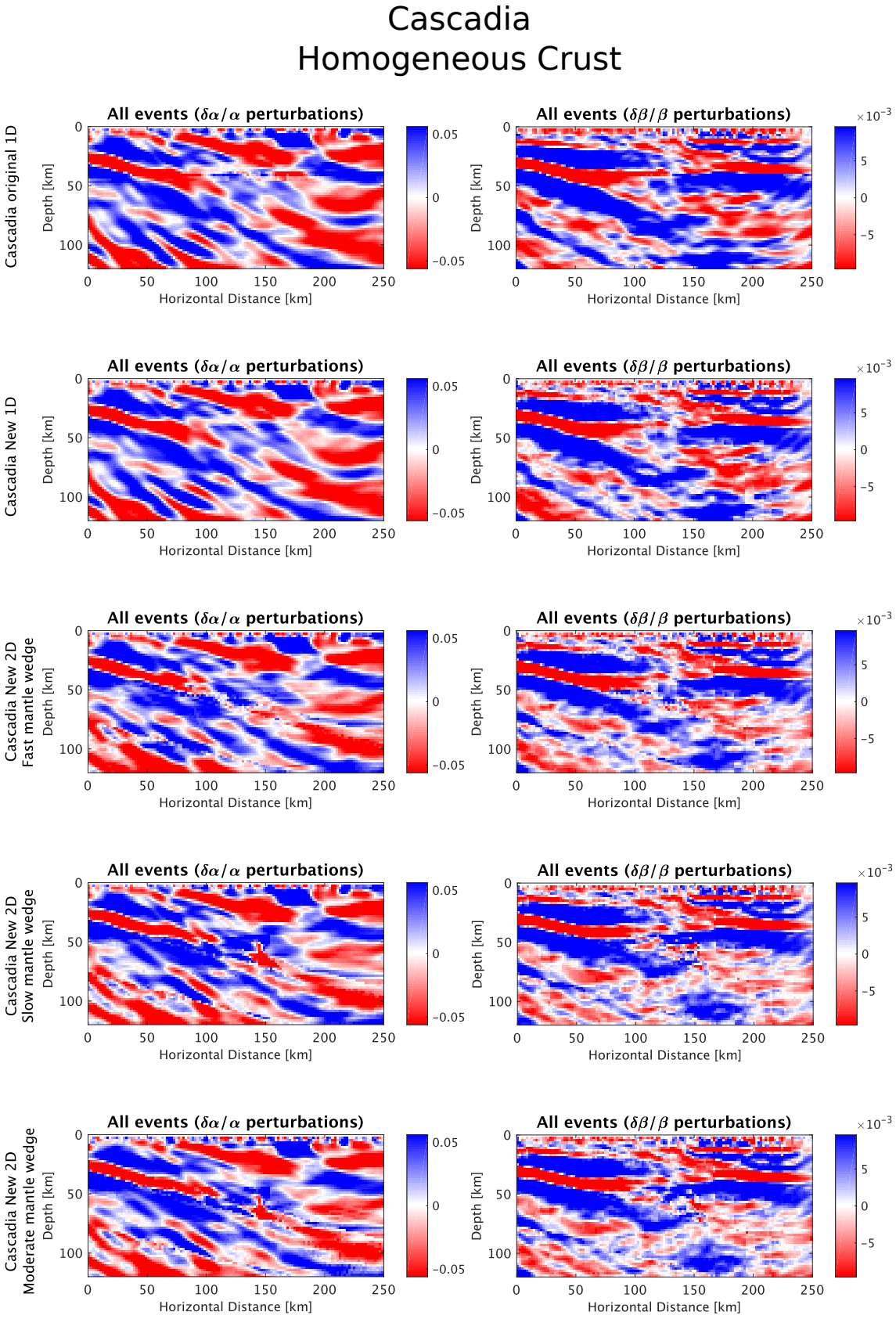

Figure 6.5: Images generated using the Cascadia data set and a homogeneous crust. In this figure from top down is the images generated using the Original method, New method 1D, New method 2D: fast mantle wedge, New method 2D: slow mantle wedge, New method 2D: moderate mantle wedge, respectively.

6.6 Cascadia data - Multi layered crust

6.6.1 Validity - Comparison between original and new method (1D background velocity model)

The images generated for the Cascadia dataset, using the custom 1D velocity model, containing a multilayered crust is displayed in figure 6.6. The figure displays the images generated using the original method and the new method on the first and second rows, respectively. The images display a similar location, size and shape of features, comparable to the previously discussed cases.

6.6.2 Features - 1D background velocity model

In the 1D model,second row, we observe the same features as in the case of the simple crust, but in image A we see a slight downward shift of the features below 40 km, and upward shift of the features above 40 km. In image B we observe a more general upwards shift of the features. In image A, this extension increases the apparent dip of the upper dipping crust. The oceanic crust now dips from a depth of 25 km and ∼17 degrees landward dip with an even thickness of about 10 km. The feature thickens at 40 km depth and 75 km offset (the same location as the simple case), but appears more constrained than in the simple case. In image B, the upper dipping basaltic crust is imaged with smoother boundaries, and the thickening of the crust appears as a natural progression. The continuation of the dipping structure, the eclogitized crust, reappears after a small gap at a depth of ∼65 km and offset of 140 km, and continues until the end of the model in image A. It is poorly constrained and with a varying dip and thickness. In image B, the upper dipping basaltic crust appears to transition into the horizontal feature. The continental Moho is again only identifiable in image B, and even here it contains a lot of noise between the offset of 110 km and 160 km, similar to the observations in the case of the homogeneous crust.

6.6.3 Features - 2D with a fast mantle wedge

In the images generated by the new method applied using a 2D velocity model with a fast mantle wedge and layered continental crust,third row, we observe a significant amount of artefacts, in the form of odd coloured pixels, similar to those observed in the cases of with homogeneous crust. We observe a diagonal upward shift of the features, similar to the effect observed in the previous 2D cases, both in the synthetic and Cascadia models. This reduces the apparent dip of the upper dipping basaltic crust, from a landward dip of ∼17 degrees to ∼14 degrees. The thickening

of the basaltic crust is reduced, as the lower boundary is shifted upwards while the upper boundary remains largely stationary. The eclogitized crust is also shifted in the same fashion. The lower boundary is shifted upwards, while the upper boundary remains stationary. This effect is apparent, but poorly resolved, due to the artefacts previously mentioned. The lower dipping eclogitized crust still appear to be more constrained, with a lower, more consistent dip, and a more narrow shape. The features in the mantle above the dipping oceanic crust appears more planar, as the trend of the upwards shift forms a bulge. The continental Moho, at 40 km, is poorly resolved in image A, but appear as a clear red-to-blue discontinuity from 150 km and landward. This discontinuity is less defined in the area prior to 150 km offset. The upper 40 km appears identical to the 1D case.

6.6.4 Features - 2D with a slow mantle wedge

The fourth row of figure 6.6, displays the images generated with the new method using a 2D velocity model with a slow mantle wedge. Some off coloured pixels occur along the same lines as in previous images, the protrusion of the upper right corner of the mantle wedge being especially worrying. Similar to the observations made in the case of the slow, homogeneous case, we observe an increased uplift in the center of the image, 100-150 km offset, compared to the fast 2D case. We observe a clear division into an upper dipping basaltic crust and lower dipping eclogitized crust. The upper dipping basaltic crust appears as a homogeneous structure with a consistent thickness. As the lower end of the basaltic crust is uplifted, the general dip of the structure is altered. We observe a slight jump, or offset, similar to the one identified in the 2D slow synthetic case and slow homogeneous Cascadia case. The red banana shaped feature observed above the lower end of the upper dipping basaltic crust, previously identified in the slow case of the homogeneous crust, is not strictly apparent. An argument for a division of the lower end of the eclogitized crust could be made, as a thickening is observed with a weaker segment crossing through. This is not observed in the case of the 2D fast, multi-layered case.

Correctly identifying any minute changes to the lower dipping structure is difficult, due to the noise observed. A general upwards shift and concentration of red features around an offset of 100 to 150 km, is, however, clearly observed. The shape of the structure in the mantle above the lower dipping structure is shifted upwards compared to the 1D case, in a similar manner as in the 2D fast case, but the shape of the feature in the 2D slow case is more remanent of that of the 1D case. The horizontal feature at 40 km depth is unaltered, as are all features above 40 km.

6.6.5 Features - 2D with a moderate mantle wedge

The bottom row of the figure are the images generated using the new method, a more moderate assumption of serpentinization of the mantle wedge and a multi layered crust. The model is for all intents and purposes close to identical to that of the slow mantle wedge and multi layered crust. Some slight changes between the two models can be observed. These include a less extensive uplift of the structures in the center of the image, offset 100-150 km and depth of 40-70 km, more so in image B than in image A. In image B, the oceanic crust is less connected, and appears as two more distinct features. All features in the upper 40 km, the horizontal discontinuity, the Moho, at 40 km depth and the features in the mantle above the lower dipping oceanic crust is identical to the case of the slow mantle wedge.

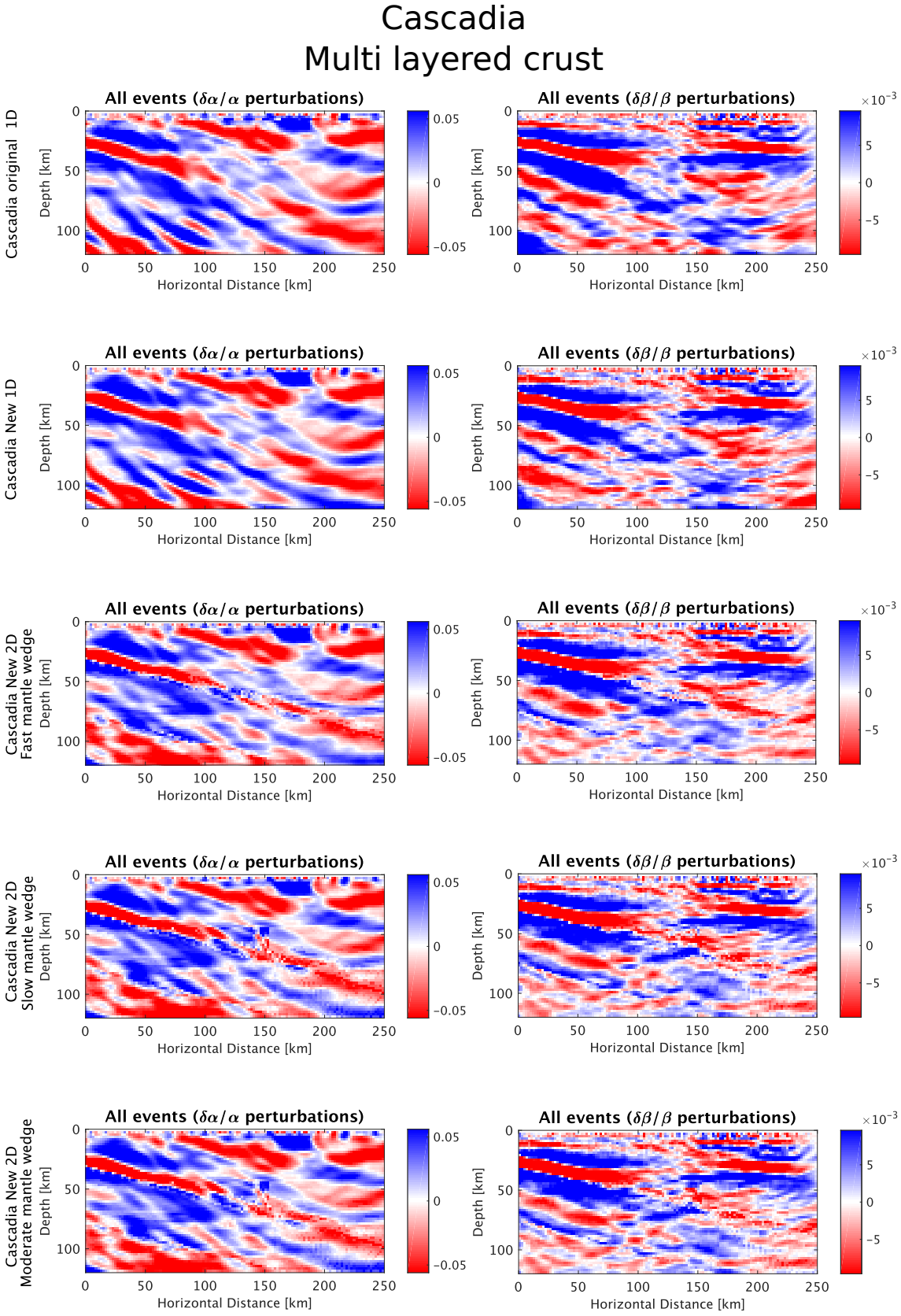

Figure 6.6: Images generated using the Cascadia data set and a multi layered crust. In this figure from top down is the images generated using the Original method, New method 1D, New method 2D: fast mantle wedge, New method 2D: slow mantle wedge, New method 2D: moderate mantle wedge, respectively.

Chapter 7

Discussion

In this chapter I will discuss the main outcomes of the project. First, I will evaluate whether or not the changes made to the method may be considered an improvement, particularly in respect to the defined research questions. Then I will discuss some of the constraints, challenges and solutions put in place to obtain these images as well as a note on the computational demand. Finally, I will present some conclusions and some suggestions for further work.

7.1 Discussion of results

7.1.1 Interpretation of results

Synthetic case

In the synthetic case of the fast mantle wedge, we observe two distinct features. We observe a structure dipping inland from a depth of 25 km with a dip of $\sim$7 degrees across the left half of the model and a horizontal feature at 30 km depth and at an offset of about 60 km where it intersects with the dipping feature and to the end of the model. These coincide with the features outlined in the velocity model used to generate the synthetic data. The 2D background velocity model in this case introduces a dipping feature representing a dipping oceanic crust. The images produced are close to identical for both the original, new 1D and new 2D case.

In the synthetic case of the slow mantle wedge, we observe the same general features as in the fast mantle case. We also observe a continuation of the red feature, beyond the extension observed in the fast case. This feature disperses into a triangle shape with two branches. As this feature is only observable in the synthetic case of the slow mantle wedge this is believed to be indicative of slower seismic velocities in the mantle wedge. The 2D background velocity model includes lower seismic velocities

in the forearc mantle and we observe a significant improvement in the placement of the features observed. The region above 40 km depth is unaffected. This is a trend that is observed in all cases, as the velocity model associated with the scatterers in this region is identical in the new and old method. In the case of a fast mantle wedge, this trend extends down to the first dipping interface.

Cascadia case

In the models generated from the Cascadia dataset, we observe the same three features. We observe a dipping feature, in the same location, that is interpreted, based on previous studies Langston (1981),Tréhu et al. (1994) and Rondenay et al. (2001), as the dipping oceanic lithosphere of the Juan de Fuca plate. We observe a horizontal feature, also in the same location, that is, based on the same studies, interpreted as the continental crust-mantle-discontinuity, also known as the Moho. The feature is best observed in the images displaying the beta perturbations, indicating a sharper, more abrupt transition in S-velocities, than in P-velocities. This might, however, be due to a difference in scaling between the two images. We observe a thickening of the subducting oceanic slab towards a depth of 50 km. This thickening may be indicative of the presence of a slower mantle wedge, as the thickening might be an effect similar to the effect observed in the synthetic case.

Slight differences may be observed in the models generated based on the homogeneous crust and the multilayered crust. The biggest difference is a vertical shift of features. The image displaying the alpha perturbations underwent a vertical extension, resulting in a uplift of features in the top section and a downshift of features below 30-40 km. The image displaying the beta perturbations experienced, on the other hand, a general uplift. This is natural as the P-velocities were increased in the mantle and decrease only in the top two layers, while the S-velocities experience a consistent decrease. The features appear more constrained in the case of a multilayered crust and adhere to sharper transitions.

When we apply the new method to a more complex background velocity models we observe a trend of an upwards shift of the lower left diagonal section of the image. The shift varies depending on the velocity model incorporated. In the case of the fast mantle wedge the shift may be described as an upward shift increasing with depth and offset. With the introduction of a slow mantle wedge at the center of the image, the area beneath the mantle wedge is even further lifted up, as the area above experiences a decrease in velocities. This results in a total uplift with a concave shape and bulging center. The uplift results in a decrease in the dip of

the subducting oceanic crust and a better constrained lower dipping structure. The continental Moho appears largely unchanged by the introduction of a 2D velocity model. This is not surprising as the crust (upper 40 km) does not change by design. The spatial extent and the seismic parameters of the mantle wedge introduced are highly uncertain as the landward end of the wedge is assumed to be a smooth transition (Bostock et al., 2002). The petrological conditions, more specifically the degree of hydration (which has a significant influence on seismic velocities), is under continuous discussion.

The images generated using a 2D velocity model with a more moderate degree of serpentinization of the mantle wedge and a multilayered crust, were deemed to be the most accurate as they were generated using the presumed most realistic estimate of the reference background velocity model. The images of this case will be compared to the interpretations made by Rondenay et al. in 2001 and 2008 of the original model(Rondenay et al., 2001)(Rondenay et al., 2008). Based on these evaluations I will answer the research questions put forward in the introduction.

7.1.2 Implication

In this project I set out to determine if a 2D background velocity model would provide a significant improvement of the migration technique; the inverse GRT. The improvement would be evaluated in terms of the accuracy of the images produced, both in terms of the reliability of the results observed and the accuracy of the structures identified. As some artefacts are produced for 2D cases when real data is used, the reliability of the new images produced is slightly diminished, at least for the specific cases and positions where errors are known to occur. The accuracy is, however, undoubtedly improved. Altering the background velocity model has had a noticeable effect on the produced images. As the alterations made to the background velocity are a clear improvement in accuracy, the implication is that any alterations to the produced images results in an improvement in the accuracy of the produced images. We may thus assume that any general changes to the generated images observed for a 2D case, is an improvement compared to the 1D case. The reliability depends on the region of interest, and as the region of interest put forward in the research questions were related to the areas of disturbance, the focus of interpretation will be large, general trends, with little confidence placed on minor features.

The general shift of features is in agreement with expected changes, and as such deemed an improvement on the images produced. We expect a general shift of features as we introduce areas of higher and lower velocities to the reference model. This will alter the travel times, and the signals observed are attributed to a more correct position. As the reference medium is similar for nearby points, the shift of data is similar as well. The minor structures near, and in, the mantle wedge are circumstantial due to the possibility of artefacts, and will not be discussed in terms of improvement.

In order to evaluate if the general shift has had an effect on the interpretation of the images, we look at the interpretations made by Rondenay et al. (2008), as these are the latest and most accurate interpretations to date. The evaluation was conducted by retracing the interpretations made in 2008 and setting the resulting outline as an overlay over the images produced by the new method. The position of the overlay was checked against the images produced by the new method using a 1D model. In figure 6.6, bottom row, we observe the images generated using a moderate mantle wedge and a multi layered crust, with a scaling set to approximate the scaling of the figures created in 2008. A set with (left), and without (right), the interpretations made, is displayed. The solid lines represent the interpretations made by Rondenay in 2008 and the dashed lines indicate two alternate interpretations, based on the new images. Interpretation (a) indicates a continuous dipping oceanic crust with no kink present. Interpretation (b) indicates a kink, but with a lesser change of dip and later occurrence. With interpretation (b) the oceanic plate would not change direction until reaching a depth of 55 km. With interpretation (a) the oceanic plate would continue with no change of direction. Both interpretations alter the current temperature-pressure conditions placed upon the plate at depths $>$ 45km. The kink at 45 km depth has previously been interpreted to be the onset of eclogitization (Bostock et al., 2002). As we still observe a transition to weaker perturbations in terms of S-velocities in the same location as in the images of 2002 and 2008, we may still interpret the onset of eclogitization at 45 km depth.

A further discussion on the consequence of the new temperature and pressure conditions will not be conducted, as a petrological interpretation of the new images is not within the scope of this thesis. The focus will rather be on the relative accuracy of the interpretations made in 2008, and in this thesis.

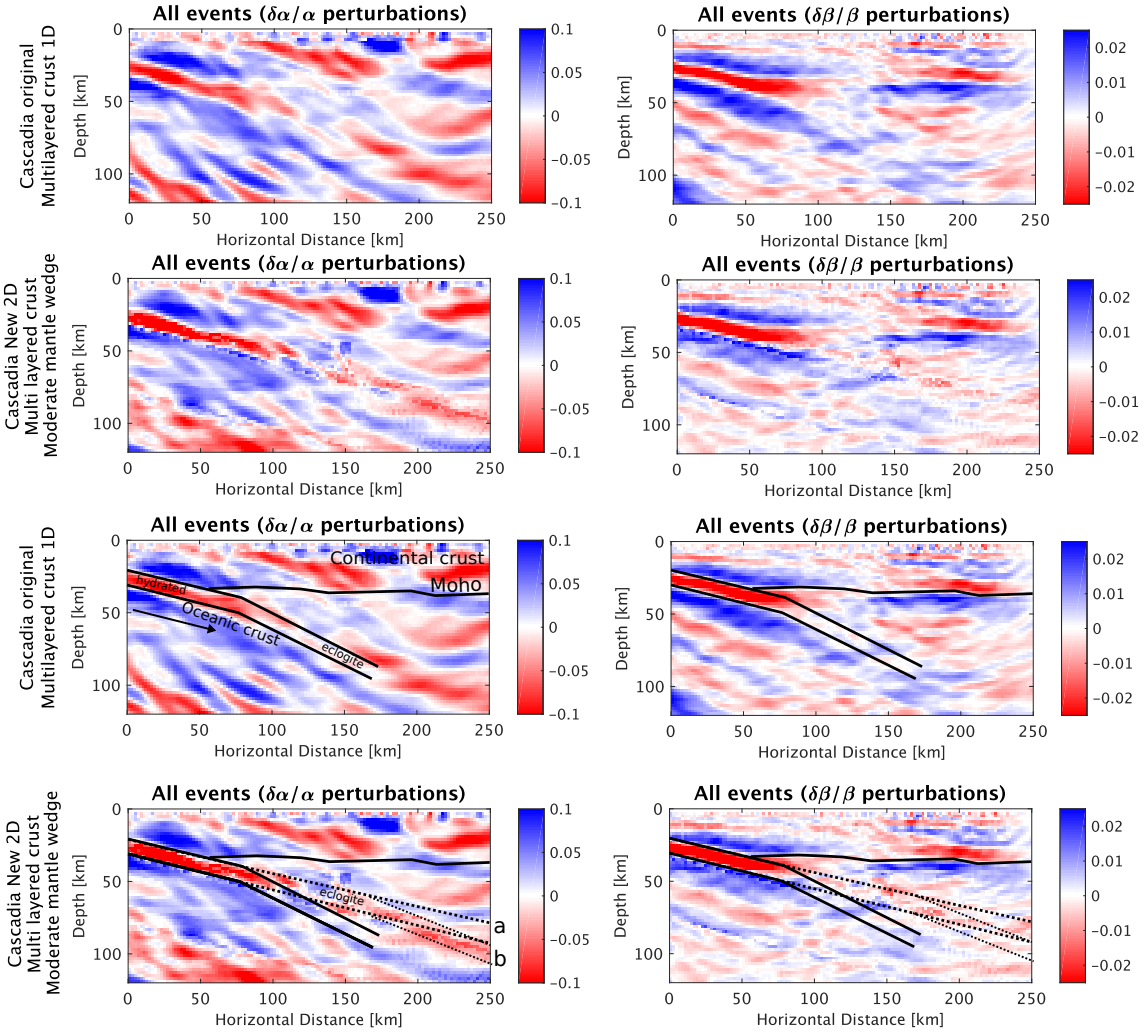

Figure 7.1: Interpretation made by Rondenay in 2008 overlaid on images generated by the new method with a 1D multilayered crust, and new method with a 2D multilayered crust and moderate mantle wedge. New alternate interpretations, **a** and **b**, included.

7.1.3 Research questions

In terms of our research questions, a general consensus could be that the implementation of a 2D background velocity model does indeed provide a significant improvement in accuracy. This implementation positions the structures below the continental crust more accurately, and results in a correction of the dipping oceanic crust. This correction is perhaps big enough to disprove the kink proposed by Rondenay et al. (2001). The previous identification of the kink was likely produced by the simplifying assumptions made in 2001, specifically the assumption of a 1D reference model when imaging 2D perturbations. The mantle wedge is, however, not more discernible through the new method. The mantle wedge is located just beneath the crust and it is identified through an alteration of the signature of the Moho. As the Moho was already included in the original reference model, no major

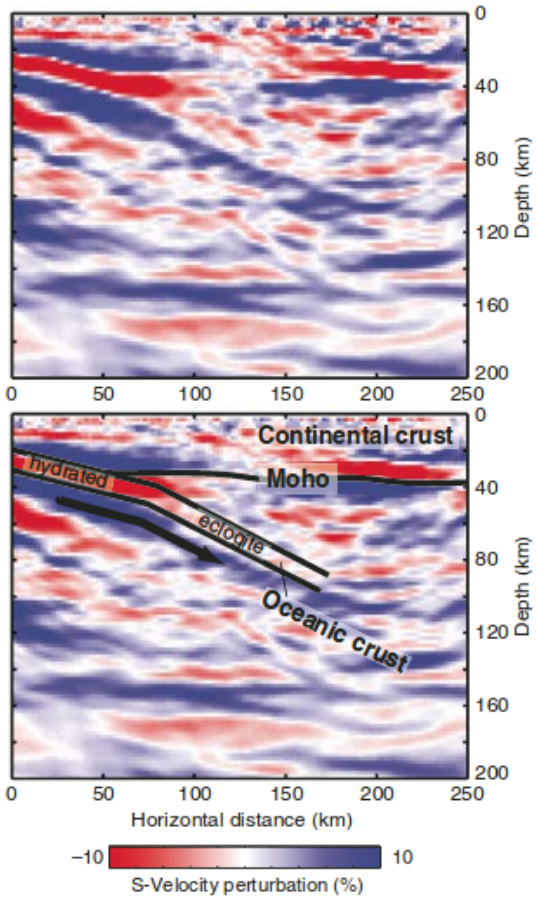

Figure 7.2: Interpretations by Rondenay et al. (2008)

changes were put in place, apart from the alteration of the properties of the mantle wedge. This alteration had a greater effect on the underlying structure than the crust-mantle discontinuity. The mantle wedge is therefore currently not better constrained by utilizing a 2D reference model.

The processing time has been mentioned on occasion throughout this thesis. The improvements to the images generated is significant enough that the computational demand of the method is less of a concern. It may still be noted that the processing time from preprocessed data to finished images was ∼1000 seconds with the original method, while with the new method, it is ∼6000 seconds for the synthetic 2D case, ∼7500 seconds for the Cascadia 2D case with a homogeneous crust and ∼11500 seconds for the Cascadia 2D case with a multilayered crust. All cases were run on the servers made available through the department. This server had a total of 516822 MB RAM divided over 64 CPUs. The new method has unfortunately not been designed for parallel loops. These processing times are significant, but still reasonable. It is therefore concluded that improvement of image-quality justifies the increase in computational demand.

7.2 Problems and challenges

The main source of problems and challenges were related to the introduction of dipping interfaces, low velocity layers and challenging scatterer-station-combinations.

The spatial positions of the scatterers and stations are such that not all combinations are possible with a natural, upwards travelling ray path. The restriction of an upwards travelling ray path is due to the transformation from a ray path in a 2D velocity model to one in 1D. A ray path that propagates through the same depth segment on multiple occurrences is hard to translate, as the same depth segment might be associated with different properties. Downwards propagating rays, including critically refracted and reflected rays are therefore omitted from the process.

The spatial positions of the stations/receivers in relation to the scatterer meant that even when ray tracing outwards in a range of $[-\pi/2 : \pi/2]$, reaching the station was not a guarantee, especially for shallow scattering points. A natural step would be to include extrapolation, when determining the exact ray paths. Although the interfaces were linear, and as such easy to predict, the end of interfaces, or introduction of new interfaces, caused the extrapolation to produce sub-par, and on some occasions entirely wrong, ray paths. The most extreme ray path possible, the ray path generated with a take off angle of $\sim \pm\pi/2$, was determined to be a better approximation and was such used for all stations the ray path could not reach, given the constraints of the ray tracer. Using the most extreme ray paths omitted the need for extrapolation.

A recurring issue throughout the implementation was the occurrence of complex numbers. The complex numbers were encountered in the calculations of the scattered wave table. The interpolation table was created for a range of ray parameters to account for the incoming plane wave for each unique ray path. This occasionally led to scenarios where the ray parameter provided by the range, was less than the horizontal slowness. This resulted in an obliquity corrected velocity that, combined with the scattering angle, produced complex values through the expression $\sqrt{(1-p^2a^2)}$. This expression is a frequent part of the key calculations in inverse GRT. In this expression, p is the horizontal slowness denoting the scattering angle and a is the obliquity corrected P-velocity. Whenever $p^2a^2 > 1$, a complex value is generated. This was not a random occurrence, but arose when the scattering point was just/directly beneath a dipping interface. The sections where this expression is included is always a summation over layers. As complex values are only generated for either one or two layers, I circumvented the problem with complex numbers by

adjusting the horizontal slowness to a more moderate value. Using the expression $p^2 = 1/a^2 - 0.000001$ insured a value as close to the one provided as possible, while still within the acceptable range. The complex numbers were most likely caused by low velocity layers and dipping interfaces. This combination causes ray paths that, translated into 1D velocity models, have a high degree of variance in terms of layer thickness, see figure 7.3. Some layers are close to non-existent along one ray while being a dominating feature in another.

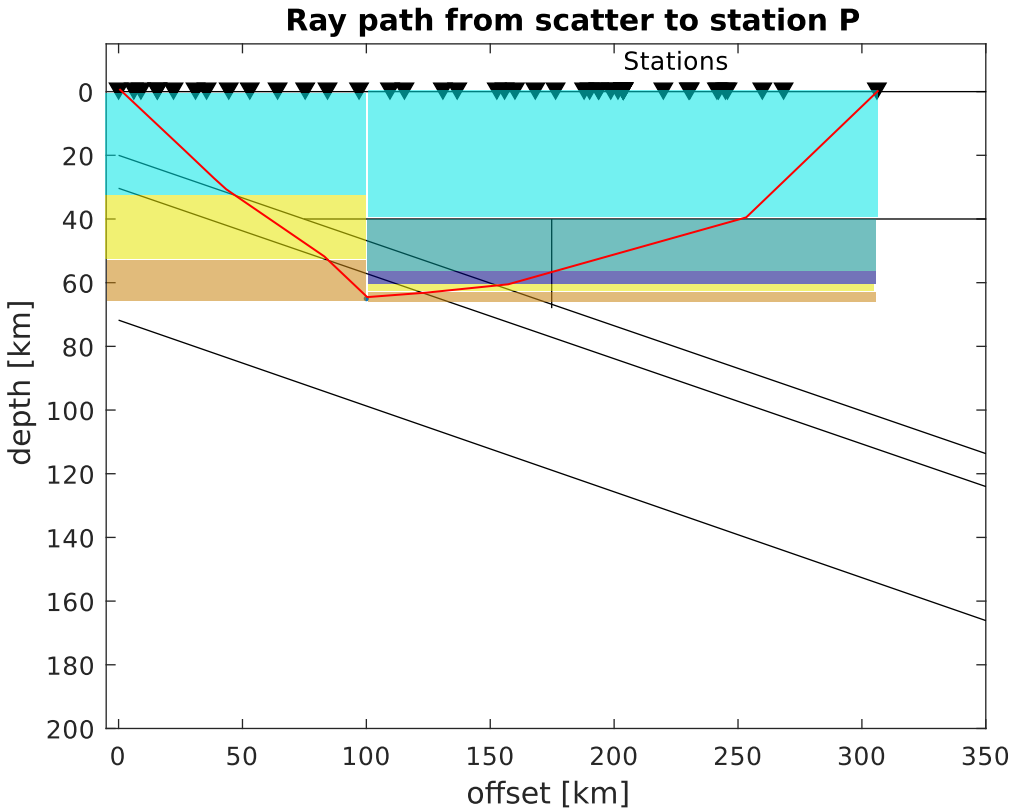

Figure 7.3: Illustration of ray paths, and resulting 1D velocity models, associated with scatterer directly beneath interface.

The near vertical nature of the landward end of the mantle wedge was also a challenge in the ray tracing. The ray originating from scatterers inside the mantle wedge was often reflected rather than transmitted, as illustrated by figure 7.4. The inclusion of these rays influenced the interpolation later in the process. Rays hitting this interface were therefore ignored in the later stages. This is most likely the cause of the protrusion of this upper corner in the Cascadia images.

As the discrepancies in the models, in the form of odd coloured data points, only occur for the Cascadia dataset, it is likely that the noise occurs due to out-of-plane events. The synthetic dataset was created with in-plane source and no obliquity

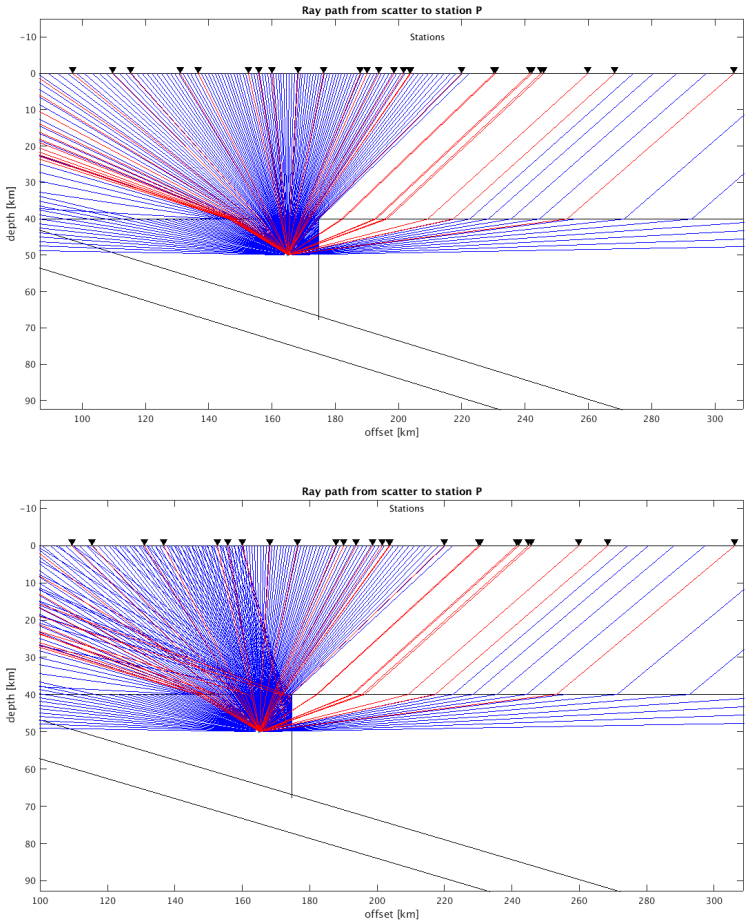

Figure 7.4: Illustration of ray paths originating within the mantle wedge. Top figure displays the final scenario. Bottom figure displays the scenario where no restrictions related to the mantle wedge are applied.

corrections were necessary. As the noise in the models only occur for the 2D case, the odd coloured data points are likely due to the combination of dipping interfaces and out-of-plane events, as the effect is present regardless of the seismic properties of the wedge.

7.3 Validity and limitations

The method images the medium using the forward and backscattered wavefield as it originates from perturbations in a 2D plane. The plane is chosen in the preprocessing, and all events and receivers are projected onto this plane. This limitation is lessened by a dense network of seismic receivers and multiple events, preferably inline with the 2D plane.

In this project I assume sharp transitions between media, as a constraint to improve

the computational time of the ray tracer. This is an obvious simplification of the real world. This is especially detrimental to the landward end of the mantle wedge, which is a smooth transition over a large horizontal area, and any sharp transition location would be dubious. This feature would more accurately be represented by a smooth transition. A sharp boundary was still determined for the sake of simplicity and consistency. Strictly linear interfaces were chosen for the same reasons. This simplification allowed for mathematical simplifications in the ray tracer that greatly improved the processing time and reduced the possibility of errors. The Earth is of course not planar, but as a reference model it still provided a significant improvement to the previously strictly horizontally layered reference model. The ray tracer also assumes the medium to be isotropic and homogeneous within the respective boundaries. This is a simplification of the elastic isotropic case, and necessary to lessen the mathematical and computational demand of the method.

The method as of now is developed for a 2D background velocity model, that may, with minor tweaks, be expanded to accommodate a 3D background velocity model, so as to even better approximate real cases. Even though the nature of a subduction zone has a great deal of variance perpendicular to the strike of the subduction zone, this does not negate that many subduction zones, for instance the Hellenic subduction zone, have a significant 3D variance as well, as the strike along the subduction zone is far from consistent and the subduction zone itself is curved.

In this project we started by assuming two possible cases of serpentinization. We assumed a fast mantle wedge with seismic properties equivalent to no serpentinization and a slow mantle wedge with seismic properties equivalent to extreme degrees of serpentinization, approximately 80% serpentinization, higher than ever assumed to occur in nature (Hyndman and Peacock, 2003). These two were chosen as two extreme edge cases in order to evaluate the contribution of each reference model. A more moderate case, with a serpentinization of 50%, determined from the graph created by Hyndman and Peacock (2003), was put forward to explore a more probable, realistic case and generate a model suitable for comparing to the interpretations of Rondenay et al. (2008). A uniform serpentinization of the entire forearc mantle is, of course, also a simplification.

Even with the limitations put in place to implement the 2D reference model, we still observe encouraging results. We observe a distinct shift of features offering a more accurate model that may be interpreted with simpler explanations. The trends observed with the new implementation are exciting enough that the application to other subduction zones would be of great interest.

7.4 Further work

The primary goal from here is to further develop the current tools to remove the artefacts observed. As part of this step it would be natural to remove some of the constraints set by the method and allow for a more complex 2D geometry. Implementing an option of smooth transitions would be a major step that might help to image the mantle wedge with higher accuracy and reliability, as adjusting the method to allow for a smooth mantle wedge edge would perhaps better discern the extent of the serpentinization. The option of a more complex 2D geometry would make the method more generally applicable, and would be a great step towards applying the new method to other subduction zones.

As an extension of a more complex 2D background velocity model, a 3D background velocity model could be considered. This could further relocate the features observed to even more accurate positions. It is, however, assumed that the step from a 1D to a 2D reference model has provided a larger improvement than the step from 2D to 3D reference model would. This is based on the belief that the assumption of a 1D case compared to a 2D case is a more extensive assumption than the assumption of a 2D case compared to a 3D case. This assumption is naturally entirely dependent on the complexity and symmetric nature of the subduction zone.

A different, but equally interesting step would be to observe if other techniques than ray tracing might generate similar or better results. Techniques such as the fast marching method (Popovici and Sethian, 1997) might provide a faster way of obtaining the same information, and might be easier to implement for a more complex 2D or 3D geometry. A petrological evaluation of the new results, both from this and potential future improvements to the method, in terms of the new temperature/pressure conditions following the uplift of features, would be an interesting study as well.

Chapter 8

Conclusion

In this project I have implemented a 2D background velocity model in the migration technique inverse Generalized Radon Transform. I have improved upon a limitation of the original method of Rondenay et al. (2001) by developing the tools and techniques needed, and demonstrated the importance of an accurate background velocity model through the application of the new method to both synthetic data and real data from the Cascadia subduction zone (Rondenay et al., 2001).

Throughout this thesis I have detailed the role of a subduction zone, its individual components and the importance of imaging subduction zones with a high level of detail. I have described some theoretical background on the topic of seismic propagation, the concept of inversion vs. forward modeling, and some migration techniques and the inverse GRT more in depth. I have presented a case study of the Cascadia subduction zone as it has been interpreted up until this point. I have described the process of implementation of the new method and detailed key steps, such as the development of a ray tracer and 2D model. I have presented and discussed the images generated by the application of the new method. I have discussed some limitations of the new method, as well as the challenges encountered in the development of this project. I will now reiterate some of the conclusions drawn from the application and evaluation of this new improved method.

The new method allows us to image the subduction zone with higher accuracy in terms of placement of the structures. Two interpretations were made based on the new image: The first being that the subducting slab may not have the kink discovered in previous studies, the second being that the kink is located deeper and with a shallower dip. Of these, the most basic interpretation offers a simpler viable description to the subducting system, and is as such an improvement from the previous interpretations.

It would be advantageous to further refine the method developed, as well as remove some of the constraints and expanding the scope of the method. It would also be of great interest to observe the results of this method applied to other subduction zones or geological settings in general. A petrological evaluation of the results of this project would be beneficial as some of the temperature and pressure conditions may have been altered as an effect of the upwards shift of features.

This project has been a great experience, as I have gained knowledge on migration techniques and the inner workings of subduction zones as well as an increased understanding of wave propagation. I feel content with the outcome of the project. I consider the improved accuracy of the images generated as a token of success. Although I would have liked to present images with no obvious artefacts present, I am satisfied in the conclusion that the Cascadia subduction zone has now been mapped in greater detail, and may no longer be considered kinky.

References

P. Audet, M. G. Bostock, D. C. Boyarko, M. R. Brudzinski, and R. M. Allen. Slab morphology in the cascadia fore arc and its relation to episodic tremor and slip. *Journal of Geophysical Research: Solid Earth*, 115(B4), 2010.

B. A. Auld. *Acoustic fields and waves in solids*. 1973.

G. Beylkin. The inversion problem and applications of the generalized radon transform. *Communications on pure and applied mathematics*, 37(5):579–599, 1984.

G. Beylkin and R. Burridge. Linearized inverse scattering problems in acoustics and elasticity. *Wave motion*, 12(1):15–52, 1990.

M. Bostock. The moho in subduction zones. *Tectonophysics*, 609:547–557, 2012.

M. Bostock and S. Rondenay. Migration of scattered teleseismic body waves. *Geophysical Journal International*, 137(3):732–746, 1999.

M. Bostock, S. Rondenay, and J. Shragge. Multiparameter two-dimensional inversion of scattered teleseismic body waves 1. theory for oblique incidence. *Journal of Geophysical Research: Solid Earth*, 106(B12):30771–30782, 2001.

M. Bostock, R. Hyndman, S. Rondenay, and S. Peacock. An inverted continental moho and serpentinization of the forearc mantle. *Nature*, 417(6888):536–538, 2002.

N. I. Christensen. Elasticity of ultrabasic rocks. *Journal of Geophysical Research*, 71(24):5921–5931, 1966.

S. W. Fleming and A. M. Tréhu. Crustal structure beneath the central oregon convergent margin from potential-field modeling: Evidence for a buried basement ridge in local contact with a seaward dipping backstop. *Journal of Geophysical Research: Solid Earth*, 104(B9):20431–20447, 1999.

E. R. Flueh, M. A. Fisher, J. Bialas, J. R. Childs, D. Klaeschen, N. Kukowski, T. Parsons, D. W. Scholl, U. ten Brink, A. M. Tréhu, et al. New seismic images

of the cascadia subduction zone from cruise so108—orwell. *Tectonophysics*, 293 (1):69–84, 1998.

C. Fowler. *The Solid Earth: An Introduction to Global Geophysics*. Cambridge University Press, 2005. ISBN 9780521584098. URL https://books.google.no/books?id=PifkAotvTroC.

J. Gazdag and P. Sguazzero. Migration of seismic data. *Proceedings of the IEEE*, 72(10):1302–1315, 1984.

R. Hyndman and K. Wang. Thermal constraints on the zone of major thrust earthquake failure: The cascadia subduction zone. *Journal of Geophysical Research: Solid Earth*, 98(B2):2039–2060, 1993.

R. D. Hyndman and S. M. Peacock. Serpentinization of the forearc mantle. *Earth and Planetary Science Letters*, 212(3):417–432, 2003.

D. Komatitsch and J.-P. Vilotte. The spectral element method: An efficient tool to simulate the seismic response of 2d and 3d geological structures. *Bulletin of the seismological society of America*, 88(2):368–392, 1998.

C. A. Langston. Evidence for the subducting lithosphere under southern vancouver island and western oregon from teleseismic p wave conversions. *Journal of Geophysical Research: Solid Earth*, 86(B5):3857–3866, 1981.

X.-q. Li. *Deconvolving orbital surface waves for the source duration of large earthquakes and modeling the receiver functions for the earth structure beneath a broadband seismometer array in the Cascadia subduction zone*. PhD thesis, 1996.

D. Miller, M. Oristaglio, and G. Beylkin. A new slant on seismic imaging: Migration and integral geometry. *Geophysics*, 52(7):943–964, 1987.

X. Nabelek et al. A high-resolution image of the cascadia subduction zone from teleseismic converted phases recorded by a broadband seismic array: Eos trans., 1993.

t. Pacific Network. Cascadia subduction zone, 2017. URL https://pnsn.org/outreach/earthquakesources/csz.

A. M. Popovici and J. Sethian. Three dimensional traveltime computation using the fast marching method. In *SEG Technical Program Expanded Abstracts 1997*, pages 1778–1781. Society of Exploration Geophysicists, 1997.

S. Rondenay. Upper mantle imaging with array recordings of converted and scattered teleseismic waves. *Surveys in geophysics*, 30(4-5):377–405, 2009.

S. Rondenay, M. Bostock, and J. Shragge. Multiparameter two-dimensional inversion of scattered teleseismic body waves 3. application to the cascadia 1993 data set. *Journal of Geophysical Research: Solid Earth*, 106(B12):30795–30807, 2001.

S. Rondenay, M. G. Bostock, and K. M. Fischer. Multichannel inversion of scattered teleseismic body waves: practical considerations and applicability. *Seismic Earth: array analysis of broadband seismograms*, pages 187–203, 2005.

S. Rondenay, G. A. Abers, and P. E. Van Keken. Seismic imaging of subduction zone metamorphism. *Geology*, 36(4):275–278, 2008.

J. Shragge, M. Bostock, and S. Rondenay. Multiparameter two-dimensional inversion of scattered teleseismic body waves 2. numerical examples. *Journal of Geophysical Research: Solid Earth*, 106(B12):30783–30793, 2001.

S. Stein and M. Wysession. *An introduction to seismology, earthquakes, and earth structure*. John Wiley & Sons, 2009.

A. Tréhu, I. Asudeh, T. Brocher, J. Luetgert, W. Mooney, J. Nabelek, Y. Nakamura, et al. Crustal architecture of the cascadia forearc. *SCIENCE-NEW YORK THEN WASHINGTON-*, pages 237–237, 1994.

N. Tsumura, H. Ikawa, T. Ikawa, and M. Shinohara. Delamination-wedge structure beneath the hidaka collision zone, central hokkaido, japan inferred from. *Geophysical Research Letters*, 26(8):1057–1060, 1999.

M. Unsworth and S. Rondenay. Mapping the distribution of fluids in the crust and lithospheric mantle utilizing geophysical methods. In *Metasomatism and the Chemical Transformation of Rock*, pages 535–598. Springer, 2013.

P. E. Wannamaker. Magnetotelluric observations across the juan de fuca subduction system in the emslab project. *Journal of Geophysical Research: Oceans*, 94(B10), 1989. ISSN 2169-9313.

P. E. Wannamaker, R. L. Evans, P. A. Bedrosian, M. J. Unsworth, V. Maris, and R. S. McGary. Segmentation of plate coupling, fate of subduction fluids, and modes of arc magmatism in cascadia, inferred from magnetotelluric resistivity. *Geochemistry, Geophysics, Geosystems*, 15(11):4230–4253, 2014.

C. S. Weaver and C. A. Michaelson. Seismicity and volcanism in the pacific northwest: evidence for the segmentation of the juan de fuca plate. *Geophysical Research Letters*, 12(4):215–218, 1985.

K. Wikimedia Commons. Diagram of the geological process of subduction, 2016. URL `https://en.wikipedia.org/wiki/Subduction`.

Appendix A

Appendix

A.1 All produced images

In this section all the images produced by the method, as applied to the synthetic and real Cascadia data set, is displayed. For each application 7 plots, containing 9 images in total, are produced, corresponding to the different mode contributions as described in section 6.2. These images are fitted to one page, resulting in one page for each case, 16 cases in total; 6 associated with the synthetic case and 10 associated with the Cascadia case.

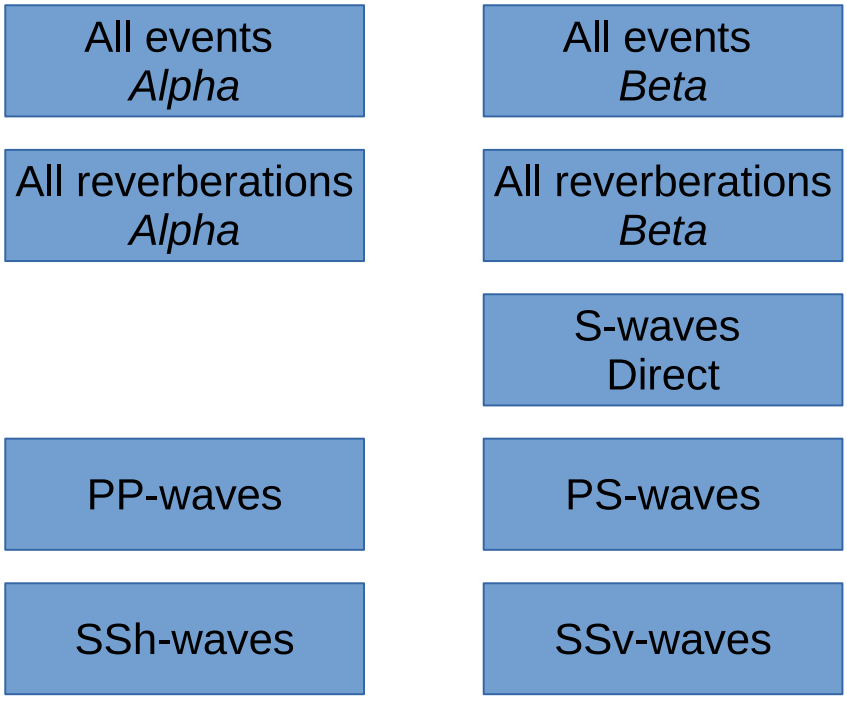

Figure A.1: Overview of compilation figures.

A.1.1 Synthetic data set

Synthetic data set - fast forearc mantle original method - 1D

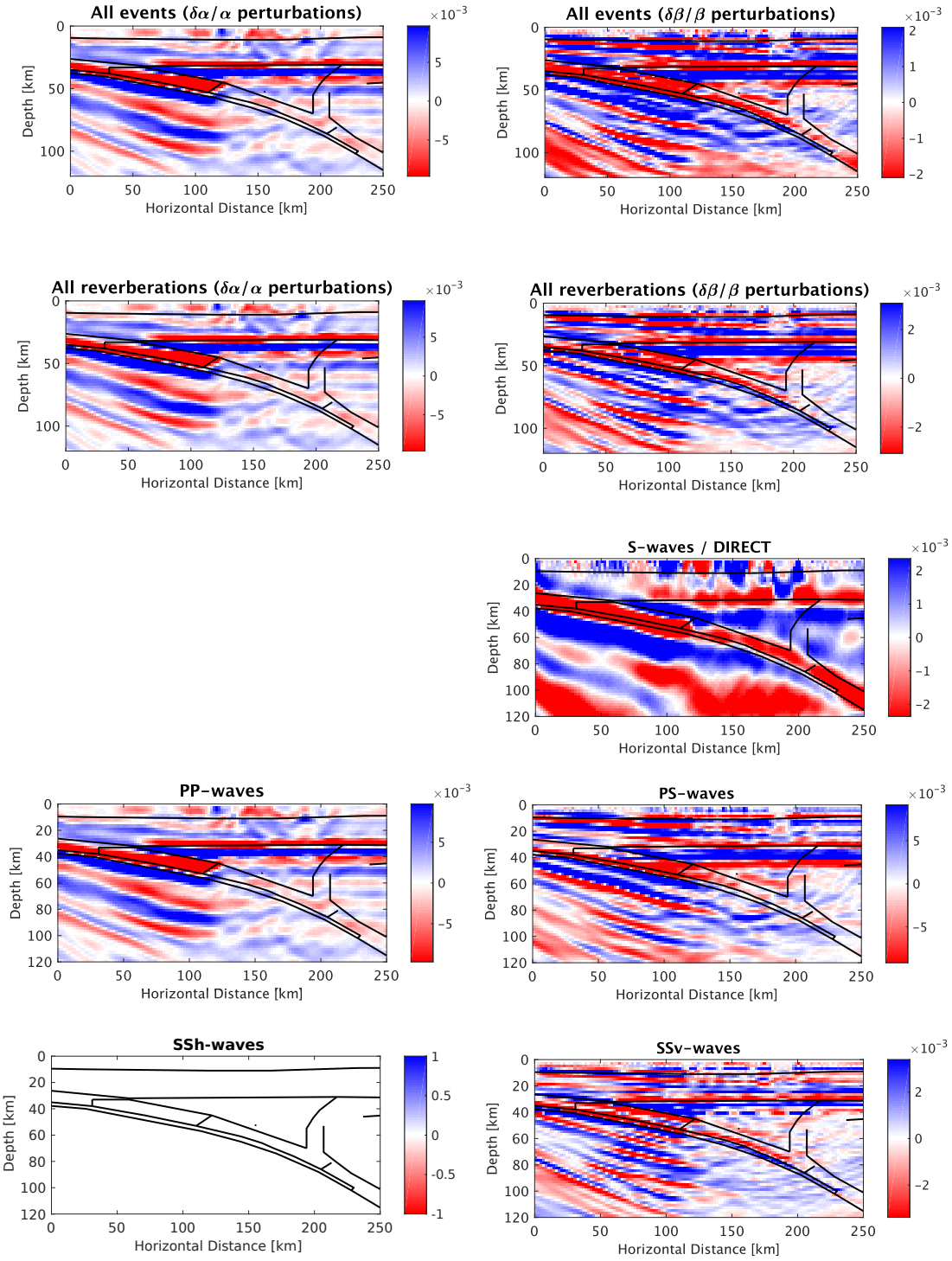

Figure A.2: Images generated using the Synthetic data set with a fast forearc mantle, original method 1D.

Synthetic data set - fast forearc mantle
new method - 1D

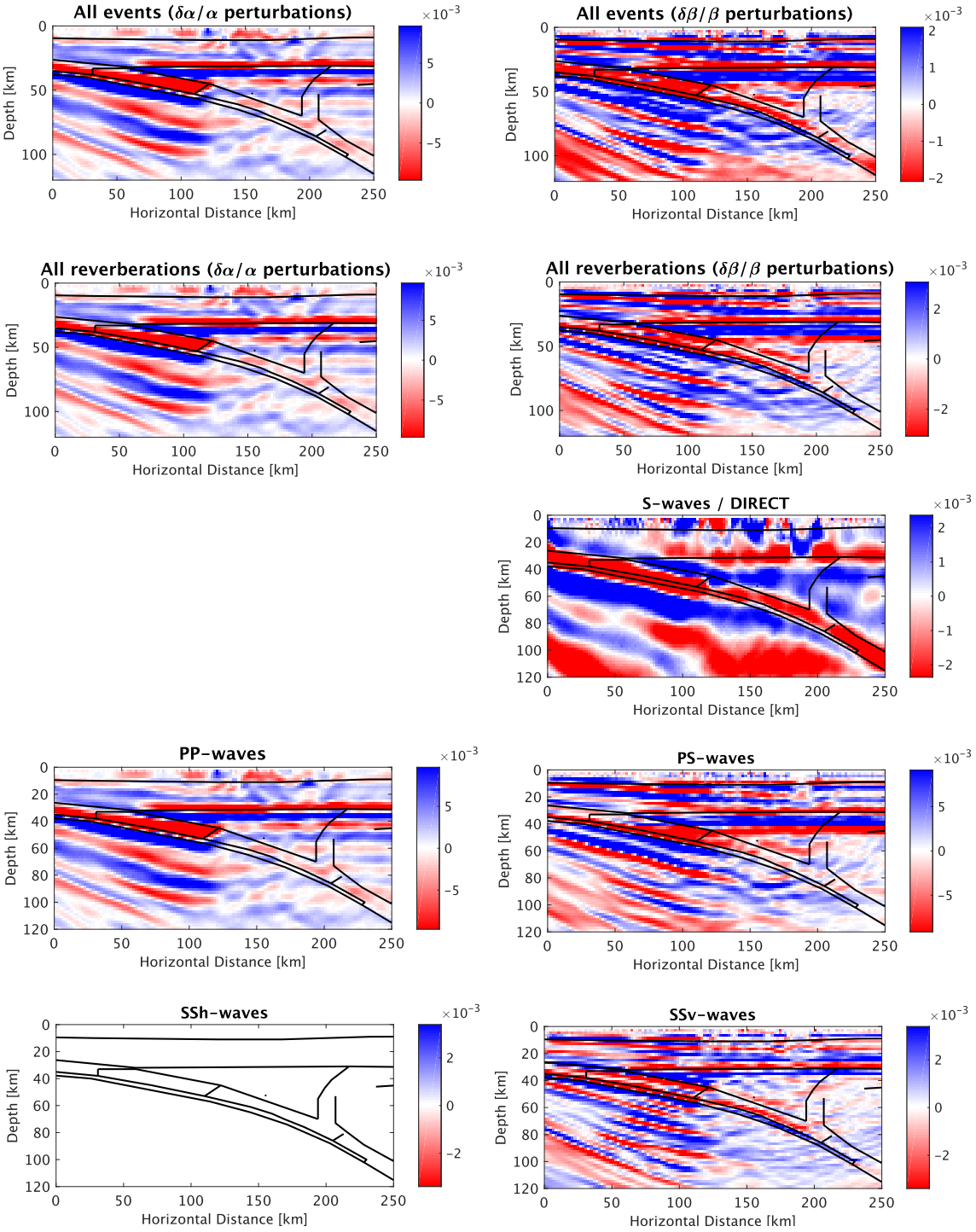

Figure A.3: Images generated using the Synthetic data set with a fast forearc mantle, new method 1D.

Synthetic data set - fast forearc mantle
new method - 2D

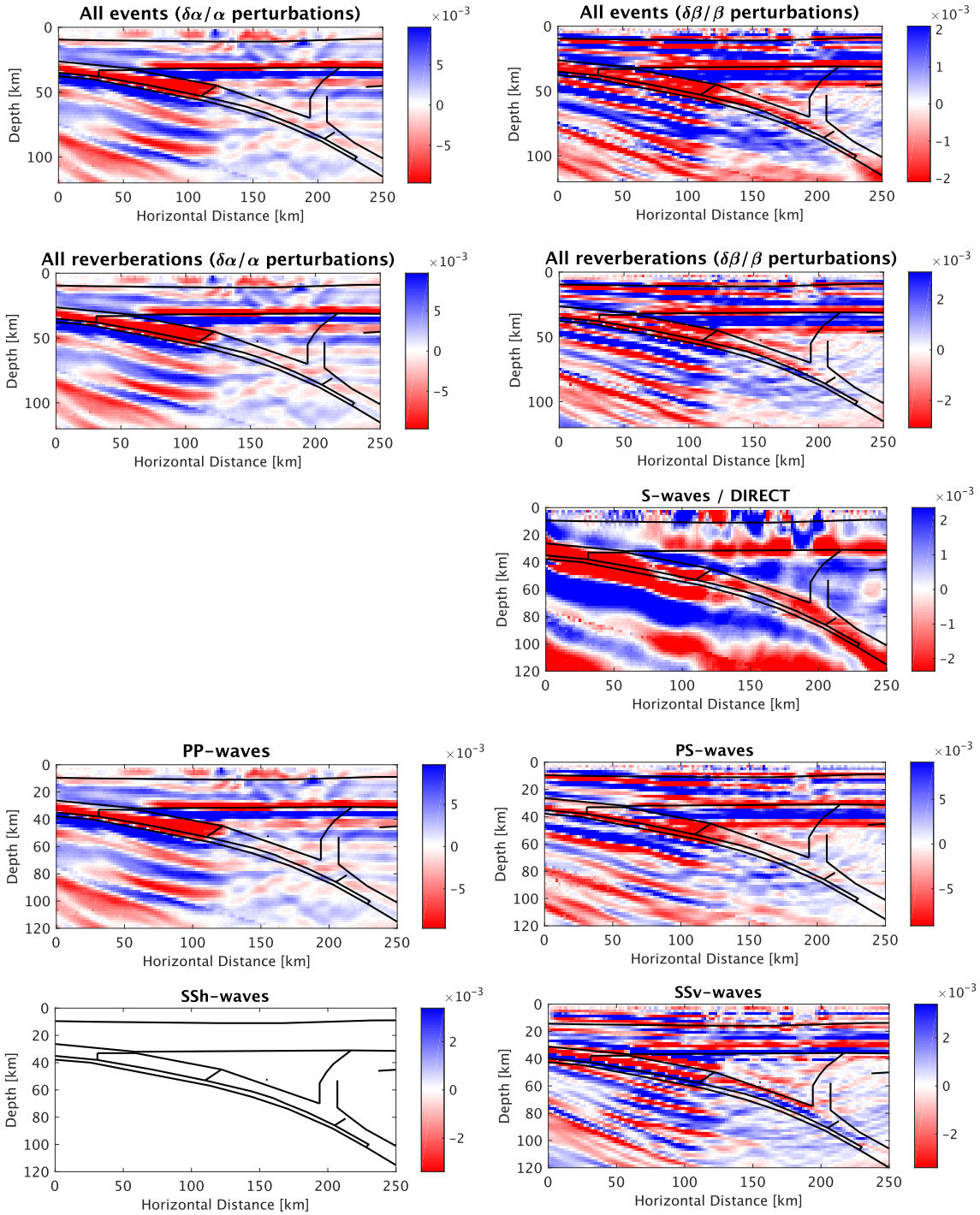

Figure A.4: Images generated using the Synthetic data set with a fast forearc mantle, new method 2D.

Synthetic data set - slow forearc mantle
original method - 1D

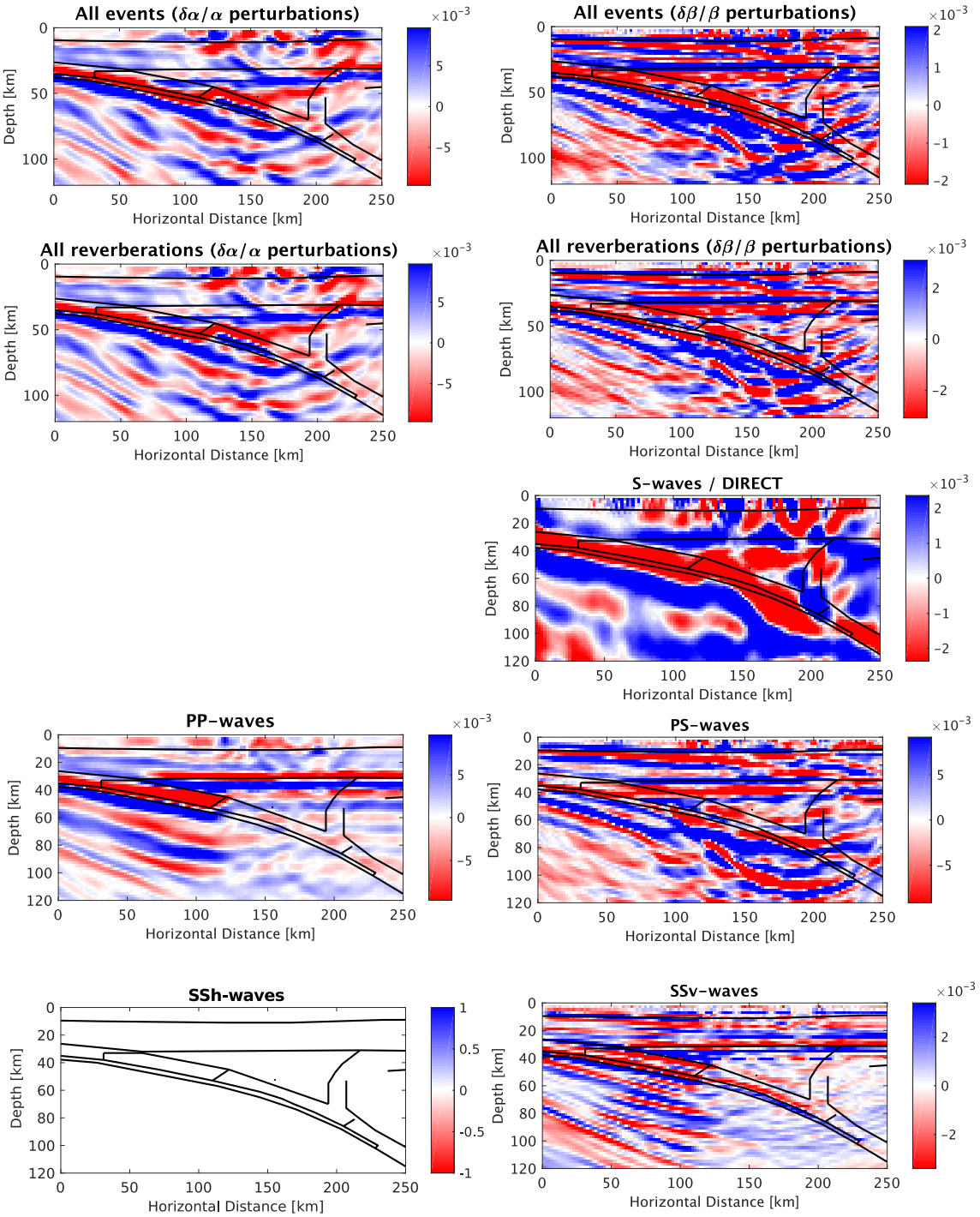

Figure A.5: Images generated using the Synthetic data set with a slow forearc mantle, original method 1D.

Synthetic data set - slow forearc mantle
new method - 1D

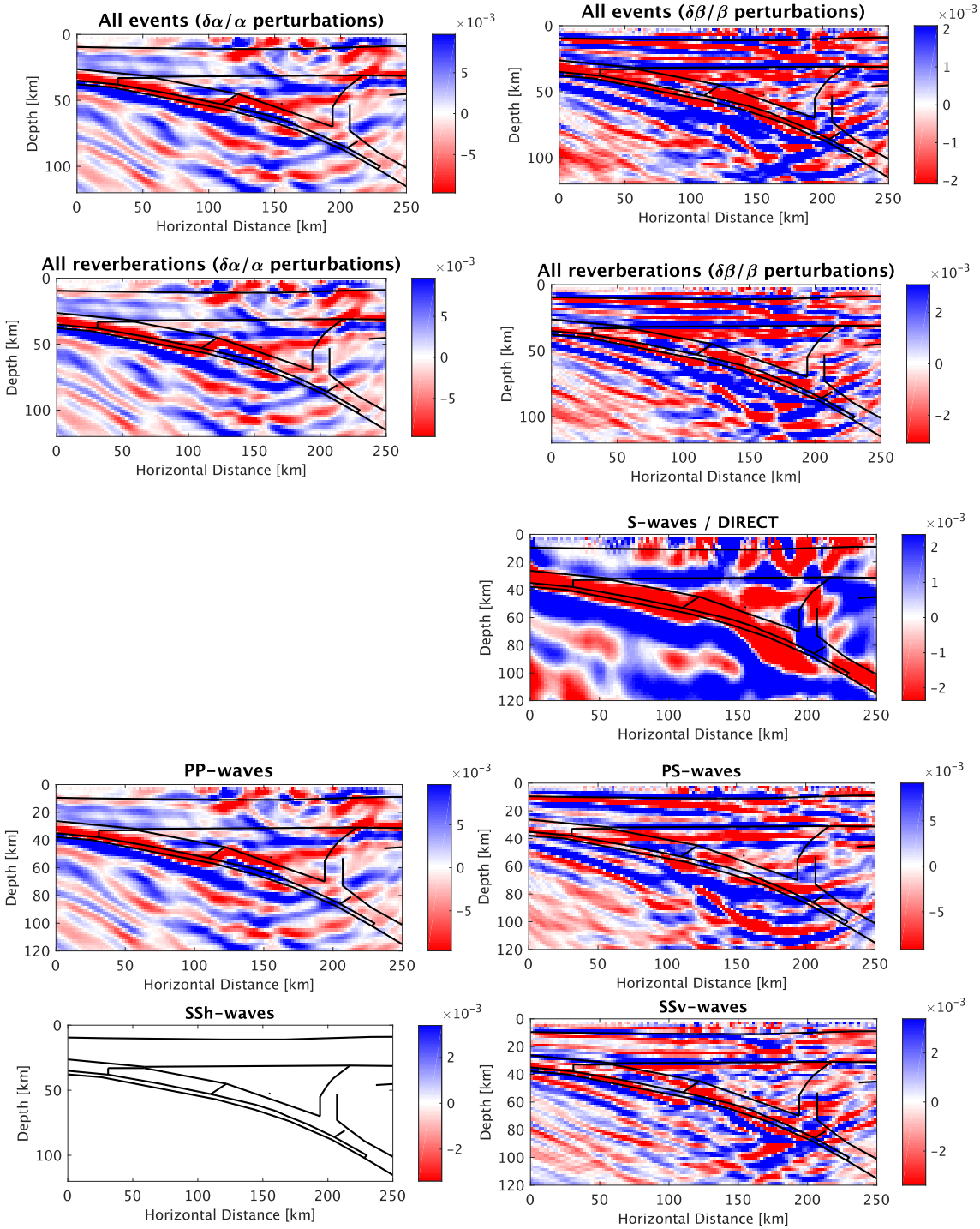

Figure A.6: Images generated using the Synthetic data set with a slow forearc mantle, new method 1D.

Synthetic data set - slow forearc mantle
new method - 2D

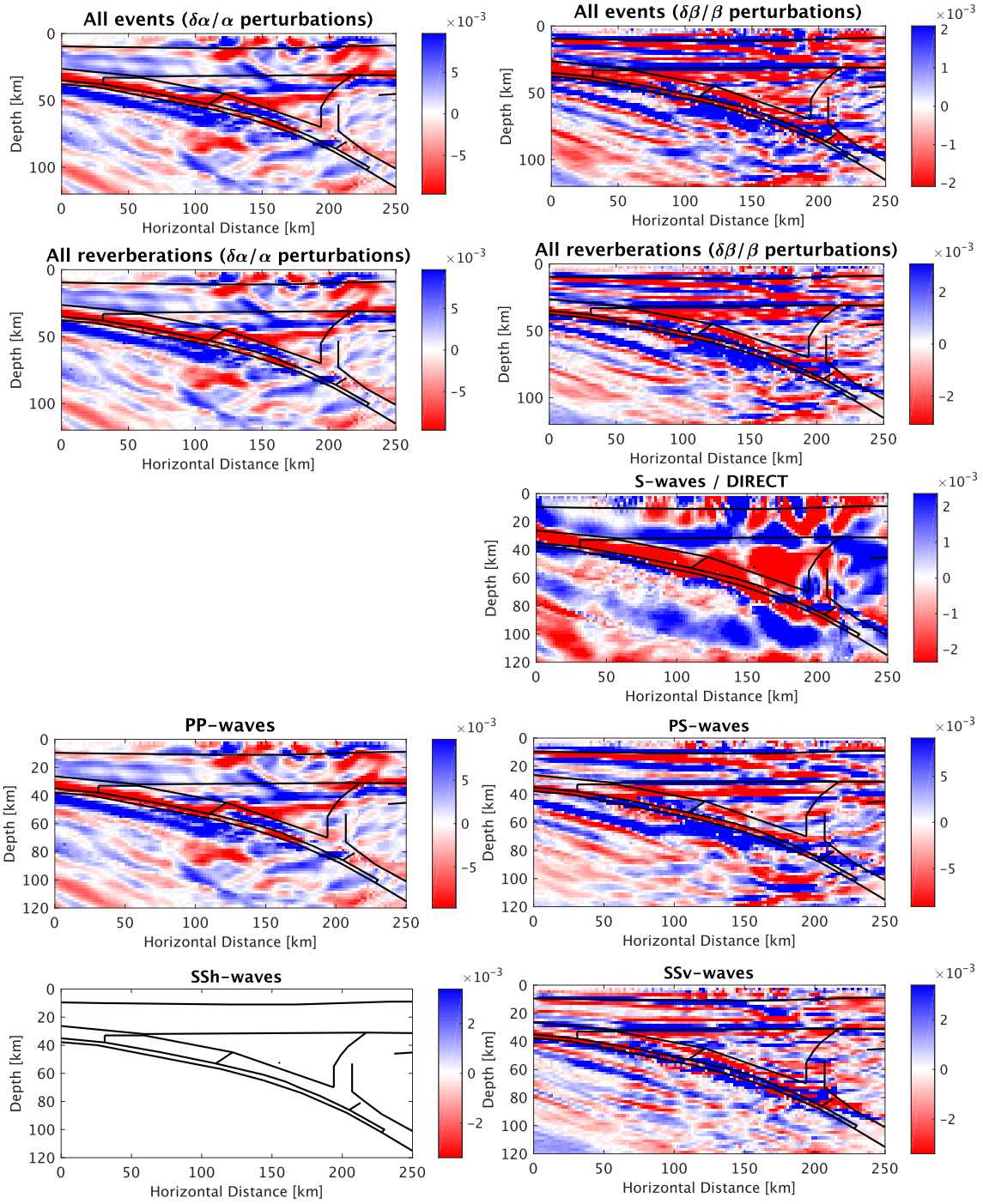

Figure A.7: Images generated using the Synthetic data set with a slow forearc mantle, new method 2D.

A.1.2 Cascadia data set - Homogeneous crust

Cascadia data set - original method

1D - homogeneous crust

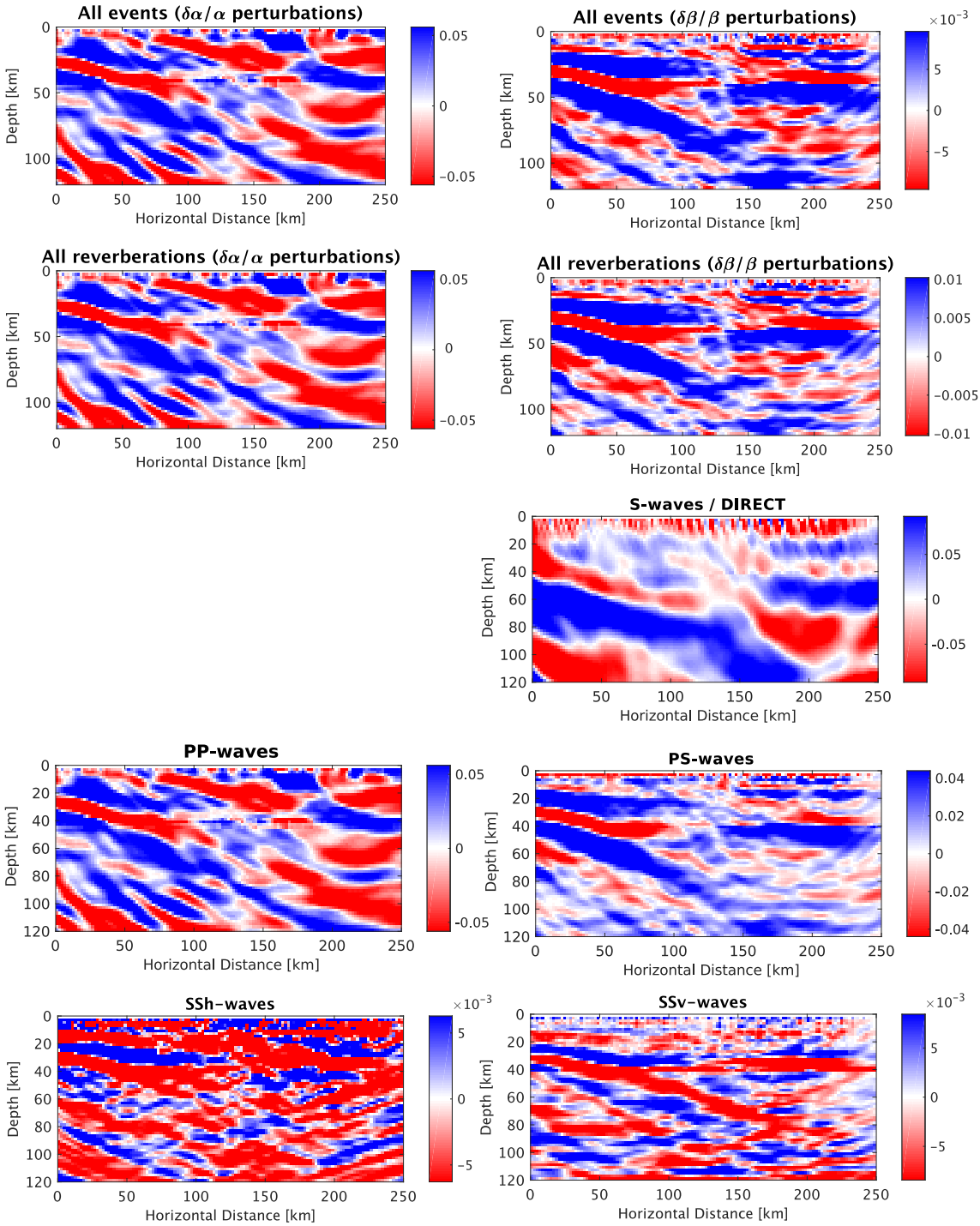

Figure A.8: Images generated using the Cascadia data set, original method 1D, homogeneous crust

Cascadia data set - new method
1D - homogeneous crust

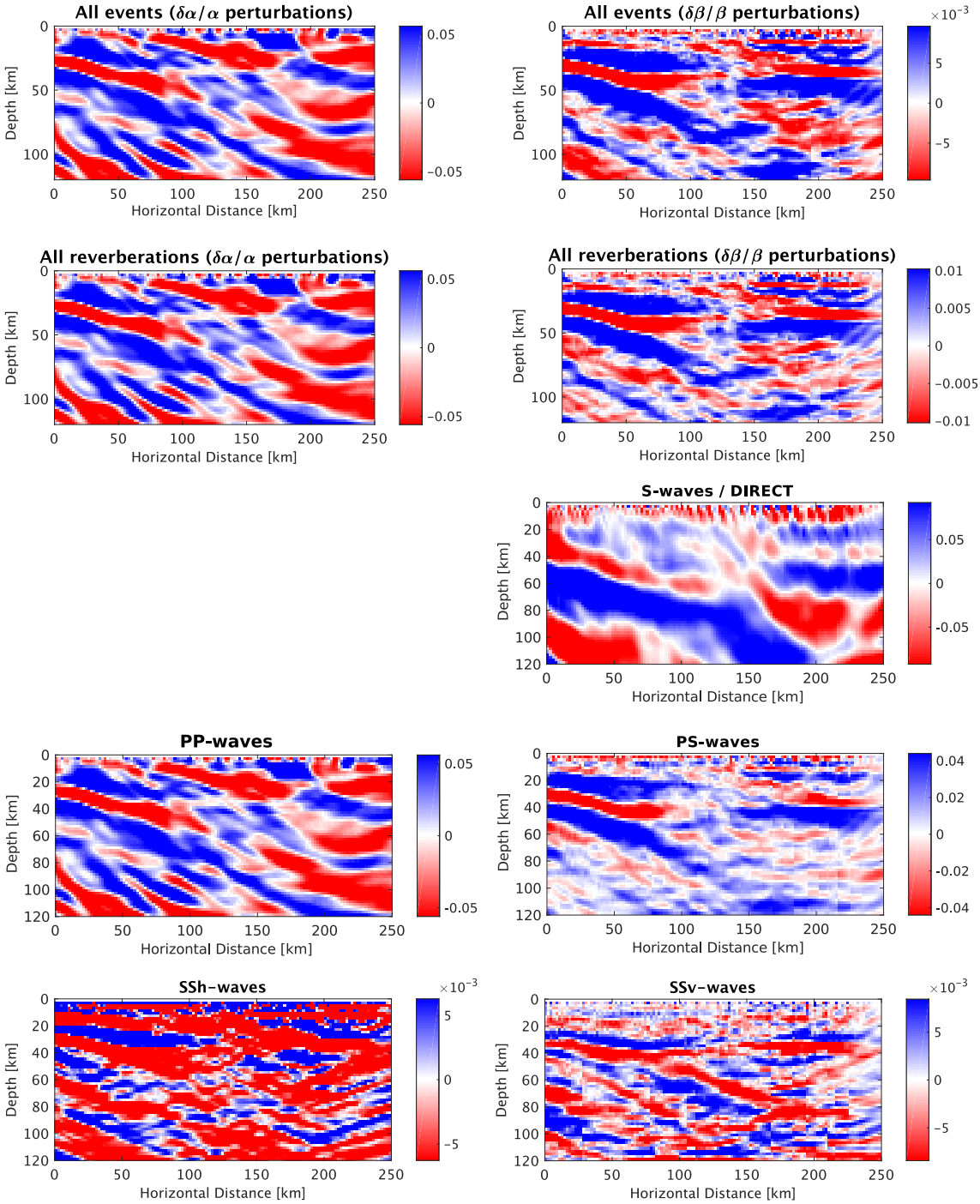

Figure A.9: Images generated using the Cascadia data set, new method 1D, homogeneous crust

Cascadia data set - new method
2D fast mantle wedge - homogeneous crust

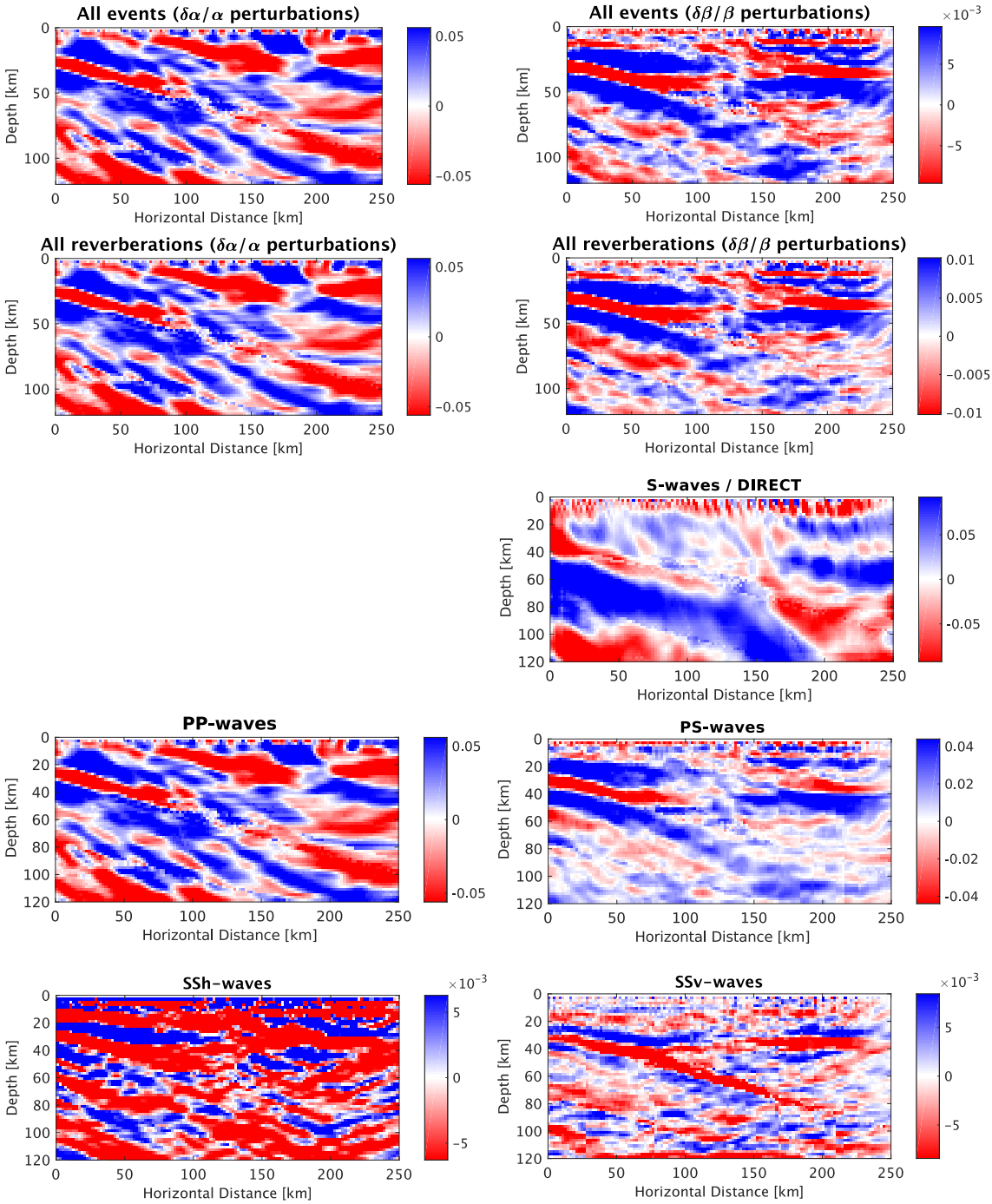

Figure A.10: Images generated using the Cascadia data set, new method 2D; fast mantle wedge, homogeneous crust

Cascadia data set - new method
2D slow mantle wedge - homogeneous crust

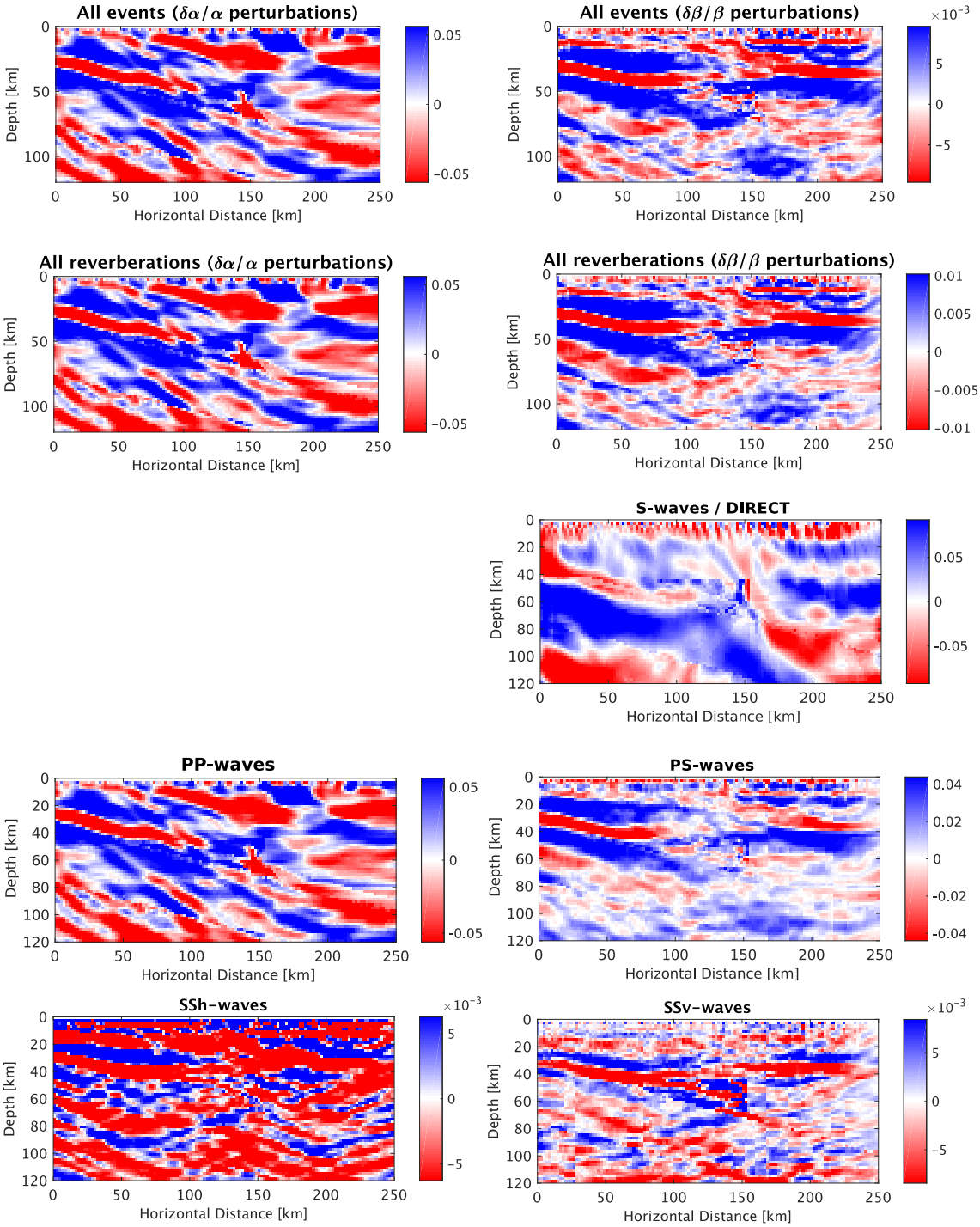

Figure A.11: Images generated using the Cascadia data set, new method 2D; slow mantle wedge, homogeneous crust

Cascadia data set - new method
2D moderate mantle wedge - homogeneous crust

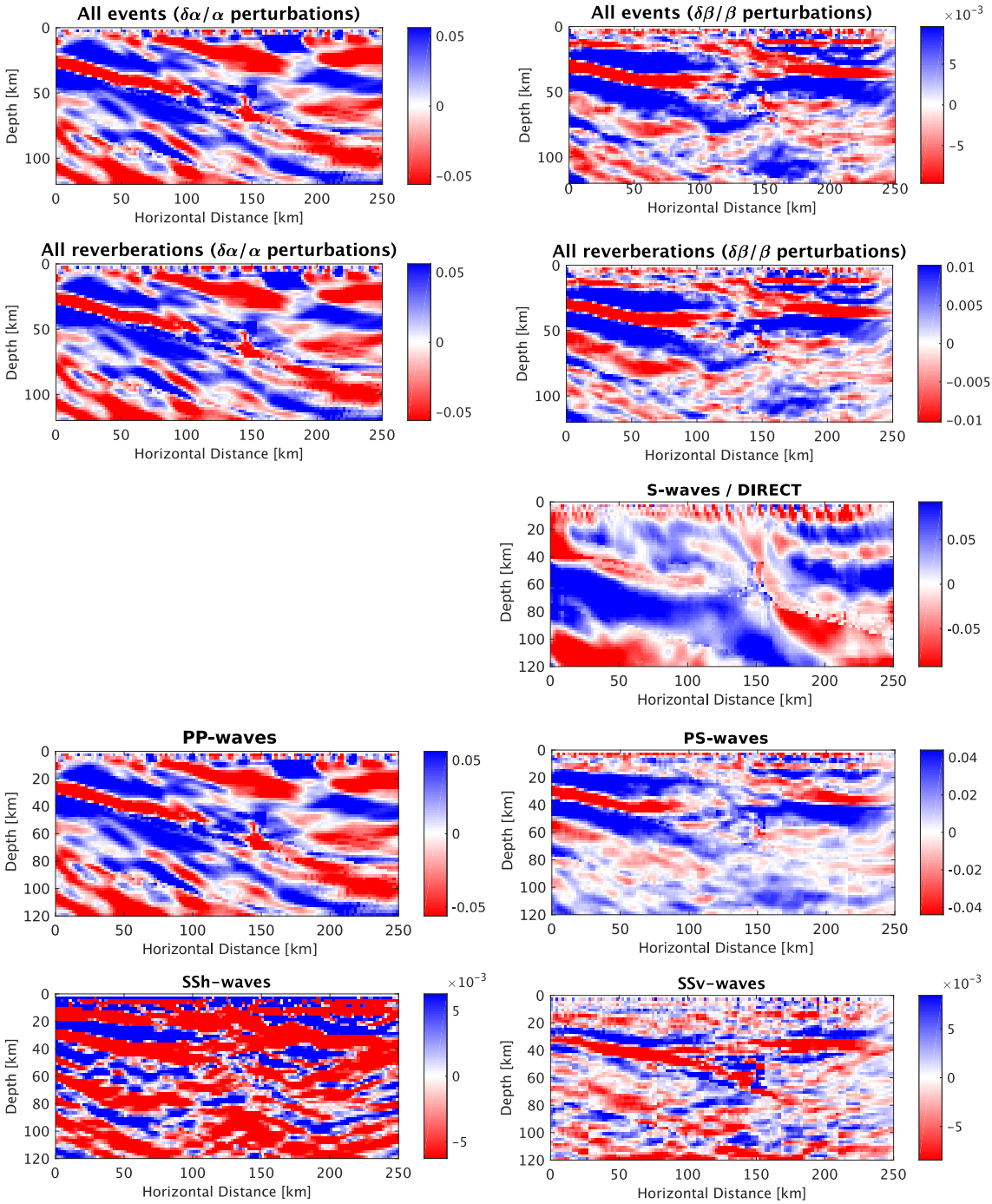

Figure A.12: Images generated using the Cascadia data set, new method 2D; moderate mantle wedge, homogeneous crust

A.1.3 Cascadia data set - Multi layered crust

Cascadia data set - original method

1D - multi layered crust

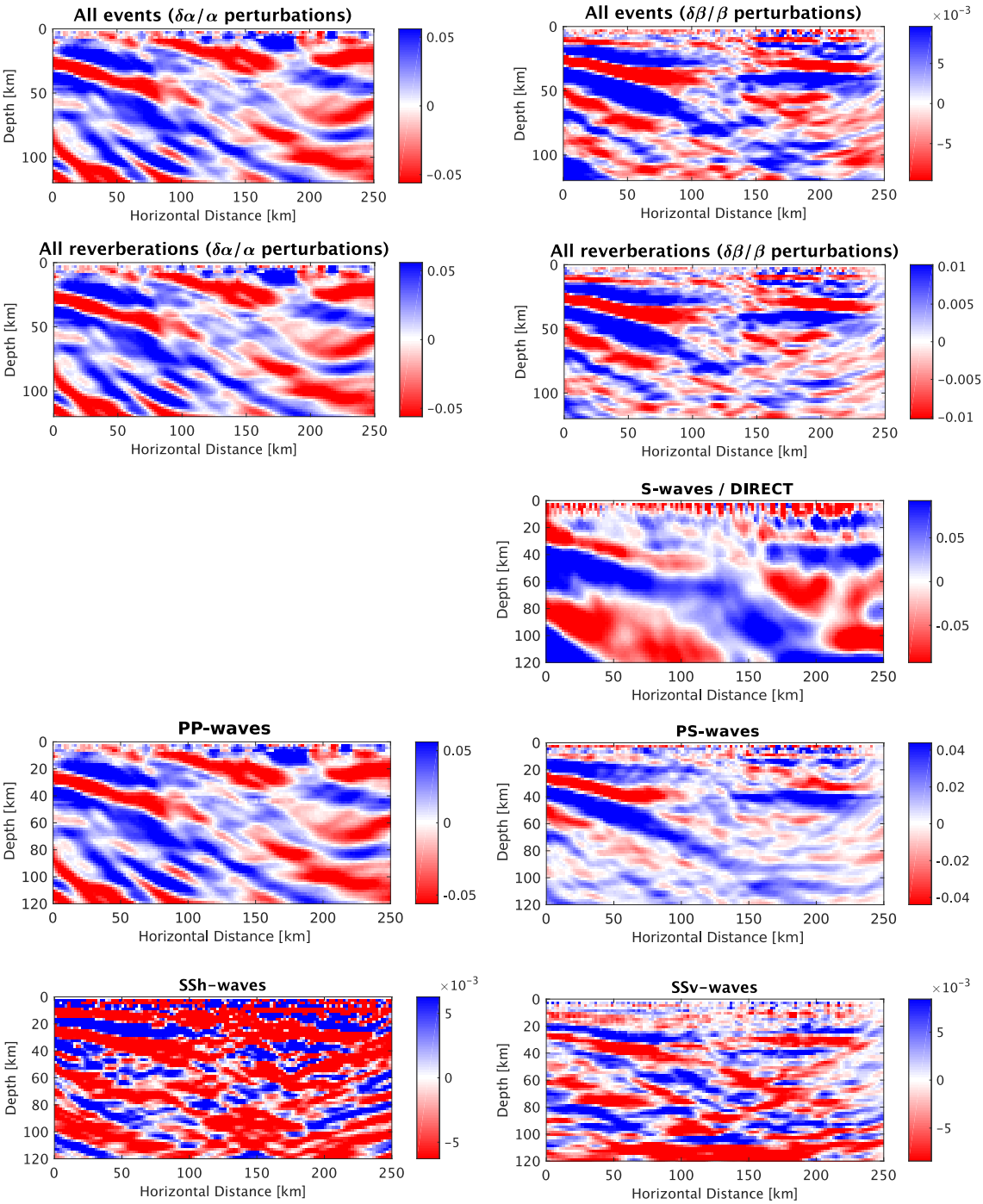

Figure A.13: Images generated using the Cascadia data set, original method 1D, multi layered crust

Cascadia data set - new method
1D - multi layered crust

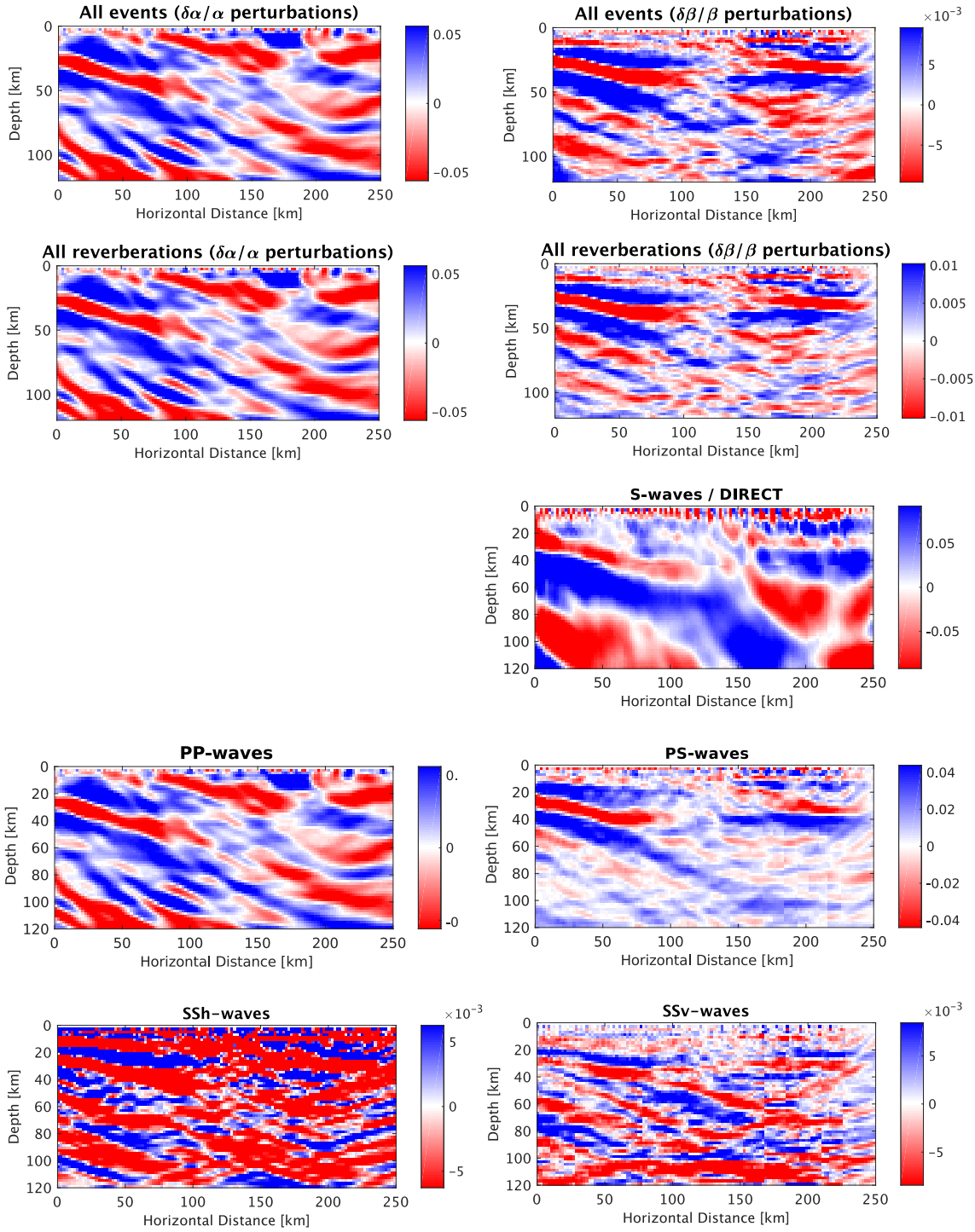

Figure A.14: Images generated using the Cascadia data set, new method 1D, multi layered crust

Cascadia data set - new method
2D fast mantle wedge - multi layered crust

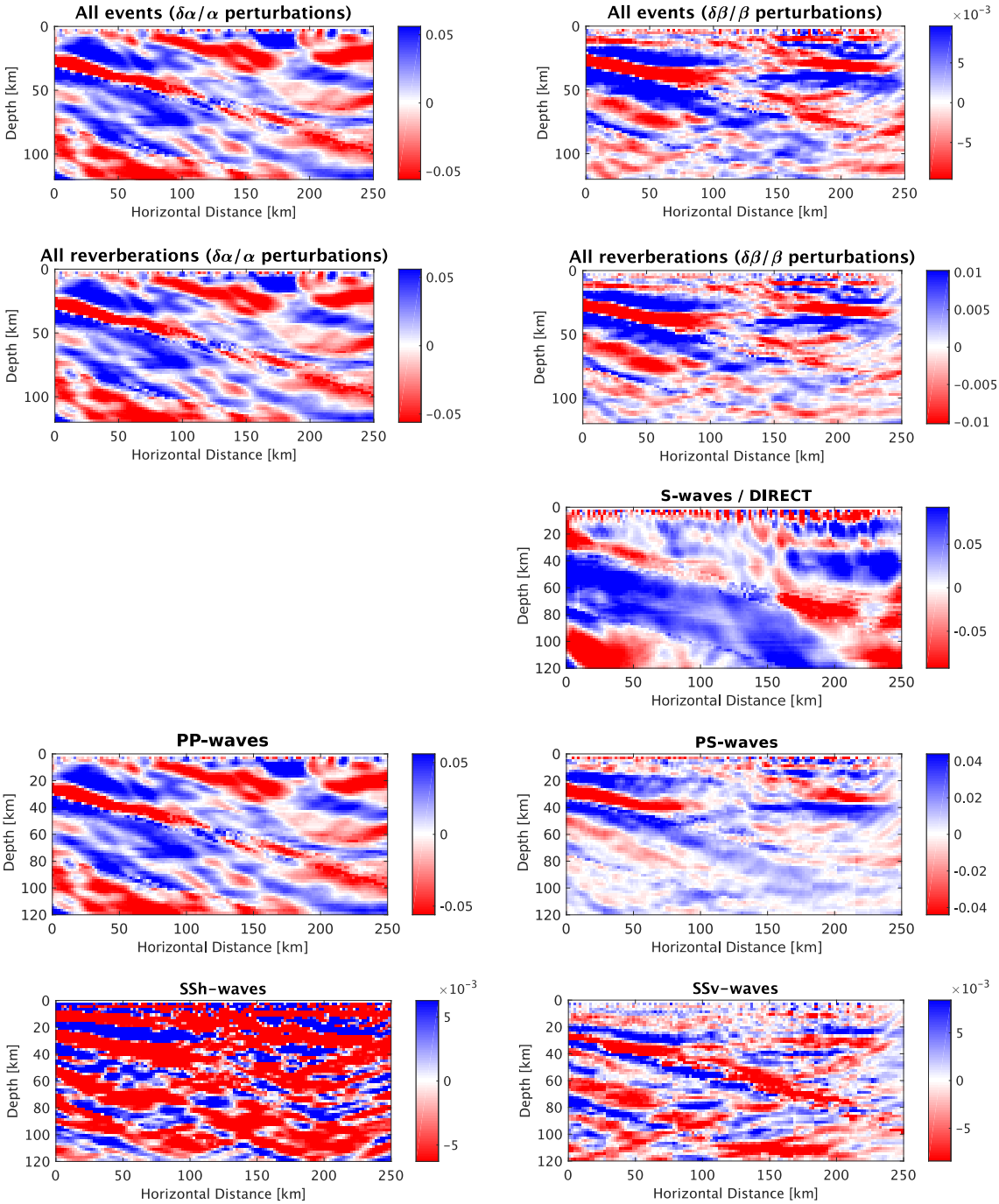

Figure A.15: Images generated using the Cascadia data set, new method 2D; fast mantle wedge, multi layered crust

Cascadia data set - new method
2D slow mantle wedge - multi layered crust

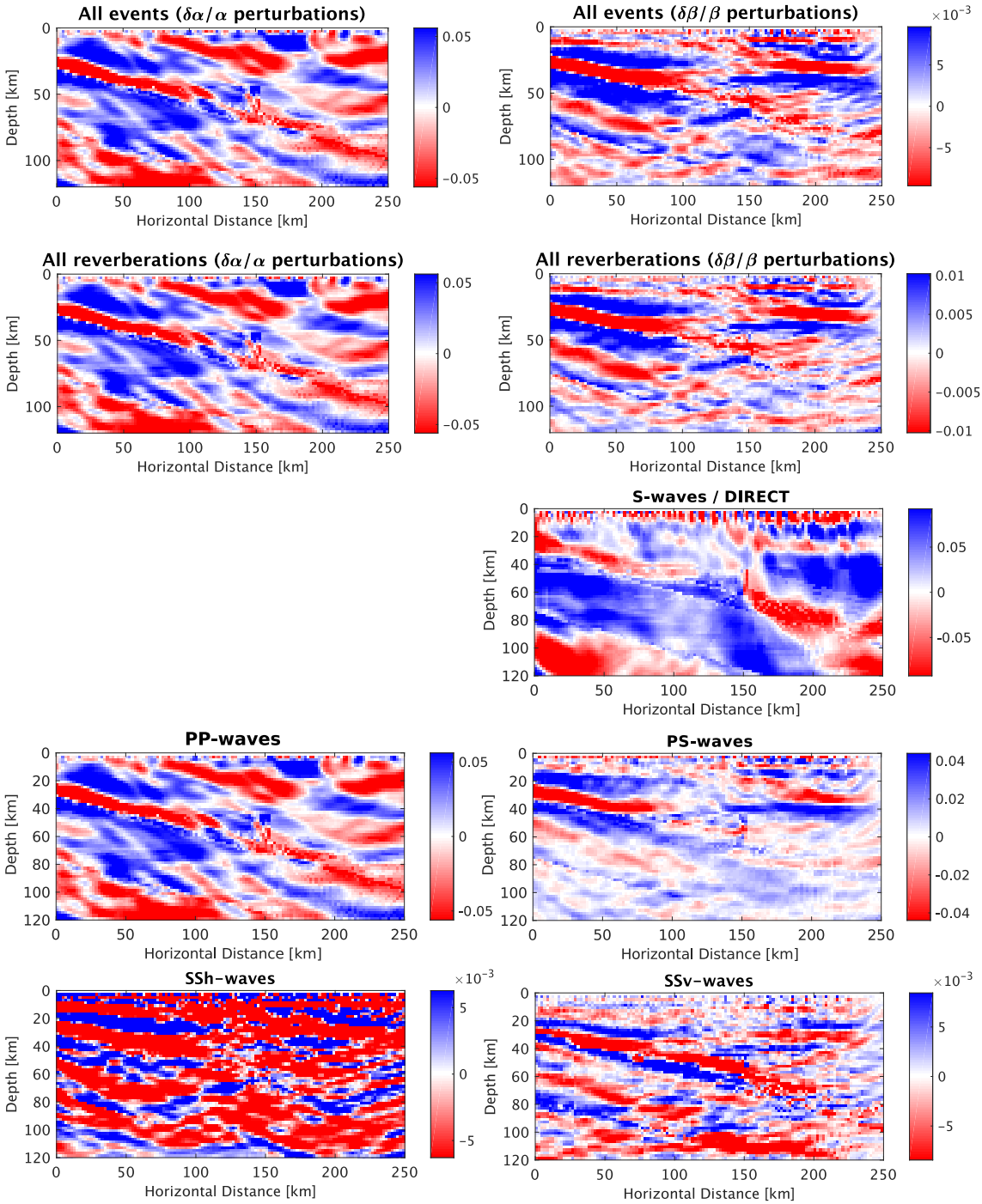

Figure A.16: Images generated using the Cascadia data set, new method 2D; slow mantle wedge, multi layered crust

Cascadia data set - new method
2D moderate mantle wedge - multi layered crust

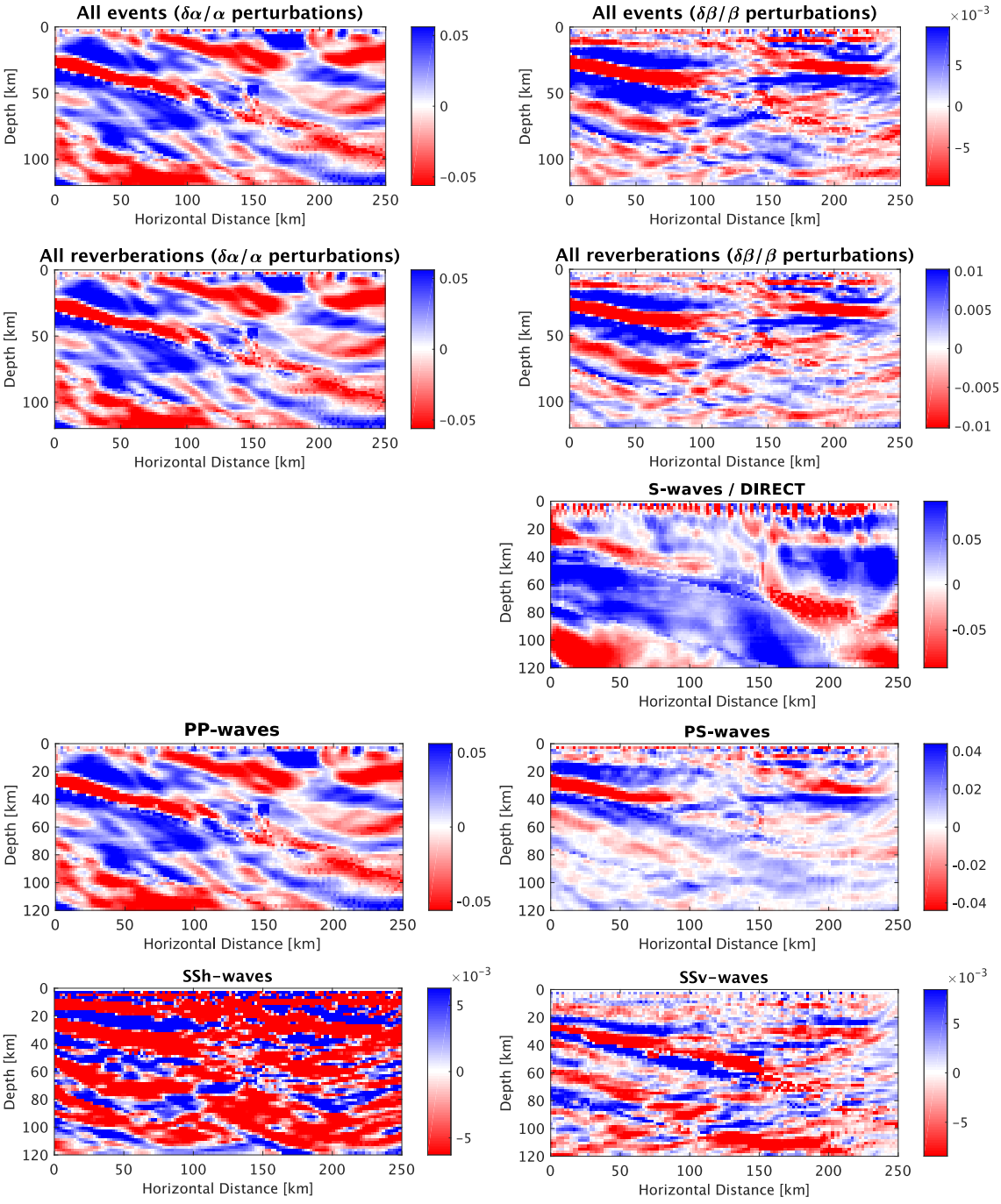

Figure A.17: Images generated using the Cascadia data set, new method 2D; moderate mantle wedge, multi layered crust

A.2 Scripts

In this appendix I have included the algorithms of the main scripts associated with this project. It is divded into two sections. Section one contains the algorithms of the original scripts, while section two contains the algorithms of the new method. The objective of each algorithm is included as a preface. In the algorithms describing the new method, a brief summary of the alterations is included at the end of each algorithm.

A.2.1 Overview original

Objective: Image the subsurface using inverse GRT with a 1D reference model.

```
PREPROCESSING
   Set up coordinate system: Find projection line and project the
      stations onto the projection line. The projection line is
      found by setting the projection angle, counterclockwise from
      north, manually, or to find the best fitting line, resulting
      in the least shifting of stations.
   Read data from individual events and pick the arrival of the
      incident P-wave to determine the time window to be used for
      deconvolution.
   Align the traces and decompose the wavefield to the source
      estimate for each event.
   Deconvolve the estimated source wavelet from the scattered
      wavefields
   Reconstitute the data in preparation for migration. Cutting time
       windows, transforming the data back to a R-T-Z system and
      rotating it to u1-u2-u3.
Create interpolation table {PREP_TABLE.m}
MAIN
   Load station file containing the projection angle and station
      position and enumeration along the projection line.
   Define events and weighting of the different scattering modes.
   Read the data corresponding to the events
   Create the interpolation table associated with the plane
      incident waves {PLANE_WAVE.m}
   Load table containing scattered waves
   Normalize the amplitudes by dividing the time signal by the
      square root of the P-wave impedance. This is required to
      retrieve the true velocity perturbations.
   Migrate the data {MIGRATE.m}
REPRODUCE
   Compute the alpha and beta perturbations
   Plot the results
```

Original prep_table.m

Objective: Calculate pp, ps, tp ,ts , Jp and Js.

```
Load velocity model and calculate velocity dependent parameters
Create parameter arrays of 51 length corresponding to depth, p-
   velocity, s-velocity density and layer number as a function of
   depth.
Define slowness range for event interpolation and scatter range for
    station interpolation.
Loop over slowness
   Loop over depth
      Define scattering angle range, theta, which is dependent on
         the depth and scatter range.
      Calculate the obliquity corrected velocities
      Loop over theta/scattering angle
         Loop over layers
           Calculate pa, pb, ta, tb, Ja, Jb, xa,xb
         End loop over layers
      End loop over scattering angle
      Interpolate xb for scatter range to obtain correct pp, ps, tp
         ,ts,Jp, Js
   End loop over depth
End loop over slowness
```

Original plane_wave.m

Objective: Calculate ti, tip,tis (travel time of direct and P/S reverberated incident wave.

```
Load velocity model and calculate velocity dependent parameters
Create parameter arrays of 51 length corresponding to depth, p-
   velocity, s-velocity density and layer number as a function of
   depth.
Set up event parameters
Define horizontal range for interpolation
Loop over event
   Loop over horizontal slowness
      Loop over depth array
         Loop over horizontal range
            If the horizontal slowness <= total slowness
               Loop over layer
                  Calculate ti, tip, tis
               End loop over layer
            End if
         End loop over horizontal range
      End loop over depth
   End loop over horizontal slowness
```

```
   If total slowness is negative, flip traveltimes along spatial
      points. Event incoming from clockwise direction. End if.
End loop over event
```

Original migrate.m

Objective: Migrate the traces.

```
Set up model grid, initialize matrices and load tables
Event dependent calculations
   Trapezoidal integration over horizontal slowness
   Compute the scalar amplitude and reflection coefficients
Loop over vertical scatter position z
   Velocity model dependent calculations
      Calculate Model parameters a,b,and rho as a function of depth
      Calculate W11, bona,A0, A0s, psign dtxs,n0p and n0s
   Loop over horizontal scatter position x
      Loop over event
         Station dependent calculations
         Scatter point dependent calculations
         Estimate total traveltime gradient
         Gather points along diffraction hyperbola
         Estimate angle between incident wave and backprojected
            diffracted wave
         Calculate scattering matrix
         Calculate Beylkin determinant
         Calculate spectra coefficients
         Apply station weights
      End of event loop
      Apply station weights (continued)
      Estimate psi, normalization factor [Hessian], (dip resolution
         )
      Estimate k, normalization factor [Hessian] (volume resolution
         )
      Calculate individual components of Hessian
      Calculate individual components of Gradient (spatial gradient
          of total traveltime function?)
   End loop over x
End loop over z
```

Original reproduce.m

Objective: Calculate the alpha and beta perturbations and plot the results.

```
Load event file produced by migration
Define weights applied to each scattering mode
Loop over vertical scatter position z
```

```
   Loop over horizontal scatter position x
      Compute square root of Hessian
      Compute gradient function for each individual mode
      Generalized inversion
   End horizontal image point
End vertical image point
dcrep.m plots the image points
```

A.2.2 Overview new

Objective: Image the subsurface using inverse GRT with a new 2D reference model.

```
PREPROCESSING: No changes
PREP_TABLE:Create interpolation table containing the traveltime,
   slowness and Jacobian for P and S phases for the scattered waves
   .
MAIN
   Load station file containing the projection angle and station
      position and enumeration along the projection line.
   Define events and weighting of the different scattering modes.
   Load model grid
   Load table containing scattered waves
   read the data corresponding to the events
   Normalize the amplitudes by dividing the time signal by the
      square root of the P-wave impedance. This is required to
      retrieve the true velocity perturbations.
   Migrate the data.
Reproduce
```

Changes: plane_wave is moved to within migrate, scatter grid is loaded in main, not in migrate.

New prep_table.m

Objective: calculate pp, ps, tp ,ts , Jp and Js.

```
Load velocity model
Load scatter grid
Load station information
Define scattering angle range [-pi/2:pi/2]  length: 201
Calculate unique 1D velocity models and scattering angle using ray
   tracer function. See alternate flowchart.
Define slowness range for event interpolation, [0:0.008],  length
   51
Loop over vertical scatter position z
   Loop over horizontal scatter position x
```

```
      Extract scattering angle associated with scatter point
      Loop over scattering angle
         Extract 1D velocity model associated with scattering angle
         Loop over slowness range
            Check validity of scattering angle
            Loop over layers
               Find obliquity corrected velocity
               Calculate pp, ps, tp ,ts ,Jp, Js
               Check for complex numbers
            End loop over layers
         End loop over slowness
         Store slowness, traveltime and Jacobian
      End scattering angle
   End horizontal scatter position
End vertical scatter position
```

Changes: Ray tracing added, Change of loop structure, variables calculated directly.

New plane_wave.m

Objective: Calculate ti, tip,tis (travel time of direct and P/S reverberated incident wave. Plane wave new [function] Ray parameter of event used as take-off-angle as part of backscattering

```
Loop over stations
   Find velocity model using ray tracing algorithm
   If current slowness <= abs(total slowness)
      Loop over layers
         Compute ti,tip,tis using same equations as original
      End loop over layers
   End if
End loop over stations
```

Changes: since the plane wave is now a function and located within the migration script it is already a loop over event and scatter-point. This eliminate the loop over event and depth array from the original plane-wave. The loop over horizontal range has been replaced by a loop over station-position. The plane-wave is as a result placed within in one additional loop, compared to the original script, a loop over horizontal scatter position x.

New migrate.m

Objective: Migrate traces

```
Initialize matrices
Event dependent calculations
Loop over vertical scatter position z
```

```
Loop over horizontal scatter position x
   Loop over event
      Station dependent calculations
      Velocity model dependent calculations
      Scatter point dependent calculations
      total travel time gradient
      Plane wave calculations
      Gather point along diffraction hyperbola
      RESUME AS ORIGINAL ...
```

Changes: The velocity model dependent calculations are moved to within the loop, the plane wave calculations are moved from main to within the loop-structure. The interpolations associated with the scattered wave are changed from an interpolation over event, scatter point and station to an interpolation over event. The interpolations associated with the plane wave are made completely redundant.